Geometry, topology and mechanics of twisted elastic fibers

by

Vishal P. Patil

Submitted to the Department of Mathematics
in partial fulfillment of the requirements for the degree of

Doctor of Philosophy

at the

MASSACHUSETTS INSTITUTE OF TECHNOLOGY

June 2021

Author .....
Department of Mathematics
May 7, 2021

Certified by .....
Jörn Dunkel
Associate Professor
Thesis Supervisor

Accepted by .....
Jonathan Kelner
Chairman, Department Committee on Graduate Theses

Geometry, topology and mechanics of twisted elastic fibers

by

Vishal P. Patil

Submitted to the Department of Mathematics
on May 7, 2021, in partial fulfillment of the
requirements for the degree of
Doctor of Philosophy

Abstract

Elastic rods and fibers are ubiquitous in physical and biological systems across a range of length scales, from microtubules to construction beams. In this thesis, we explore the impact of twist on the failure and stability of elastic rods by studying fragmentation and knot dynamics. We begin with a famous phenomenon in elastic rod fragmentation observed by Feynman, who discovered that dry spaghetti typically breaks into three or more pieces when exposed to large bending stresses. Combining theory, experiments and analytic scaling arguments, we demonstrate that twist may be used to achieve binary fracture of brittle elastic rods. Additionally, we show that quenching allows for robust control of the fragmentation cascade. In the second half of this thesis, we use twist to investigate the stability of softer fibers in knotted configurations. We identify twist-based topological counting rules that explain the relative stability of bend knots, which are used to tie two ropes together. These counting rules reveal an underlying stability phase diagram which agrees with numerical simulations and experimental testing of several climbing and sailing knots. Combining the notions of structural and topological stability, we then investigate the energy discharge dynamics of a knotted elastic fiber after it is broken. We show that this class of topological batteries contains special topologically resonant states for which energy release is superslow. Finally, we apply our topological model to surgical knots. Through numerical simulation, we show that topology can be used to identify mechanically stable and balanced suture knots.

Thesis Supervisor: Jörn Dunkel
Title: Associate Professor

Acknowledgments

First and foremost, I am especially thankful to my advisor, Professor Jörn Dunkel, for all his guidance throughout my PhD. His support, patience, and advice have been invaluable, and will continue to inspire me throughout my scientific career. I am particularly grateful for his dedication to mentorship and to providing a stimulating scientific environment; I have learned a tremendous amount from our open-ended discussions about mathematics and physics. Jörn introduced me to the spaghetti breaking problem in my first year of graduate school. I could not have anticipated then that this project and its spinoffs would eventually become my thesis.

I would like to express my appreciation to the many people at MIT and in the wider scientific community whose expertise has helped me at various points during my graduate school career. I am grateful to Professors John Bush, Mathias Kolle and Emmanuel Villermaux for their encouragement and helpful discussions. I would like to thank Dr. Duke Cameron and Dr. Chin Siang Ong for their guidance and advice on surgical applications.

I am grateful to Ronald Heisser, for teaching me everything I know about experiments, and my other collaborators, Joseph Sandt, Žiga Kos, and Norbert Stoop without whom this thesis would not have been possible. I would also like to thank all the members of the Dunkel group, especially my officemates Dominic Skinner and Boya Song, for the many valuable scientific and non-scientific conversations over the years.

I would like to thank my roommate, Ted Grunberg, and my other friends and classmates from MIT and Harvard: Matt Brennan, Julien Clancy, Christian Gaetz, Frederic Koehler, Josh Lam, Derek Leung, Ashwin Narayan and Paxton Turner amongst others. I am grateful for their friendship throughout graduate school. I am also grateful to my friends on the MIT Badminton Club.

None of this would be possible without the unconditional love and support from my wonderful parents, and my sister Pradnya. I am forever grateful for all they have done.

Finally, I owe a profound debt of gratitude to my wonderful partner, Julie Takagi, for her infinite patience, good humor and for figure 4-8A. This thesis represents the culmination of the spaghetti work through which we first met.

Contents

List of Figures

Chapter 1

Introduction

Rods, filaments and fibers are ubiquitous in natural and man-made matter, performing important physical and biological functions across a wide range of scales, from columns [60], trees [39, 142, 2] and bones [113] to the legs of water striders [61], semiflexible polymer [68] networks [122, 17] and carbon nanotube composites [11]. The mechanics of rods and fibers in these settings is particularly crucial. For example, the interplay between twisting and bending is responsible for the morphological properties of DNA [88, 18, 128] and other proteins [85], and is thought to have biological function. On larger scales, twist dynamics underlies muscle function [23]. Owing to their slender structure, elastic fibers can undergo large deformations. The role of twist under these extreme conditions presents a number of interesting questions [80, 66, 114].

In this thesis, we examine how twist affects the failure and stability of elastic rods and fibers. In the hard, brittle case, the relevant failure mode is fracture [139, 6]. Elastic rods are known to fragment catastrophically, a phenomenon famously observed by Feynman [131]. We show that twist is a parameter which can be used to control this rapid fragmentation process. For softer, flexible fibers, fracture is no longer a typical failure mode. In fact, due to their flexibility, soft fibers can be contorted into topologically complex configurations. Accordingly, the failure mode we examine in this case is topological stability. In other words, the central stability question is whether a knot will slip or hold.

This thesis is organized as follows. In Chapter 2 we introduce the Kirchhoff equa-

tions for elastic rods, and sketch their derivation from 3D elasticity. These equations, which describe inextensible rods that can bend and twist, are the fundamental equations used to describe rods and fibers. This model is used in Chapter 3. We survey extensions and alternative formulations of these equations for use in subsequent chapters. In particular, we formulate an overdamped, extensible version of the Kirchhoff equations, which is used to model knots in chapters 4 and 5. In addition, we show how to formulate rod equations in terms of energy gradients, a form which more readily permits discretization and simulation [14].

In Chapter 3, we study the failure of brittle elastic rods. We model the fragmentation process using the inextensible Kirchhoff equations together with a stress based fracture criterion. In the fracture setting, these equations permit a further reduction into decoupled bend and twist equations. The analysis of these equations show that twist waves travel faster than bending waves, and that twist therefore only plays a role in the first fracture. This difference in timescale is responsible for the phenomenon of twist controlled binary fracture. The results of Chapter 3 are published in: R. H. Heisser, V. P. Patil, N. Stoop, E. Villermaux, and J. Dunkel. Controlling fracture cascades through twisting and quenching. *Proc. Natl. Acad. Sci. U.S.A.*, 115(35), 8665-8670, 2018 [58].

In the second half of this thesis, we focus on knots tied in softer, more flexible, elastic fibers. In Chapter 4 we show how to augment the overdamped, extensible Kirchhoff equations introduced in Chapter 2, with contact handling and friction-like collision forces. These collision forces have an interpretation in terms of topological counting rules which can be calculated from knot diagrams. In particular, we show that the self-torque within a knot is related to the writhe of the knot. The topology and mechanics of the knot therefore interact through twist. The results of Chapter 4 are published in: V. P. Patil, J. D. Sandt, M. Kolle, and J. Dunkel. Topological mechanics of knots and tangles. *Science*, 367(6473), 71-75, 2020 [110].

In Chapter 5, we treat closed elastic knots as energy storing topological batteries. This energy storage protocol has the attractive property that the energy can be easily released by cutting the knot open. We study the dynamics of energy discharge

from a variety of different knot types, each with different amounts of initial twist. Using the numerical framework developed in this thesis, we are able to demonstrate the existence of topologically resonant states, with superslow energy release. The results of Chapter 5 are published in: V. P. Patil, Ž. Kos, M. Ravnik, and J. Dunkel. Discharging dynamics of topological batteries. *Phys. Rev. Research*, 2(4), 043196, 2020 [109].

In Chapter 6, we apply the topological model of Chapter 4 to surgical knots. We develop a simplified model for sutures, and show how to relate mechanical observables of this model to topological features of the suture knot. Our model predicts that the most commonly used surgical knots are indeed the most mechanically stable and balanced.

In Chapter 7 we conclude our study of twisted fibers and discuss future directions.

Chapter 2

Elastic fiber models

In this chapter, we survey various models of elastic rods and fibers. These models are all based on the Kirchhoff equations [74, 75], which describe an inextensible elastic rod with bending and twisting degrees of freedom. We begin by deriving these equations from 3D elasticity theory [26, 84, 33, 27, 7], putting them in the context of 3D continuum mechanics. The derivation we sketch is based on the treatment in Ref. [33], and relies on the assumption that the deformation of each cross section of the rod is small compared its size. The reduction from 3D also allows a stretch degree of freedom to be retained, which results in an extensible generalization of the Kirchhoff equations [100].

Variational principles underlie elastic rod dynamics, and are a useful tool for simulation purposes. In sections 2.4 and 2.5, we show how the forces and torques on a rod correspond to gradients of the bend, twist and stretch energies. These reformulated rod equations can be discretized in an intuitive way, and are the continuum counterpart to the discrete elastic rod framework introduced in Refs. [14, 13]. The simulation tools used in this thesis are based upon this framework.

For the softer elastic fibers we study in chapters 4 and 5, the dynamics are overdamped. In section 2.6, we introduce an overdamped version of the extensible equations to model these scenarios. These equations are given in terms of energy gradients, a formulation in which they can be more easily discretized and simulated.

2.1 Conservation laws

The general form of rod equations can be deduced from conservation laws for linear and angular momentum [33]. We begin with a naturally straight rod with length L, uniform density ρ and constant cross section. The relaxed reference state for the rod can be chosen to lie along the z-axis. In particular, let $\mathcal{C} \subset \mathbb{R}^2$ be a cross section of the rod with center of mass at the origin. Orient $\mathcal{C}$ so that its principal axes coincide with the coordinate axes $\mathbf{e}_1$ and $\mathbf{e}_2$. The reference state of the rod is then

$$\mathcal{B} = \{(X, Y, s) : (X, Y) \in \mathcal{C}, 0 \leq s \leq L\} \tag{2.1}$$

where the z-coordinate is labelled by s since it is an arc-length parameter for the centerline curve, $\boldsymbol{x}_0(s) = (0, 0, s)$, and $\tilde{x}$ and $\tilde{y}$ are cross sectional degrees of freedom. To simplify index notation, we will also set

$$\mathbf{X} = (X_1, X_2, X_3) = (X, Y, s)$$

Let h be the maximum distance of a point in $\mathcal{C}$ from the origin, so $|\tilde{x}|, |\tilde{y}| < h$. The description of $\mathcal{B}$ as a rod requires $\alpha = h \ll L$. In other words, the length of the rod must be much larger than the size of a cross section.

Consider a general time dependent deformation, $\mathbf{X} \mapsto \boldsymbol{\phi}(\mathbf{X}, t)$ of the rod. The general form of rod equations follows from the assumption that there is a stress tensor, $\sigma_{ij}(\mathbf{X}, \boldsymbol{\phi}(\mathbf{X}, t))$, governing force transmission within the deformed body. This assumption means that the force transmitted across an area element $\mathbf{dS}$ is $\sigma_{ij} dS_j$ (using summation convention). The stress tensor can be chosen so that the force components $\sigma_{ij} dS_j$ are given in terms of the deformed basis $\{\partial_i \boldsymbol{\phi}\}$ and the area element dS_j in terms of the reference basis $\{\mathbf{e}_j\}$.

To derive the general rod equations, we decompose $\boldsymbol{\phi}$ in terms of centerline and cross sectional deformations, and apply conservation laws. Let $\mathcal{C}(s)$ be the cross section of fixed s in the reference state, and let $\boldsymbol{x}(s, t) = \boldsymbol{\phi}(0, 0, s, t)$ be the material image of the reference centerline curve $\boldsymbol{x}_0(s)$. The surface $\boldsymbol{\phi}(\mathcal{C}(s), t)$ can be parametrized

by X, Y allowing us to decompose $\boldsymbol{\phi}$

$$\boldsymbol{\phi}(\mathbf{X}, t) = \boldsymbol{x}(s, t) + \boldsymbol{\phi}^0(X, Y, s, t)$$

Note that $\boldsymbol{x}(s,t)$ is not necessarily the centroid of $\boldsymbol{\phi}(\mathcal{C}(s), t)$. However, $\boldsymbol{x}(s,t)$ is approximately the centroid of the deformed cross section in a precise sense, as we will discuss in the next section. For the purposes of the calculation we present here, we assume that the centroid property holds. Applying conversation of linear momentum in a region $a < s < b$ of the rod, yields

$$\frac{d}{dt}\int_a^b ds \int_{\mathcal{C}(s)} dXdY\ \rho\left(\dot{\boldsymbol{x}} + \dot{\boldsymbol{\phi}}^0\right) = \int_{\mathcal{C}(b)} \sigma_{ij} dS_j - \int_{\mathcal{C}(a)} \sigma_{ij} dS_j$$

where dots denote t-derivatives. The LHS represents the change of momentum in the region $a < s < b$, and the RHS is the total internal force on the boundary of this region. External forces can be added to the final rod equations later. The momentum conservation law can be written in derivative form

$$\frac{d}{dt}\int_{\mathcal{C}(s)} dXdY\ \rho\left(\dot{\boldsymbol{x}} + \dot{\boldsymbol{\phi}}^0\right) = \frac{d}{ds}\int_{\mathcal{C}(s)} \sigma_{ij} dS_j$$

This expression can be simplified by defining the force $\mathbf{F}(s,t)$ on the s'th cross section at time t, and the linear momentum $\mathbf{p}(s,t)$ of the s'th cross section at time t

$$\mathbf{F} = \int_{\mathcal{C}(s)} \sigma_{ij}\, dS_j \tag{2.2}$$

$$\mathbf{p} = \int_{\mathcal{C}(s)} dXdY\ \rho\left(\dot{\boldsymbol{x}} + \dot{\boldsymbol{\phi}}^0\right) = \rho A \dot{\boldsymbol{x}} \tag{2.3}$$

where A is the area of a reference cross section. The $\mathbf{p}$ equation follows from the fact that $\boldsymbol{x}(s,t)$ is approximately the center of mass of $\boldsymbol{\phi}(\mathcal{C}(s), t)$, so the integral of $\boldsymbol{\phi}^0$ over a cross section must vanish. The momentum equation thus becomes

$$\dot{\mathbf{p}} = \rho A \ddot{\boldsymbol{x}} = \mathbf{F}' \tag{2.4}$$

where primes denote s-derivatives. In the same way, the angular momentum conservation law in derivative form is

$$\frac{d}{dt}\int_{\mathcal{C}(s)} dXdY\ \rho\left(\boldsymbol{x}+\boldsymbol{\phi}^0\right)\times\left(\dot{\boldsymbol{x}}+\dot{\boldsymbol{\phi}}^0\right)=\frac{d}{ds}\int_{\mathcal{C}(s)}\epsilon_{ijk}\left(x_j+\phi_j^0\right)\sigma_{kl}\,dS_l$$

where ϵ_{ijk} is the Levi-Civita symbol. As before, define the moment on the s'th cross section $\mathbf{M}(s,t)$, and the internal cross sectional angular momentum $\mathbf{S}(s,t)$

$$\mathbf{M}=\int_{\mathcal{C}(s)}\epsilon_{ijk}\phi_j^0\sigma_{kl}\,dS_l \tag{2.5}$$

$$\mathbf{S}=\int_{\mathcal{C}(s)} dXdY\ \rho\left(\boldsymbol{\phi}^0\times\dot{\boldsymbol{\phi}}^0\right) \tag{2.6}$$

Since the integral of $\boldsymbol{\phi}^0$ over a cross section vanishes, the angular momentum equation becomes

$$\boldsymbol{x}\times\dot{\mathbf{p}}+\dot{\mathbf{S}}=(\boldsymbol{x}\times\mathbf{F}+\mathbf{M})'$$

where we have used the previously defined force $\mathbf{F}$ and momentum $\mathbf{p}$. We can use the momentum equation (2.4) to eliminate the $\dot{\mathbf{p}}$ term. The general form for rod equations is given by the momentum and angular momentum equations

$$\mathbf{F}'=\rho A\ddot{\boldsymbol{x}} \tag{2.7a}$$

$$\boldsymbol{x}'\times\mathbf{F}+\mathbf{M}'=\dot{\mathbf{S}} \tag{2.7b}$$

We have 6 equations with 12 unknown degrees of freedom, $\boldsymbol{x},\mathbf{S},\mathbf{F}$ and $\mathbf{M}$. The Kirchhoff equations can be derived by restricting to deformations $\boldsymbol{\phi}$ with 3 degrees of freedom corresponding to an orthonormal frame, $\{\mathbf{d}_1(s,t),\mathbf{d}_2(s,t),\mathbf{d}_3(s,t)\}$, along the centerline of the deformed rod (Fig 2-1). $\mathbf{S}$ and $\boldsymbol{x}$ are functions of this orthonormal frame, with $\boldsymbol{x}'=\mathbf{d}_3$. In the next section, we will use linear elasticity to derive a constitutive law for $\mathbf{M}$ in terms of this frame. This will reduce (2.7) to 6 unknown degrees of freedom, corresponding to the orthonormal frame and the force $\mathbf{F}$, thus

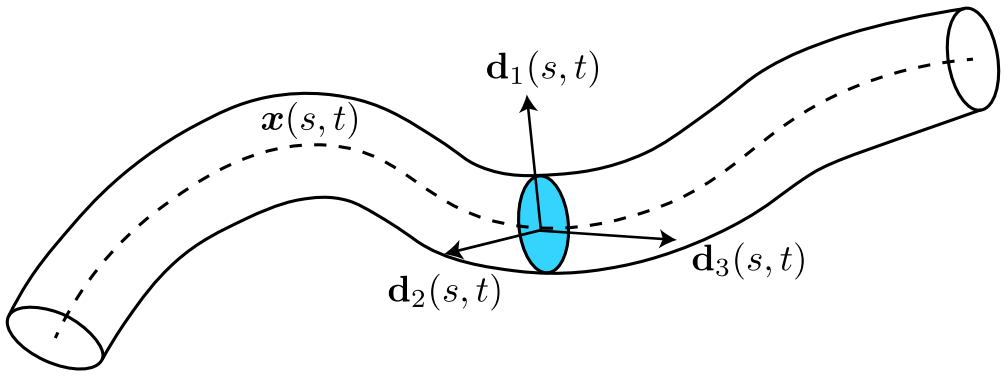

Figure 2-1: **Degrees of freedom of a Kirchhoff rod**

closing the system.

2.2 3D elasticity

Here we will sketch the derivation of the Kirchhoff equations from 3D elasticity [84, 33, 7]. We proceed by introducing the elastic strain and stress tensors and then solving the equations of elasticity for a class of rod deformations.

Consider the rod $\mathcal{B}$ given above in (2.1).

$$\mathcal{B} = \{(X, Y, s) : (X, Y) \in \mathcal{C}, 0 \leq s \leq L\}$$

where the cross section $\mathcal{C} \subset \mathbb{R}^2$ has center of mass at the origin, maximum radius h, and principal axes along the coordinate axes. To define the elastic tensors, we write the deformations in terms of displacements $\mathbf{u}$

$$\mathbf{X} \mapsto \boldsymbol{\phi}(\mathbf{X}) = \mathbf{X} + \mathbf{u}(\mathbf{X})$$

The metric tensor, g_{ij}, and strain tensor, ϵ_{ij} are dimensionless quantities

$$g_{ij} = \langle \partial_i \boldsymbol{\phi}, \partial_j \boldsymbol{\phi} \rangle$$
$$\epsilon_{ij} = \frac{1}{2} (\delta_{ij} - g_{ij})$$

where δ_{ij} is the Kronecker delta. Here, we assume that $\partial_i u_j$ is small, resulting in the small strain approximation to the strain tensor

$$\epsilon_{ij} = \frac{1}{2} (\partial_i u_j + \partial_j u_i)$$

For elastic materials, the stress tensor, σ_{ij} is a linear function of the strain tensor. We assume that the rod is isotropic and homogeneous, which results in the following constitutive law for the stress tensor [7]

$$\sigma_{ij} = K \epsilon_{kk} \delta_{ij} + 2\mu \left(\epsilon_{ij} - \frac{1}{3} \epsilon_{kk} \delta_{ij} \right) \tag{2.8}$$

where K is the bulk modulus and μ is the shear modulus of the rod. The elastic energy of the body is

$$\mathcal{E} = \int \sigma_{ij} \epsilon_{ij} \, dV$$

and the equations of motion are

$$\rho \ddot{\mathbf{u}} = \partial_i \sigma_{ij} \tag{2.9}$$

subject to the boundary condition $\sigma_{ij} n_j = 0$ on any free boundaries, where $\mathbf{n}$ is normal to the free boundary. The RHS of (2.9), which represents the internal elastic forces within the body, can be derived by extremizing the energy $\mathcal{E}$, as we will discuss in the next section. In addition to the bulk and shear moduli, it is also convenient to

define the Young's modulus E, and Poisson's ratio ν

$$\mu = \frac{E}{2(1+\nu)} \tag{2.10}$$

$$K = \frac{E}{3(1-2\nu)} \tag{2.11}$$

To close the rod equations (2.7), consider again the deformation $\boldsymbol{\phi}$ of the rod $\mathcal{B}$. Suppressing the time dependence, let $\boldsymbol{x}(s) = \boldsymbol{\phi}(0,0,s)$ as before, and set

$$\boldsymbol{\phi}(X,Y,s) = \boldsymbol{x}(s) + \boldsymbol{\phi}^0(X,Y,s)$$

We assume that each cross section approximately undergoes a rigid body transformation. This means that there is an orthonormal material frame, $\{\mathbf{d}_1, \mathbf{d}_2, \mathbf{d}_3\}$ with $\boldsymbol{x}' = (1+\epsilon)\mathbf{d}_3$, such that that the quantity $\mathbf{u}_0$ is small

$$\boldsymbol{\phi}(\mathbf{X}) = \boldsymbol{x}(s) + X\mathbf{d}_1(s) + Y\mathbf{d}_2(s) + \mathbf{u}^0(X,Y,s)$$

where $\mathbf{u}_0$ captures the non-rigid deformation of the cross sections. More precisely, $\{\mathbf{d}_1, \mathbf{d}_2, \mathbf{d}_3\}$ and $\mathbf{u}^0$ are chosen so that we can find an $\alpha < 1$ with the following properties

$$\max(h/L,\, h|\mathbf{d}_i'|,\, |\epsilon|) = \alpha, \qquad \frac{|\mathbf{u}^0|}{h}, \frac{\partial \mathbf{u}^0}{\partial X}, \frac{\partial \mathbf{u}^0}{\partial Y} = O(\alpha), \qquad \frac{\partial \mathbf{u}^0}{\partial s} = O(\alpha^2) \tag{2.12}$$

The deformed basis vectors $\partial_1\boldsymbol{\phi}$ and $\partial_2\boldsymbol{\phi}$ are then within $O(\alpha)$ of $\mathbf{d}_1$ and $\mathbf{d}_2$, which motivates the description of $\{\mathbf{d}_i\}$ as a material frame (Fig. 2-1). The stretching of the rod is captured by $\epsilon(s)$, and the rod is inextensible if $\epsilon \equiv 0$. In addition, the assumption that $|\mathbf{u}^0|/h = O(\alpha)$ implies that $\boldsymbol{x}(s)$ is the centroid of the deformed cross section, as claimed in the previous section. The fundamental degrees of freedom of an inextensible Kirchhoff rod are $\{\mathbf{d}_1, \mathbf{d}_2, \mathbf{d}_3\}$. In the extensible case, the stretching $\epsilon(s)$ must also be included.

Using this decomposition of $\boldsymbol{\phi}^0$, the cross sectional angular momentum $\mathbf{S}$ defined

in (2.6), can be expressed in terms of the frame $\{\mathbf{d}_i\}$

$$\begin{aligned}\mathbf{S} &= \int_{\mathcal{C}(s)} dXdY\ \rho\left(\boldsymbol{\phi}^0 \times \dot{\boldsymbol{\phi}}^0\right) \\ &= \int_{\mathcal{C}(s)} dXdY\ \rho\left(X\mathbf{d}_1 + Y\mathbf{d}_2\right) \times \left(X\dot{\mathbf{d}}_1 + Y\dot{\mathbf{d}}_2\right) + h\,O(\alpha)\end{aligned}$$

Consider the time derivative of the material frame. Since the frame is orthonormal, the matrix $\dot{\mathbf{d}}_i \cdot \mathbf{d}_j$ is antisymmetric, and we can write $\dot{\mathbf{d}}_i \cdot \mathbf{d}_j = \epsilon_{ijk}\omega_k$, for some ω_i. Let $\boldsymbol{\omega} = \omega_i \mathbf{d}_i$. The vector $\boldsymbol{\omega}(s)$, sometimes called the spin vector, then satisfies $\dot{\mathbf{d}}_i = \boldsymbol{\omega} \times \mathbf{d}_i$. The expression for $\mathbf{S}$ can be simplified by setting $\mathbf{R} = R_i\mathbf{d}_i = X\mathbf{d}_1 + Y\mathbf{d}_2$. Then $\dot{\mathbf{R}} = \boldsymbol{\omega} \times \mathbf{R}$, and

$$\mathbf{S} = \int_{\mathcal{C}} dR_1 dR_2\ \rho\mathbf{R} \times (\boldsymbol{\omega} \times \mathbf{R}) = \rho I_{ij}\omega_j \mathbf{d}_i \tag{2.13}$$

where I_{ij} is the inertia tensor of the undeformed cross section

$$I_{ij} = \int_{\mathcal{C}} dR_1 dR_2\ \left(R^2\delta_{ij} - R_i R_j\right)$$

The inertia tensor is diagonal in these coordinates

$$I_{ij} = \operatorname{diag}(I_1, I_2, I_3) = \operatorname{diag}(I_1, I_2, I_1 + I_2)$$

where I_1 and I_2 are the principal moments of inertia of the cross section $\mathcal{C}$ and $I_3 = I_1 + I_2$ by the perpendicular axis theorem

$$I_1 = \int_{\mathcal{C}} dXdY\ X^2, \qquad I_2 = \int_{\mathcal{C}} dXdY\ Y^2$$

Calculating the moment $\mathbf{M}$ and force $\mathbf{F}$ in the rod requires solving the equations of elasticity to find $\mathbf{u}^0(X, Y, s)$. The strain tensor of $\boldsymbol{\phi}$ depends on $\mathbf{u}^0$ and the derivative of the $\{\mathbf{d}_i\}$ frame. Analogous to the definition of $\boldsymbol{\omega}$, the s-derivative of the frame is given in terms of the curvature vector $\boldsymbol{\kappa}(s)$ which satisfies $\mathbf{d}_i' = \boldsymbol{\kappa} \times \mathbf{d}_i$ and we set

$\boldsymbol{\kappa} = \kappa_i \mathbf{d}_i$. The strain tensor to $O(\alpha^2)$ in the $\{\mathbf{d}_i\}$ basis is therefore

$$\epsilon_{ij} = \frac{1}{2}\begin{pmatrix} 2\partial_1 u_1^0 & \partial_1 u_2^0 + \partial_2 u_1^0 & -\kappa_3 Y + \partial_1 u_3^0 \\ \partial_1 u_2^0 + \partial_2 u_1^0 & 2\partial_2 u_2^0 & \kappa_3 X + \partial_2 u_3^0 \\ -\kappa_3 Y + \partial_1 u_3^0 & \kappa_3 X + \partial_2 u_3^0 & 2(\epsilon - \kappa_2 X + \kappa_1 Y) \end{pmatrix} + O(\alpha^2)$$

where $u_i^0 = \mathbf{u}^0 \cdot \mathbf{d}_i$. The stress tensor follows from (2.8), and $\mathbf{u}^0$ can be obtained by solving the time independent elasticity equations (2.9) over each cross section. The details of this calculation can be found in Ref. [33]. Here, we state the final result for $\mathbf{u}^0$, in the case where the cross sections are disks of radius h

$$u_1^0 = -\nu\epsilon X - \nu XY\kappa_1(s) + \frac{1}{2}\nu(X^2 - Y^2)\kappa_2(s) + h\,O(\alpha^2) \tag{2.14a}$$

$$u_2^0 = -\nu\epsilon Y + \nu XY\kappa_2(s) + \frac{1}{2}\nu(X^2 - Y^2)\kappa_1(s) + h\,O(\alpha^2) \tag{2.14b}$$

$$u_3^0 = h\,O(\alpha^2) \tag{2.14c}$$

When $\mathcal{C}$ is a disk, u_3^0 vanishes to leading order, meaning that the deformed cross sections are approximately planar. Using (2.14), the stress tensor for $\boldsymbol{\phi}$ is

$$\sigma_{ij} = \begin{pmatrix} 0 & 0 & -\mu\kappa_3 Y \\ 0 & 0 & \mu\kappa_3 X \\ -\mu\kappa_3 Y & \mu\kappa_3 X & E(\epsilon + \kappa_1 Y - \kappa_2 X) \end{pmatrix} + O(\alpha^2) \tag{2.15}$$

Substituting this into (2.5) and (2.2) gives constitutive laws for the moment and force distribution within the rod. The moment relation is

$$\begin{aligned} \mathbf{M} &= \int_{\mathcal{C}(s)} \epsilon_{ijk}\phi_j^0\sigma_{kl}\,dS_l \\ &= \int_{\mathcal{C}} \epsilon_{ijk} X_j \sigma_{k3}\,dXdY + O(\alpha) \\ &= EI_1\kappa_1\mathbf{d}_1 + EI_2\kappa_2\mathbf{d}_2 + \mu J\kappa_3\mathbf{d}_3 + O(\alpha) \end{aligned} \tag{2.16}$$

where I_1 and I_2 are the principal moments of inertia and J is the moment of twist,

which in general depends on u_3^0. The corresponding force relation is

$$\mathbf{F} = \int_{\mathcal{C}(s)} \sigma_{ij}\, dS_j = EA\epsilon \mathbf{d}_3 + O(\alpha) \tag{2.17}$$

The fact that some components of $\mathbf{F}$ vanish to leading order indicates that these components are unknowns that must instead be determined from the momentum and angular momentum conservation equations (2.7). In the inextensible case, all 3 components of $\mathbf{F}$ are unknowns, since $\epsilon \equiv 0$, whereas in the extensible case, only F_1 and F_2 are unknowns.

2.3 Kirchhoff equations

In this brief section, we summarize the results of the reduction from 3D elasticity, and state the key equations that we will use for the remainder of this thesis.

In the 1D theory, the rod is described by its centerline curve $\boldsymbol{x}(s,t)$ and the orthonormal material frame $\{\mathbf{d}_1(s,t), \mathbf{d}_2(s,t), \mathbf{d}_3(s,t)\}$, with $\boldsymbol{x}' = (1+\epsilon)\mathbf{d}_3$. The frame derivatives satisfy

$$\mathbf{d}_i' = \boldsymbol{\kappa} \times \mathbf{d}_i, \qquad \dot{\mathbf{d}}_i = \boldsymbol{\omega} \times \mathbf{d}_i$$

In the expression (2.16) for $\mathbf{M}$, the $\mathbf{d}_1$ and $\mathbf{d}_2$ components capture the bending response of the rod, and the $\mathbf{d}_3$ component captures the twisting response. Accordingly, let $\kappa(s)$ denote the geometric curvature of the rod instead of the magnitude of the curvature vector $\boldsymbol{\kappa}$. Since s is not an arc length parameter of the deformed rod, the curvature is

$$\kappa^2 = \left[(1+\epsilon)^{-1}\mathbf{d}_3'\right]^2 = \left(\kappa_1^2 + \kappa_2^2\right)(1 + O(\alpha))$$

Thus to leading order, $\kappa = \sqrt{\kappa_1^2 + \kappa_2^2}$. Let $\theta' = \kappa_3$ be the twist density, so θ can be thought of as a twist angle along the rod. In this thesis, we focus on rods with circular cross sections of radius h and area $A = \pi h^2$. The relevant moments of inertia

and twist are

$$I = I_1 = I_2 = \frac{1}{2} I_3 = \frac{1}{4}\pi h^4$$
$$J = 2I = \frac{1}{2}\pi h^4$$

The conservation laws (2.7), together with the constitutive laws (2.13) and (2.16), give the Kirchhoff equations for an inextensible elastic rod

$$\mathbf{F}' = \rho A \ddot{\boldsymbol{x}} \tag{2.18a}$$
$$\mathbf{M}' + \boldsymbol{x}' \times \mathbf{F} = \dot{\mathbf{S}} \tag{2.18b}$$

with constitutive laws

$$\mathbf{S} = \rho I \omega_1 \mathbf{d}_1 + \rho I \omega_2 \mathbf{d}_2 + 2\rho I \omega_3 \mathbf{d}_3 \tag{2.19a}$$
$$\mathbf{M} = EI\kappa_1 \mathbf{d}_1 + EI\kappa_2 \mathbf{d}_2 + \mu J \theta' \mathbf{d}_3 \tag{2.19b}$$

As discussed previously, the lack of a constitutive equation for $\mathbf{F}$ can be explained by counting the degrees of freedom of (2.18). There are 6 equations, and $\mathbf{M}, \mathbf{S}$ and $\boldsymbol{x}$ can all be written in terms of the frame $\{\mathbf{d}_i\}$, which has 3 degrees of freedom. Since $\mathbf{F}$ has 3 degrees of freedom, it is an unknown quantity that can be obtained by solving the equations. The Kirchhoff equations are therefore 6 equations for 6 unknowns, $\{\mathbf{d}_1, \mathbf{d}_2, \mathbf{d}_3\}$ and $\mathbf{F}$.

The Kirchhoff equations refer to the inextensible equations (2.18). In chapters 4 and 5, we will also consider the extensible Kirchhoff equations [100], where $\epsilon \neq 0$. In this case, equation (2.17) gives a constitutive equation for F_3, leaving F_1 and F_2 to be determined from the equations of motion. The dynamical equations are identical to (2.18), and there is a new constitutive law in addition to (2.19)

$$F_3 = EA\epsilon \tag{2.20}$$

In the extensible case, the 6 unknowns are $\{\mathbf{d}_1, \mathbf{d}_2, \mathbf{d}_3\}, \epsilon, F_1, F_2$.

2.4 Variational formulation

In this section we show how to obtain the (inextensible) Kirchhoff equations by varying an energy functional. This energy functional has the intuitive property of being quadratic in the derivatives of the degrees of freedom of the rod. However, the coefficients of the terms in this functional must ultimately be derived from 3D elasticity.

The Kirchhoff rod is described by its centerline curve $\boldsymbol{x}(s,t)$, and an orthonormal material frame $Q(s,t) = [\mathbf{d}_1(s,t), \mathbf{d}_2(s,t), \mathbf{d}_3(s,t)]$.

$$Q : [0, L] \times \mathbb{R} \to SO(3)$$
$$\boldsymbol{x} : [0, L] \times \mathbb{R} \to \mathbb{R}^3$$

where L is the length of the rod, and we assume $\boldsymbol{x}(s,t)$ is arc-length parametrized. Inextensibility imposes the additional constraint $\boldsymbol{x}' = \mathbf{d}_3$. Derivatives of the frame lie in the tangent space,

$$\dot{Q}, Q' \in T_Q SO(3) = \{A : A^T Q + Q^T A = 0\}$$

These derivatives can be identified with the Lie algebra $\mathfrak{so}(3)$ of 3×3 antisymmetric matrices, $Q'Q^T, \dot{Q}Q^T \in \mathfrak{so}(3)$. Thus we identify $Q', \dot{Q}$ with (pseudo) vectors $\boldsymbol{\kappa}, \boldsymbol{\omega}$ as follows

$$\kappa_i = \frac{1}{2}\epsilon_{ijk}(Q'Q^T)_{jk}, \qquad \omega_i = \frac{1}{2}\epsilon_{ijk}(\dot{Q}Q^T)_{jk}$$

As before, these vectors satisfy $\mathbf{d}_j' = \boldsymbol{\kappa} \times \mathbf{d}_j$ and $\dot{\mathbf{d}}_j = \boldsymbol{\omega} \times \mathbf{d}_j$. Equality of mixed partial derivatives further implies the following consistency equation

$$\dot{\boldsymbol{\kappa}} - \boldsymbol{\omega}' = \boldsymbol{\omega} \times \boldsymbol{\kappa} \tag{2.21}$$

Along with inertia tensor I_{ij}, it is convenient to define an elastic tensor G_{ij}

$$G_{ij} = \text{diag}\left(EI, EI, \mu J\right), \qquad I_{ij} = \text{diag}\left(I, I, 2I\right)$$

where the components are given in the $\{\mathbf{d}_i(s,t)\}$ basis. The moment $\mathbf{M}(s,t)$, and cross sectional angular momentum, $\mathbf{S}(s,t)$ can be written in terms of these tensors

$$M_i = G_{ij}\kappa_j, \qquad S_i = I_{ij}\omega_j$$

The potential energy of the rod is

$$\begin{aligned}\mathcal{E} &= \frac{1}{2}\int_0^L ds\left(\boldsymbol{\kappa}^T G\boldsymbol{\kappa} + 2\mathbf{F}\cdot(\boldsymbol{x}' - \mathbf{d}_3)\right) \\ &= \frac{1}{2}\int_0^L ds\left(EI\kappa^2 + \mu J\theta'^2 + 2\mathbf{F}\cdot(\boldsymbol{x}' - \mathbf{d}_3)\right)\end{aligned}$$

where $\mathbf{F}$(s,t) appears as a Lagrange multiplier enforcing the constraint $\boldsymbol{x}' = \mathbf{d}_3$. The kinetic energy is given by

$$\begin{aligned}\mathcal{T} &= \frac{1}{2}\int_0^L ds\left(\rho A\dot{\boldsymbol{x}}^2 + \boldsymbol{\omega}^T I\boldsymbol{\omega}\right) \\ &= \frac{1}{2}\int_0^L ds\left(\rho A\dot{\boldsymbol{x}}^2 + \rho I\omega_1^2 + \rho I\omega_2^2 + 2\rho I\omega_3^2\right)\end{aligned}$$

Consider the behavior of these energies under a perturbation

$$\mathbf{F} \mapsto \mathbf{F} + \delta\mathbf{F}, \quad \boldsymbol{x} \mapsto \boldsymbol{x} + \delta\boldsymbol{x}, \quad \mathbf{d}_i \mapsto \mathbf{d}_i + \delta\mathbf{d}_i = \mathbf{d}_i + \delta\boldsymbol{g}\times\mathbf{d}_i$$

The corresponding change in κ_i and ω_i is

$$\delta\kappa_i = \delta\boldsymbol{g}'\cdot\mathbf{d}_i, \qquad \delta\omega_i = \delta\dot{\boldsymbol{g}}\cdot\mathbf{d}_i \tag{2.22}$$

Assume that the boundary conditions (BCs) are such that

$$\left[\mathbf{F}\cdot\delta\boldsymbol{x}\right]_0^L = 0, \qquad \left[\mathbf{M}\cdot\delta\boldsymbol{g}\right]_0^L = 0$$

The change in the potential energy is

$$\begin{aligned}\delta\mathcal{E} &= \int_0^L ds\ \left(G_{ij}\kappa_i\delta\kappa_j + \delta\mathbf{F}\cdot(\boldsymbol{x}' - \mathbf{d}_3) + \mathbf{F}\cdot\delta\boldsymbol{x}' - \mathbf{F}\cdot\delta\mathbf{d}_3\right)\\ &= \int_0^L ds\ \left(M_i\delta\boldsymbol{g}'\mathbf{d}_i - \mathbf{F}\cdot\delta\boldsymbol{g}\times\mathbf{d}_3 + \mathbf{F}\cdot\delta\boldsymbol{x}' + (\boldsymbol{x}' - \mathbf{d}_3)\cdot\delta\mathbf{F}\right)\\ &= \int_0^L ds\ \left[(-\mathbf{M}' - \mathbf{d}_3\times\mathbf{F})\cdot\delta\boldsymbol{g} - \mathbf{F}'\cdot\delta\boldsymbol{x} + (\boldsymbol{x}' - \mathbf{d}_3)\cdot\delta\mathbf{F}\right]\end{aligned}$$

and the change in the kinetic energy is

$$\begin{aligned}\delta\mathcal{T} &= \int_0^L ds\ \left(\rho A\dot{\boldsymbol{x}}\cdot\delta\dot{\boldsymbol{x}} + I_{ij}\omega_i\delta\omega_j\right)\\ &= -\int_0^L ds\ \left(\rho A\ddot{\boldsymbol{x}}\cdot\delta\boldsymbol{x} - S_i\delta\dot{\boldsymbol{g}}\cdot\mathbf{d}_i\right)\\ &= -\int_0^L ds\ \left(\rho A\ddot{\boldsymbol{x}}\cdot\delta\boldsymbol{x} + \dot{\mathbf{S}}\cdot\delta\boldsymbol{g}\right)\end{aligned}$$

The change in the action is then given by

$$\begin{aligned}\delta S &= \int_0^T dt\,(\delta\mathcal{T} - \delta\mathcal{E})\\ &= \int_0^T dt\int_0^L ds\left[(\mathbf{F}' - \rho A\ddot{\boldsymbol{x}})\cdot\delta\boldsymbol{x} + \left(-\dot{\mathbf{S}} + \mathbf{M}' + \mathbf{d}_3\times\mathbf{F}\right)\cdot\delta\boldsymbol{g} - (\boldsymbol{x}' - \mathbf{d}_3)\cdot\delta\mathbf{F}\right]\end{aligned}$$

Setting $\delta S = 0$ yields the constraint $\boldsymbol{x}' = \mathbf{d}_3$ and the Kirchhoff equations (2.18).

2.5 Force-torque formulation

Reformulating the Kirchhoff equations (2.18) in terms of the more physical degrees of freedom $\{\boldsymbol{x}(s,t), \theta(s,t)\}$ leads to a system of equations that is more computationally tractable. This description produces a force equation for the centerline curve $\boldsymbol{x}$ and a scalar torque equation for the twist angle θ. The forces and torques can further be broken down into terms arising from gradients of the bend, twist and stretch energies. This formulation is also particularly amenable to numerical simulation. For example, a discretized energy can be written in terms of a discretized rod, and fores and torques

can be calculated by taking the relevant gradients of the discretized energy. This is the principle underlying the numerical framework for simulating rods introduced in Refs. [14, 13], which we utilize here. In this section, we derive the continuum analog of these discrete equations for the inextensible and extensible models, and explain their relationship to the Kirchhoff equations.

Inextensible case

Recall the Kirchhoff equations (2.18)

$$\mathbf{F}' = \dot{\mathbf{p}}, \qquad \mathbf{M}' + \boldsymbol{x}' \times \mathbf{F} = \dot{\mathbf{S}}$$

where $\mathbf{p} = \rho A \dot{\boldsymbol{x}}$ is used to simplify notation. Reformulating (2.18) involves eliminating $\mathbf{F}$. To do this, we introduce the Frenet frame of the rod $\{\mathbf{t}, \mathbf{n}, \mathbf{b}\}$, which consists of the unit tangent vector $\mathbf{t}$, the unit normal $\mathbf{n}$ which is defined to be parallel to $\mathbf{t}'$, and the unit binormal $\mathbf{b}$ defined by $\mathbf{b} = \mathbf{t} \times \mathbf{n}$. The Frenet frame satisfies

$$\mathbf{t}' = \kappa \mathbf{n}, \qquad \mathbf{n}' = -\kappa \mathbf{t} + \tau \mathbf{b}, \qquad \mathbf{b}' = -\tau \mathbf{n} \tag{2.23}$$

where κ is the curvature of the curve $\boldsymbol{x}$ and τ is the torsion. Observe that $\mathbf{t} = \mathbf{d}_3$, and $\boldsymbol{\kappa} = \kappa \mathbf{b} + \theta' \mathbf{t}$. The moment and angular momentum vectors are

$$\mathbf{M} = EI\kappa \mathbf{b} + \mu J \theta' \mathbf{t}$$
$$\mathbf{S} = \rho I \mathbf{t} \times \dot{\mathbf{t}} + 2\rho I \omega_3 \mathbf{t}$$

The scalar torque equation follows from taking the moment equation (2.18b) in the $\mathbf{t}$ direction, $\mathbf{M}' \cdot \mathbf{t} = \dot{\mathbf{S}} \cdot \mathbf{t}$

$$\mu J \theta'' = 2\rho I \dot{\omega}_3 \tag{2.24}$$

To get the force equation, rewrite $\mathbf{F}$ in terms of $\mathbf{M}$ by taking derivatives of $\mathbf{M}' - \dot{\mathbf{S}}$

$$\mathbf{t} \times \left(\mathbf{M}' - \dot{\mathbf{S}}\right) = \mathbf{t} \times (\mathbf{F} \times \mathbf{t}) = \mathbf{F} - (\mathbf{F} \cdot \mathbf{t})\mathbf{t}$$
$$\mathbf{b} \cdot \left(\mathbf{M}'' - \dot{\mathbf{S}}'\right) = \mathbf{b} \cdot (\dot{\mathbf{p}} \times \mathbf{t} + \mathbf{F} \times \kappa\mathbf{n}) = -\dot{\mathbf{p}} \cdot \mathbf{n} + \kappa\mathbf{F} \cdot \mathbf{t}$$

Thus

$$\mathbf{F} = \mathbf{t} \times \mathbf{M}' - \mathbf{t} \times \dot{\mathbf{S}} + \frac{1}{\kappa}\left(\mathbf{b} \cdot \left(\mathbf{M}'' - \dot{\mathbf{S}}'\right) + \dot{\mathbf{p}} \cdot \mathbf{n}\right)\mathbf{t}$$

Decompose $\mathbf{F}$ as follows

$$\mathbf{F}_{(0)} = \mathbf{t} \times \mathbf{M}' = EI\left(\mathbf{t} \times (\kappa\mathbf{b})'\right) + \mu J\theta'\kappa\mathbf{b}$$
$$\mathbf{F}_{(1)} = -\mathbf{t} \times \dot{\mathbf{S}} + \frac{1}{\kappa}\left(\mathbf{b} \cdot \left(\mathbf{M}'' - \dot{\mathbf{S}}'\right) + \dot{\mathbf{p}} \cdot \mathbf{n}\right)\mathbf{t}$$

Combining (2.24) with the expressions $\mathbf{F}$ gives the force-torque formulation of the Kirchhoff equations

$$\left[EI\left(\mathbf{t} \times (\kappa\mathbf{b})'\right) + \mu J\theta'\kappa\mathbf{b}\right]' + \mathbf{F}'_{(1)} = \rho A\ddot{\boldsymbol{x}} \tag{2.25a}$$
$$\mu J\theta'' = 2\rho I\dot{\omega}_3 \tag{2.25b}$$

The force $\mathbf{F}_{(0)}$ and the scalar torque can be obtained by taking gradients of the energy, using the results of the previous section. The force $\mathbf{F}_{(1)}$ can then be interpreted as the constraint force fixing $|\boldsymbol{x}'| = 1$ and imposing inextensibility. The bending and twisting energies are

$$\mathcal{E}_b = \frac{1}{2}\int_0^L ds\; EI\kappa^2, \qquad \mathcal{E}_t = \frac{1}{2}\int_0^L ds\; \mu J\theta'^2 \tag{2.26}$$

In section 2.4, these energies were perturbed by $\boldsymbol{x} \mapsto \boldsymbol{x} + \delta\boldsymbol{x}$ and $\mathbf{d}_i \mapsto \mathbf{d}_i + \delta\boldsymbol{g} \times \mathbf{d}_i$. Now, we vary the energies with respect to $\boldsymbol{x}$ and θ instead. This requires writing $\delta\boldsymbol{g}$

in terms of $\delta\boldsymbol{x}$ and $\delta\theta$. The key result is

$$\delta\boldsymbol{g} = \mathbf{t} \times \delta\mathbf{t} + \delta\theta\mathbf{t}$$

The expression for $\delta\boldsymbol{g}$ comes from considering how the frame changes when $\boldsymbol{x}$ or θ changes. Varying θ without the centerline corresponds to a change only in the twist of the frame, given by the $\mathbf{t}$ component of $\delta\boldsymbol{g}$. Varying $\boldsymbol{x}$ without θ will parallel transport the frame in the direction of variation. In other words, if $\delta\theta = 0$, then $\delta\boldsymbol{g} \cdot \mathbf{t} = 0$. Together, these observations show that $\delta\boldsymbol{g} \cdot \mathbf{t} = \delta\theta$. For the part of $\delta\boldsymbol{g}$ normal to $\mathbf{t}$, observe that $\delta\boldsymbol{g}$ should satisfy $\delta\mathbf{t} = \delta\boldsymbol{g} \times \mathbf{t}$ which is indeed true of the above expression (because $\delta\mathbf{t} \cdot \mathbf{t} = 0$ since $\mathbf{t} \cdot \mathbf{t} = 1$). Finally, observe that

$$\delta\mathbf{t} = \delta\left(\frac{\boldsymbol{x}'}{1+\epsilon}\right) = \frac{1}{1+\epsilon}\delta\boldsymbol{x}' - \frac{1}{1+\epsilon}(\mathbf{t} \cdot \delta\boldsymbol{x}')\mathbf{t}$$

where the stretch ϵ is included since the perturbation is unconstrained, so $\boldsymbol{x}' + \delta\boldsymbol{x}'$ does not necessarily have unit length. The final expression for $\delta\boldsymbol{g}$ is

$$\delta\boldsymbol{g} = \frac{1}{1+\epsilon}\mathbf{t} \times \delta\boldsymbol{x}' + \delta\theta\mathbf{t} \tag{2.27}$$

Use (2.22) to vary the energies

$$\delta\mathcal{E}_b + \delta\mathcal{E}_t = \int_0^L G_{ij}\kappa_i\delta\kappa_j = \int_0^L ds\; G_{ij}\kappa_i\delta\boldsymbol{g}' \cdot \mathbf{d}_j = \int_0^L ds\; (EI\kappa\mathbf{b} \cdot \delta\boldsymbol{g}' + \mu J\theta'\mathbf{t} \cdot \delta\boldsymbol{g}')$$

Separating the bending and twisting contribution gives

$$\begin{aligned}\delta\mathcal{E}_b = \int_0^L ds\; EI\kappa\mathbf{b} \cdot \delta\boldsymbol{g}' &= -\int_0^L ds\; EI(\kappa\mathbf{b})' \cdot \left(\frac{1}{1+\epsilon}\mathbf{t} \times \delta\boldsymbol{x}' + \delta\theta\mathbf{t}\right) \\ &= \int_0^L ds\; EI\left(\frac{1}{1+\epsilon}\mathbf{t} \times (\kappa\mathbf{b})'\right) \cdot \delta\boldsymbol{x}'\end{aligned}$$

and

$$\delta\mathcal{E}_t = \int_0^L ds\ \mu J\theta'\mathbf{t}\cdot\delta\boldsymbol{g}' = -\int_0^L ds\ \mu J\left(\theta''\mathbf{t}+\theta'\kappa\mathbf{n}\right)\cdot\left(\frac{1}{1+\epsilon}\mathbf{t}\times\delta\boldsymbol{x}'+\delta\theta\mathbf{t}\right)$$
$$= \int_0^L ds\ \mu J\left(\frac{1}{1+\epsilon}\theta'\kappa\mathbf{b}\right)\cdot\delta\boldsymbol{x}' - \mu J\theta''\delta\theta$$

Taking functional derivatives of the energies and imposing the constraint $\epsilon = 0$ gives

$$\begin{aligned}\frac{\delta\mathcal{E}_b}{\delta\boldsymbol{x}} &= -EI\left(\mathbf{t}\times(\kappa\mathbf{b})'\right)' & \frac{\delta\mathcal{E}_b}{\delta\theta} &= 0\\ \frac{\delta\mathcal{E}_t}{\delta\boldsymbol{x}} &= -\mu J\left(\theta'\kappa\mathbf{b}\right)' & \frac{\delta\mathcal{E}_t}{\delta\theta} &= -\mu J\theta''\end{aligned} \tag{2.28}$$

These energy gradients correspond to force and torque terms in (2.25), and also provide insight into the coupling between bend and twist modes. The bending energy produces forces on $\boldsymbol{x}$ and the twist energy produces torques on θ as expected. However, the twist energy is also responsible for forces on the centerline. Thus moving the rod without explicitly twisting it can still change the twist energy. The force-torque equations can be written in terms of the energy gradients

$$-\frac{\delta\mathcal{E}_b}{\delta\boldsymbol{x}} - \frac{\delta\mathcal{E}_t}{\delta\boldsymbol{x}} + \mathbf{F}'_{(1)} = \rho A\ddot{\boldsymbol{x}} \tag{2.29a}$$

$$-\frac{\delta\mathcal{E}_t}{\delta\theta} = 2\rho I\dot{\omega}_3 \tag{2.29b}$$

The state of the rod at time t is given by $\{\boldsymbol{x}(s,t),\theta(s,t)\}$. To get a numerical framework from the above equations, the additional twist compatibility equation relating ω_3 and θ is needed

$$\omega_3' + \mathbf{t}\cdot\left(\mathbf{t}'\times\dot{\mathbf{t}}\right) = \dot{\theta}' \tag{2.29c}$$

This follows from the $\mathbf{t}$ component of the consistency equation (2.21)

$$\dot{\boldsymbol{\kappa}} - \boldsymbol{\omega}' = \boldsymbol{\omega}\times\boldsymbol{\kappa}$$

To simulate inextensible rods, we use a discretized version of these equations, as developed in Refs. [14, 13]. The procedure can be roughly summarized as follows. At time t, the quantities $\{\boldsymbol{x}(s,t), \theta(s,t), \omega_3(s,t)\}$ are stored. The forces and torques can be calculated by taking gradients of $\mathcal{E}_b[\boldsymbol{x}, \theta]$ and $\mathcal{E}_t[\boldsymbol{x}, \theta]$. Using some time-stepping scheme, ω_3 can be updated using these energy gradients. Updating $\boldsymbol{x}$ is a two step process. First, the energy gradient forces are added. Then the constraint force $\mathbf{F}_{(1)}$ is implemented by projecting the partially updated $\boldsymbol{x}$ onto the constraint manifold of curves with $|\boldsymbol{x}'| = 1$. The details of this manifold projection step can be found in Ref. [14]. Finally, θ is updated using the updated ω_3 and $\boldsymbol{x}$. Chapter 3 focuses on inextensible rods, and uses this algorithm.

Extensible case

As in the inextensible case, we begin by reformulating the Kirchhoff equations as a force equation and a scalar torque equations. The forces and torques will then be rewritten in terms of energy gradients. When stretching is included, the Kirchhoff equations (2.18) are augmented by the addition constitutive law (2.20)

$$\mathbf{F}' = \rho A \ddot{\boldsymbol{x}}, \qquad \mathbf{M}' + \boldsymbol{x}' \times \mathbf{F} = \dot{\mathbf{S}}, \qquad \mathbf{F} \cdot \mathbf{t} = EA\epsilon$$

Since s is no longer an arc length parameter, the Frenet frame now satisfies

$$\mathbf{t}' = (1+\epsilon)\kappa\mathbf{n}, \qquad \mathbf{n}' = -(1+\epsilon)\kappa\mathbf{t} + (1+\epsilon)\tau\mathbf{b}, \qquad \mathbf{b}' = -(1+\epsilon)\tau\mathbf{n}$$

The relationship between the geometric curvature and the frame derivative $\boldsymbol{\kappa}$, defined by $\mathbf{d}_i' = \boldsymbol{\kappa} \times \mathbf{d}_i$, is now

$$\kappa^2 = \frac{1}{(1+\epsilon)^2}\left(\kappa_1^2 + \kappa_2^2\right)$$

Therefore, to leading order, the moment has the same form as in the inextensible case, $\mathbf{M} = EI\kappa\mathbf{b} + \mu J\theta'\mathbf{t}$. The scalar torque equation, $\mathbf{M}' \cdot \mathbf{t} = \dot{\mathbf{S}} \cdot \mathbf{t}$, is also the same

as (2.24)

$$\mu J\theta'' = 2\rho I\dot{\omega}_3$$

To eliminate $\mathbf{F}$, observe that the component $\mathbf{F}$ normal to $\mathbf{t}$ can be obtained from the moment equation (2.18b)

$$\frac{1}{1+\epsilon}\mathbf{t}\times\left(\mathbf{M}'-\dot{\mathbf{S}}\right)=\mathbf{t}\times(\mathbf{F}\times\mathbf{t})=\mathbf{F}-(\mathbf{F}\cdot\mathbf{t})\mathbf{t}$$

The component of $\mathbf{F}$ in the $\mathbf{t}$ direction is given by the constitutive law (2.20)

$$\mathbf{F}=\frac{1}{1+\epsilon}\mathbf{t}\times\left(\mathbf{M}'-\dot{\mathbf{S}}\right)+EA\epsilon\mathbf{t}$$

It can be argued that $\mathbf{t}\times\dot{\mathbf{S}}$ is small and can be neglected [33, 64, 74, 75]. Indeed this approximation was suggested by Kirchhoff himself [33]. This gives

$$\begin{aligned}\mathbf{F}&=\frac{1}{1+\epsilon}\mathbf{t}\times\mathbf{M}'+EA\epsilon\mathbf{t}\\&=EI\left(\mathbf{t}\times(\kappa\mathbf{b})'\right)+\mu J\theta'\kappa\mathbf{b}+EA\epsilon\mathbf{t}\end{aligned}$$

where the components of $\mathbf{F}$ in the plane normal to $\mathbf{t}$ are given to leading order in α (2.12). This is equivalent to neglecting the effect of bend-stretch and twist-stretch coupling. The force can be decomposed in terms of energy gradients

$$\mathcal{E}_b=\frac{1}{2}\int_0^L ds\ EI\kappa^2,\qquad \mathcal{E}_t=\frac{1}{2}\int_0^L ds\ \mu J\theta'^2,\qquad \mathcal{E}_s=\frac{1}{2}\int_0^L ds\ EA\epsilon^2 \tag{2.30}$$

The gradients of the bend and twist energies produce the transverse components of $\mathbf{F}$ to leading order, as in (2.28). To vary the stretching energy, observe that

$$\delta\epsilon=\delta\left(\mathbf{t}\cdot\boldsymbol{x}'-1\right)=\delta\mathbf{t}\cdot\boldsymbol{x}'+\mathbf{t}\cdot\delta\boldsymbol{x}'=\mathbf{t}\cdot\delta\boldsymbol{x}'$$

where $\delta\mathbf{t}\cdot\boldsymbol{x}' = 0$ because $\delta\mathbf{t}$ is perpendicular to $\mathbf{t}$ and $\boldsymbol{x}'$ which follows from $\mathbf{t}\cdot\mathbf{t} = 0$. The derivatives of the stretching energy are therefore

$$\frac{\delta\mathcal{E}_s}{\delta\boldsymbol{x}} = -EA\left(\epsilon\mathbf{t}\right)', \qquad \frac{\delta\mathcal{E}_s}{\delta\theta} = 0 \tag{2.31}$$

The force equation, $\mathbf{F}' = \rho A\ddot{\boldsymbol{x}}$, and torque equation, now take the form

$$-\frac{\delta\mathcal{E}_b}{\delta\boldsymbol{x}} - \frac{\delta\mathcal{E}_t}{\delta\boldsymbol{x}} - \frac{\delta\mathcal{E}_s}{\delta\boldsymbol{x}} = \rho A\ddot{\boldsymbol{x}} \tag{2.32a}$$

$$-\frac{\delta\mathcal{E}_t}{\delta\theta} = 2\rho I\dot{\omega}_3 \tag{2.32b}$$

$$\omega_3' + \mathbf{t}\cdot\left(\mathbf{t}'\times\dot{\mathbf{t}}\right) = \dot{\theta}' \tag{2.32c}$$

The twist compatibility equation is included for completeness. It is possible to modify these equations to include the coupling between stretch and the other modes. However, provided the stretching remains small, the resulting dynamics will be approximately the same as above.

2.6 Overdamped dynamics

In this thesis, the extensible Kirchhoff equations are only used in the overdamped limit, where inertia is negligible. To model overdamped dynamics, damping terms must be introduced on the RHS of (2.32). Motivated by hydrodynamics, we choose damping terms depending on the second spatial derivatives of the velocities $\dot{\boldsymbol{x}}$ and $\boldsymbol{\omega}$. In the force equation, the natural choice is a term proportional to $\dot{\boldsymbol{x}}''$. For the torque equation, observe that

$$\mathbf{S} = \rho I\mathbf{t}\times\dot{\mathbf{t}} + 2\rho I\omega_3\mathbf{t}$$

$$\dot{\mathbf{S}}\cdot\mathbf{t} = \rho J\mathbf{t}\cdot\frac{d}{dt}\left(\omega_3\mathbf{t}\right)$$

This suggests a twist damping term of the form $(\omega_3 \mathbf{t})'' \cdot \mathbf{t}$. Combining this with (2.32) gives a set of equations describing overdamped fibers

$$\frac{\delta \mathcal{E}_b}{\delta \boldsymbol{x}} + \frac{\delta \mathcal{E}_t}{\delta \boldsymbol{x}} + \frac{\delta \mathcal{E}_s}{\delta \boldsymbol{x}} = \eta A \dot{\boldsymbol{x}}'' \tag{2.33a}$$

$$\frac{\delta \mathcal{E}_t}{\delta \theta} = 2\eta I (\omega_3 \mathbf{t})'' \cdot \mathbf{t} \tag{2.33b}$$

$$\omega_3' + \mathbf{t} \cdot \left(\mathbf{t}' \times \dot{\mathbf{t}} \right) = \dot{\theta}' \tag{2.33c}$$

where η is a damping coefficient and the factors of A and $2I$ are included on dimensional grounds. These equations are used to model the softer fibers studied in chapters 4 and 5.

Chapter 3

Fragmentation

Fracture processes are a frequent occurrence in nature, from earthquakes to broken trees and bones. Understanding and controlling fracture dynamics remains one of the foremost theoretical and practical challenges in material science and physics. In this chapter, we investigate the fracture and fragmentation behavior of elongated brittle objects, such as vaulting poles or long fibers. This problem goes back to Feynman who observed that dry spaghetti almost always break into three or more pieces when exposed to large bending stresses. While bending-induced fracture is fairly well understood, much less is known about the effects of twist. Through experimental and theoretical results, we demonstrate that twisting enables fracture control by utilizing the different propagation speeds of twist and bending waves. In particular, we show that twist can be used to achieve robust binary fracture of an elastic rod. Additionally, we show that varying the quench speed at which the ends of the elastic rod are brought together also provides control over the fragmentation process.

3.1 Breaking spaghetti

Elastic rod fracture plays a critical role in a range of systems, from columns [60] to trees [39, 142, 2] and bones [113]. When placed under extreme stresses, the structural stability of such materials becomes ultimately limited by the fracture behaviors of their individual fibrous or tubular constituents. Owing to their central practical

importance in engineering, elastic rod fracture and crack propagation have been intensively studied for more than a century both experimentally [16, 6, 45] and theoretically [59, 112, 41]. Recent advances in video microscopy and microscale force manipulation [35, 102] have extended the scope of fracture studies to the microworld [42, 32], revealing causes and effects of structural failure in the axonal cytoskeleton [132], fibroblasts [104], bacterial flagellar motors [4], active liquid crystals [122] and multiwalled carbon nanotubes [145, 98].

Built on Sir Neville Mott's foundational studies on the fragmentation of ring shaped explosives [99], theoretical work on elastic rod fracture has flourished over the past two decades [144, 146, 6, 45, 94, 140]. Yet, many basic aspects of the fracture phenomenology remain poorly understood. Bending induced fragmentation has been thoroughly investigated in the limits of adiabatically slow [6] and diabatically fast [45] energy injection, but the roles of twist and quench rate on the fracture process have yet to be clarified. These two fundamental issues are directly linked to a famous observation by Richard Feynman [131], who noted that dry spaghetti, when brought to fracture by holding the ends and moving them towards each other, appears almost always to break into at least three pieces. The phenomenon of non-binary elastic rod fracture is also well known to pole vaulters, with a notable instance occurring during the 2012 Olympic Games [22]. Below, we will revisit and generalize Feynman's experiment, in order to investigate systematically how twist and quench dynamics influence the elastic fragmentation cascade [6, 45]. Specifically, we will demonstrate two complementary quench protocols for controlled binary fracture of brittle elastic rods, thereby identifying conditions under which Feynman's fragmentation conjecture becomes invalid. Our experimental observations are in good agreement with numerical predictions from a nonlinear elasticity model, and can be rationalized through analytical scaling arguments.

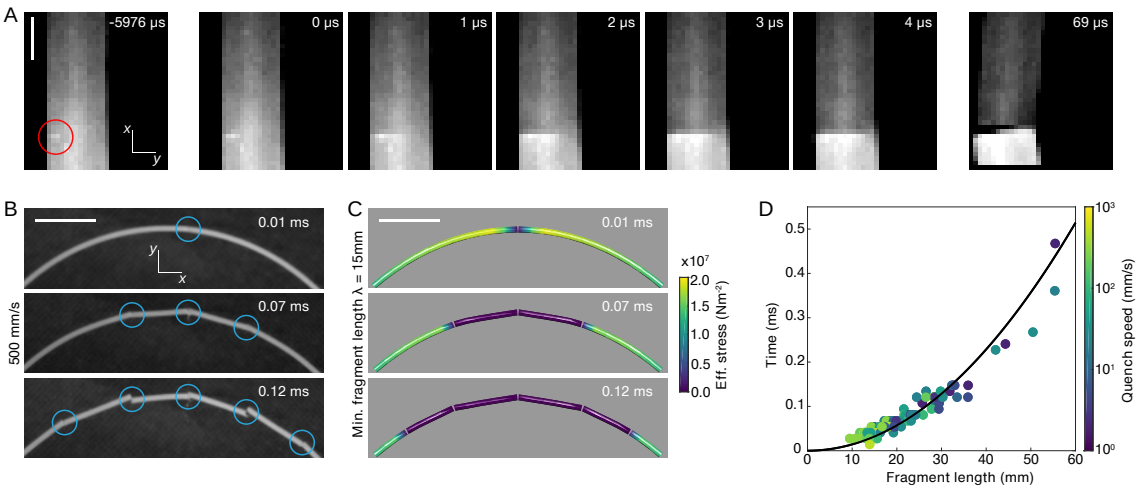

Figure 3-1: **Fragmentation is a multistage process.** (**A**) High speed images show first fracture. A crack nucleates and grows initially on a relatively slow millisecond-timescale. Catastrophic failure occurs at a critical crack depth (the Griffith length) leading to rapid crack propagation within $\sim 10\,\mu$s. Subsequent separation of the two fragments is governed by another slower timescale associated with bending waves. (**B**) High speed images show sequential fractures separated by a characteristic distance. Fragments are ejected with considerable angular velocity, in agreement with the observation of non-simultaneous fractures. (**C**) Simulations show bending waves originating at the point of first fracture creating additional fractures separated by at least the minimum fragment length λ. The predicted fracture times agree with (B). In simulations, fragments are frozen after fracture and do not evolve further. (**D**) The time between the first two fractures and the resulting fragment length lie along the space-time path of the location of maximum bending stress (solid line) (sample size $n = 110$). The distance between the first two fractures depends on quench speed but is bounded from below. Diameter of rod and gaps between fragments enhanced for visualization in (C). Scale bar in (A) 1 mm. Scale bars in (B,C) 15 mm.

3.2 Validity of Kirchhoff model

Time scales in fragmentation

Revisiting Feynman's experiment, we monitor the fracture dynamics of dry spaghetti using high-speed imaging at frame rates ranging from 1972 frames per second (fps) to 1000000 fps (Fig. 3-1). The highest time resolution data show that already a basic fracture event involves several timescales, from initial crack nucleation and growth, to catastrophic failure (Fig. 3-1A). The initial nucleation phase is relatively slow, lasting ~ 10 ms. It is followed by a fast catastrophic phase ($\sim 10\,\mu$s), during which

the crack propagates rapidly close to the material speed of sound. The creation of multiple fragments via a fragmentation cascade is then governed by the slower propagation timescale of elastic bending waves (Fig. 3-1B,C), as shown by Audoly and Neukirch [6]. Our goal is to control the fragmentation dynamics on this slower elastic timescale, which can be treated accurately within the Kirchhoff theory (Fig. 3-1B,C).

Kirchhoff model with twist damping

In this chapter, we model an elastic rod using the inextensible Kirchhoff equations (2.18) together with a phenomenological twist damping term. The position of the rod at time t is described by its arc length parametrized centerline $\boldsymbol{x}(s,t)$, $s \in [0, L]$, and an orthonormal material frame $\{\mathbf{d}_1(s,t), \mathbf{d}_2(s,t), \mathbf{d}_3(s,t)\}$ with $\mathbf{d}_3 = \boldsymbol{x}'$. The rod has uniform density ρ, is naturally straight and inextensible with circular cross section with radius h. The rod's dynamics are governed by the damped Kirchhoff equations

$$\mathbf{F}'' = \rho A \ddot{\mathbf{d}}_3 \tag{3.1a}$$

$$\mathbf{M}' + \mathbf{d}_3 \times \mathbf{F} = \dot{\mathbf{S}} + 4b\rho I \omega_3 \mathbf{d}_3 \tag{3.1b}$$

where the moment $\mathbf{M}$ and cross sectional angular momentum $\mathbf{S}$ are given by (2.20)

$$\mathbf{M}(s,t) = EI\kappa_1 \mathbf{d}_1 + EI\kappa_2 \mathbf{d}_2 + \mu J \kappa_3 \mathbf{d}_3$$
$$\mathbf{S}(s,t) = \rho I \omega_1 \mathbf{d}_1 + \rho I \omega_2 \mathbf{d}_2 + 2\rho I \omega_3 \mathbf{d}_3$$

and $\mathbf{d}_i' = \boldsymbol{\kappa} \times \mathbf{d}_i$, $\dot{\mathbf{d}}_i = \boldsymbol{\omega} \times \mathbf{d_i}$. The cross sections are circular, so $J = 2I = \pi h^2/2$. The Young's modulus E and the shear modulus μ are related by $E/\mu = 2(1+\nu)$, where ν is the Poisson's ratio. Most materials have $0.2 < \nu < 0.5$. The final term on the RHS of (3.1b) denotes damping of twist modes with damping parameter b. Our measurements of this parameter using a torsion pendulum indicate that twist is approximately critically damped. Since the timescale for the entire fracture cascade is an order of magnitude smaller than the time period of the fundamental bending

mode, we do not need to include bending damping terms in our analysis. The average material properties of our experimental samples are $\rho = 1.5 \pm 0.1\,\mathrm{g/cm}^3$, $E = 3.8 \pm 0.3\,\mathrm{GPa}$, $\mu = 1.5 \pm 0.2\,\mathrm{GPa}$, and by considering mean values for E, μ we obtain $\nu = 0.3 \pm 0.1$. We present fracture data for rods of radius $2h = 1.4 \pm 0.05\,\mathrm{mm}$ and $2h = 1.7 \pm 0.05\,\mathrm{mm}$. Finally, we note that the Kirchhoff equations do not account for certain shear effects described by Timoshenko beam theory. Indeed, the Timoshenko theory does provide a more accurate description of bending waves with large wavenumber compared to rod radius. However, to describe fracture, we will only need to consider wavenumbers k with $kh/2\pi < 0.1$. In this regime, the difference between the Timoshenko and Kirchhoff beam theories is negligible [54].

Measurement of twist damping

We measure the damping parameter b by observing the damping of a torsion pendulum made by attaching to the rod an approximately cylindrical mass with height h_0 and mass moment of inertia I_0. As above, the rod has length L. Note that the dimensions of I_0 are $(\mathrm{Mass}) \times (\mathrm{Length})^2$ in contrast to the moment of inertia I of the rod cross section, which has units $(\mathrm{Length})^4$. To derive the equation of motion for the torsion pendulum we begin with the $\mathbf{d}_3$ component of the damped twist equation (3.1b)

$$2b_0\omega_3 + 2\rho I\dot{\omega}_3 = 2\mu I\theta''$$

where $b_0 = 2\rho I$ is used to simplify notation, and $\theta' = \kappa_3$. The torsion pendulum rotates around its axis, so $\dot{\mathbf{d}}_3 = 0$ and $\boldsymbol{\kappa}' = 0$ which means $\boldsymbol{\omega} = \omega_3\mathbf{d}_3$ and $\boldsymbol{\kappa} = \theta'\mathbf{d}_3$. Equality of mixed partial derivatives (see (2.21)) therefore gives $\dot{\theta} = \omega_3$. The torsion pendulum can thus be described by θ

$$2b_0\dot{\theta} + 2\rho I\ddot{\theta} = 2\mu I\theta''$$

Consider a discretization of the rod in steps of size h_0. Let $\theta(kh_0, t) = \theta_k(t)$ for $k = 0, 1, 2, ..., L/h = N$. In particular, $\theta_0(t) \equiv 0$. Points θ_i and θ_{i+1} are connected by an elastic cylinder with radius h and height h_0. The discretized undamped Lagrangian is thus given by:

$$\sum_{i=1}^{N} \rho I h_0 \dot{\theta}^2 - \sum_{i=1}^{N} \frac{\mu I}{h_0} (\theta_i - \theta_{i-1})^2$$

Equations of motion for each θ_i follow from the Lagrangian

$$2b_0 h_0 \dot{\theta}_i + 2\rho I h_0 \ddot{\theta}_i + \frac{2\mu I}{h_0} (2\theta_i - \theta_{i-1} - \theta_{i+1}) = 0 \qquad \text{for } i < N$$

$$2b_0 h_0 \dot{\theta}_N + 2\rho I h_0 \ddot{\theta}_N + \frac{2\mu I}{h_0} (\theta_N - \theta_{N-1}) = 0 \qquad \text{when } i = N$$

The torsion pendulum consists of the rod together with a mass with moment of inertia I_0 attached to its last segment. This mass will undergo solid body rotation. As a result the presence of the mass alters the kinetic term but not the potential term. Assuming $I_0 \gg 2\rho I h_0$, the N'th equation becomes

$$2b_0 h_0 \dot{\theta}_N + I_0 \ddot{\theta}_N + \frac{2\mu I}{h_0} (\theta_N - \theta_{N-1}) = 0$$

In the limit $I_0 \gg 2\rho I h_0$, we can make the approximation $(\theta_N - \theta_{N-1})/h_0 \approx \theta_N / L$. Finally, we set $\Theta(t) = \theta_N(t)$ and obtain the equation of motion for a torsion pendulum

$$2b_0 h_0 \dot{\Theta} + I_0 \ddot{\Theta} + \frac{2\mu I}{L} \Theta = 0$$

The pendulum frequency is $\omega_{(p)}^2 = 2\mu I / L I_0$, and the amplitude decay is given by $\exp(-b_0 h_0 t / I_0)$. The damping parameter can be written in terms of the the number of oscillations taken for the amplitude to halve, $N_{1/2}$.

$$b = \frac{1}{2\rho I} b_0 = \frac{1}{2\rho I} \frac{I_0 \omega_{(p)} \log 2}{2\pi h_0 N_{1/2}}$$

In our experiments, we find $b = 1.3 \times \pi c_\theta / L$, where $c_\theta = \sqrt{\mu/\rho}$ is the speed of undamped twist waves. This approximately corresponds to critical damping.

3.3 Fracture model and minimal fragment size

Minimum fragment length

To stabilize the Kirchhoff model, we introduce a phenomenological minimum fragment length into our model. As shown by Audoly and Neukirch [6], when an initially uniformly curved elastic rod is released from one end, its local curvature increases at the free end. However, when a rod fractures at a point of maximum curvature, the Kirchhoff model possesses solutions in which the curvature near the fracture tip increases even further. Assuming a curvature based fracture criterion, this would trigger additional fractures arbitrarily close to the first fracture, which is not observed experimentally (Fig. 3-1B,D). In agreement with standard fragmentation theory [53, 139], our data show the existence of a finite minimum fragment length $\lambda > 0$ (Fig. 3-1D). This observation, along with the separation of bending wave and crack propagation timescales (Fig. 3-1A), confirms the applicability of the Kirchhoff theory (Fig. 3-1B,C).

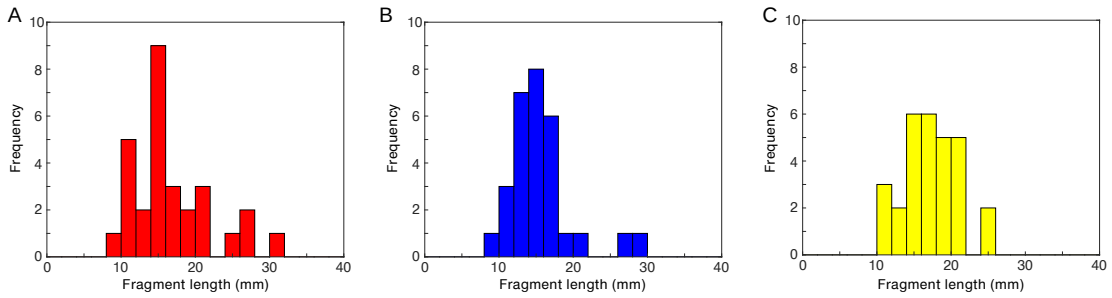

Figure 3-2: **The minimum fragment length is independent of radius.** (**A-C**) Lengths distributions of the first ejected fragment for samples of varying diameter. (**A**) Diameter $2h = 1.1\,\text{mm}$ ($n = 29$). (**B**) Diameter $2h = 1.4\,\text{mm}$ ($n = 29$). (**C**) Diameter $2h = 1.7\,\text{mm}$ ($n = 29$). In each case smallest observed length is approximately 10 mm. All data obtained for samples of length 24 cm at quench speeds $v > 200\,\text{mm/s}$.

Experimentally, the minimum fragment length, λ, depends on v, the quench speed.

We define λ statistically. Let $n_i(v)$ be the number of pieces observed in the ith trial at speed v. Let $\lambda_i(v)$ be the length of the smallest piece found in the ith trial at speed v. In the binary fracture case, $n_i(v) = 2$, we observe that $\lambda_i(v) \approx L/2$, however this is a bad estimate for the minimum fracture length, $\lambda(v)$. This can be explained as follows. By symmetry, the first fracture occurs at the midpoint of the rod. Then binary fracture will occur if $\lambda > L/4$. This motivates the definition of $\lambda_i^*(v)$

$$\lambda_i^*(v) = \begin{cases} L/4 & \text{if } n_i(v) = 2 \\ \lambda_i(v) & \text{otherwise.} \end{cases}$$

Finally, we define the minimum fragment length, $\lambda(v)$, by:

$$\lambda(v) = \frac{1}{n} \sum_{i=1}^{n} \lambda_i^*(v)$$

In other words, if non-binary fracture occurred at speed v, the minimum fragment length would be equal to the mean length of the smallest piece. Due to the infrequency of binary fracture for $v > 1\text{mm/s}$, setting $\lambda_i(v) = L/4$ when $n_i(v) = 4$ does not affect the scaling behavior of λ with v.

There are alternative ways of measuring the minimum fragment size, such as measuring the length of the first fragment to be ejected (Fig. 3-2). Data collected using this method suggest that there is an absolute minimum fragment length, 10 mm at high quench speeds, and that this length is independent of radius (Fig. 3-2). Intriguingly, this indicates that the phenomenological minimum fragment size is related to a material property of the rod.

Fracture criteria

To compare individual experiments with theoretical predictions, we solve the Kirchhoff equations (3.1) numerically with a discrete differential geometry algorithm [14, 13], adopting a stress-based fracture criterion. This involves the full stress tensor σ_{ij}, derived in equation (2.15). The effective stress at a point, $\sigma(s)$, is obtained by

integrating a scalar invariant of the full stress tensor, σ_{ij}, over a cross section of the rod

$$\begin{aligned}\sigma(s,t)^2 &= \frac{1}{2\pi h^2}\int dA\ \sigma_{ij}\sigma_{ij} \\ &= \frac{1}{4}E^2h^2\kappa(s,t)^2 + \frac{1}{2}\mu^2h^2\theta'(s,t)^2\end{aligned} \tag{3.2}$$

where κ is the geometrical curvature of the centerline and $\theta' = \kappa_3$ is the twist density. If the rod is in a steady state, the twist density is constant, $\theta' = Tw/L$, where Tw is the total applied twist. We posit that the rod fractures at a point s along the curve if the effective stress $\sigma(s)$ exceeds a critical value σ_c, which depends on the radius h and the material parameters of the rod. We further assume that no two fractures can occur within a minimal fragment length λ of each other. To describe the near-adiabatic twist experiments, we adopt the mean value $\lambda_0 \approx 30\,\mathrm{mm}$ measured at speed $\sim 3\,\mathrm{mm/s}$ and zero twist (Fig. 3-1D). For a uniform twist distribution, the critical stress imposes a critical yield curvature κ_c. This allows us to extract a dimensionless parameter describing the relative importance of twist and bending effects in fracture

$$\mathrm{Li} = \frac{\mu\, Tw}{E\kappa_c L} \tag{3.3}$$

We can now rewrite the above expression (3.2) for σ_c in a more intuitive form

$$\sigma_c^2 = E^2r^2\kappa_c^2\left(\frac{1}{4} + \frac{1}{2}\,\mathrm{Li}^2\right) \tag{3.4}$$

For comparison, by integrating the classical von Mises stress criterion over a cross section, we obtain a critical local stress ellipse given by

$$\left(\sigma_c^{\mathrm{VM}}\right)^2 = E^2r^2\kappa_c^2\left(\frac{1}{4} + \frac{3}{4}\,\mathrm{Li}^2\right) \tag{3.5}$$

Another common criterion comes from considering the maximum eigenvalue of the stress tensor, or maximum principal stress, on the boundary of the rod. This gives a critical stress parabola

$$\left(\sigma_c^{P}\right)^2 = E^2r^2\kappa_c^2\left(1 + \mathrm{Li}^2 + \sqrt{1 + 2\,\mathrm{Li}^2}\right) \tag{3.6}$$

All three curves are qualitatively consistent with our data, with equation (3.4) yielding the best quantitative agreement (Fig. 3-4F). For samples of different length and radius, and hence a different value σ_c, equation (3.4) is still found to agree well with the data. In the limit of zero twist, all three fracture criteria predict a critical curvature, which has been successfully used to rationalize aspects of twist-free elastic rod fracture [6]. While the origin of this critical curvature requires a deeper theory [140], the above fracture criterion (3.2) suffices for our purposes.

3.4 Twist controlled fracture

The first protocol we explore is the role of twist in bending-induced fracture. Twisting modes are known to cause many counter-intuitive phenomena in elastic rod morphology [40, 49, 107, 80], including Michell's instability [92] and supercoiling [18]. The motivation for combining twisting and bending to achieve controlled binary fracture is based on the idea that torsional modes can contribute to the first stress-induced fracture but may dissipate sufficiently fast to prevent subsequent fractures. To test this hypothesis, we built a custom device consisting of a linear stage with two freely pivoting manual rotary stages placed on both sides (Fig. 3-3A,B). Aluminum gripping elements were attached to each rotary stage to constrain samples close to the torsional and bending axes of rotation. As in Feynman's original experiment [131], we used commercially available spaghetti as test rods. To ensure reproducibility, in-

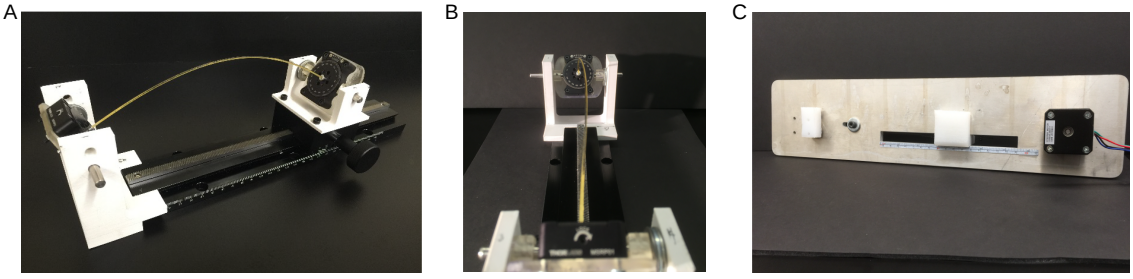

Figure 3-3: **Experimental apparatus.** (**A**) Twist controlled fracture device (**B**) Twist device generates twists high enough to produce visible out of plane buckling. (**C**) Speed controlled fracture device

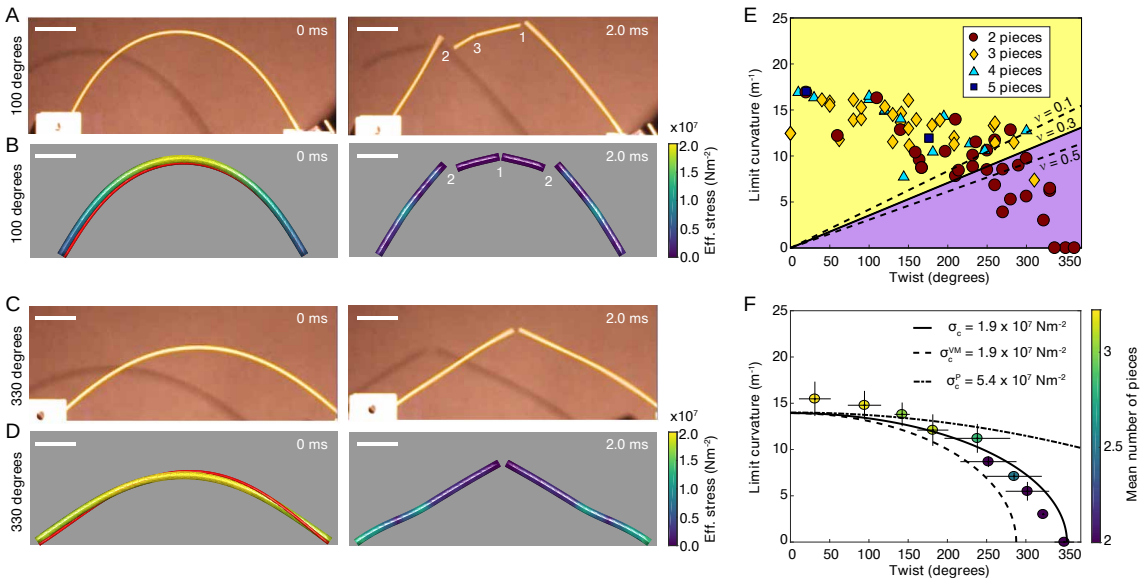

Figure 3-4: **Using twist to break Feynman's fragmentation bound.** (**A**) High-speed images from an experiment with subcritical twist angle showing fragmentation into more than two pieces, in agreement with Feynman's conjecture. Time $t = 0$ (left) is defined as the moment (last frame) before fracture (**B**) Simulations also predict fracture in more than two pieces for parameters corresponding to the experiment in (A). Due to perfectly symmetric initial conditions, our simulations generally produce even fragment numbers. Red line illustrates twist. (**C**) At supercritical twist angles, the maximum curvature before fracture is significantly lowered enabling twist-controlled binary fracture. (**D**) Simulations for the experimental parameters in (C) also confirm binary fracture. (**E**) Phase diagram showing that binary fracture dominates for twist angles larger than ~ 250 degrees ($n = 73$). The theoretically predicted region (purple) in which an ideal rod is expected to exhibit binary fracture depends only weakly on the Poisson's ratio ν and agrees well with the data. (**F**) Experimental data from (E), averaged over 10 sectors defined by the rays $(\mu^2 JL^{-1}\cos(j\pi/20), E^2 I \sin(j\pi/20))$ for $j = 0, 1 \ldots, 10$, follow the theoretically predicted critical ellipse (solid curve) from Eq. (3.4). The dashed curve shows the von Mises ellipse from Eq. (3.5), and the dash-dotted curve shows the parabola of constant maximum principal stress from Eq. (3.6). The data in Fig. 3-7 yield $\sigma_c = \sigma_c^{\mathrm{VM}} = \sigma_c^P/\sqrt{8} = 1.9 \times 10^7\,\mathrm{N/m^2}$ at zero twist. Error bars show standard deviations. The critical curvatures for simulations at different twist in (B) and (D) are chosen according to the critical stress ellipse in (F), and the minimum fragment length $\lambda = 30\,\mathrm{mm}$ estimated from the data in Fig. 3-1D. Diameter of rod in (B,D) enhanced for visualization. Scale bars in (A-D) 30 mm.

dividual rods were cut to the same fixed length $L = 24\,\mathrm{cm}$, and experiments were performed in a narrow temperature and humidity range. The rods' ends were coated with epoxy to increase the frictional contact with the gripping elements, enabling us to twist samples to the point of purely torsional failure, which occurred at $\sim$360

degrees for our elastic rods. In each individual twist experiment, a rod was loaded into the device, twisted to a predetermined angle, and then bent near-adiabatically (end-to-end speed $< 3\,\mathrm{mm/s}$) until fracture occurred. Select trials were recorded with a high-speed camera at 1972 fps.

As the first main result, our experiments demonstrate that supercritical twist angles give rise to binary fracture (Fig. 3-4). By contrast, for small twist angles, rods are found to fragment typically into three or more pieces (Fig. 3-4A), in agreement with Feynman's conjecture and supporting recent experimental and theoretical results [6] for the zero-twist case. For large twist angles, however, the maximum curvature before the first fracture is substantially lowered and binary fracture becomes favored (Fig. 3-4C). Although sample inhomogeneities lead to a distribution of fragment numbers at the same twist angles, the average number of fragments exhibits a robust trend towards binary fracture for twist angles larger than ~ 250 degrees (Fig. 3-4E,F). In particular, the experimental data follows a von Mises-type ellipsoidal curve when plotted in the plane spanned by the limit curvature and twist angle (Fig. 3-4E,F). We next rationalize these observations by performing mode analysis using the nonlinear elasticity model.

3.5 Decoupling of bend and twist modes

We consider the dynamics after the first fracture, starting from the fact that twist enables the rod to store its energy in more than one mode. We assume the first fracture occurs at $t = 0$ at the midpoint of the rod, when the curvature exceeds the critical value κ_c determined by Eq. (3.4). Our experiments and simulations show that at large twists, the rod breaks with low curvature (Fig. 3-4C-F). Focusing on this limit, we may assume that the rod is approximately planar, and that the bending is small. In this section, we show that under these assumptions, the twist and bending modes uncouple. The degrees of freedom in this reduced system are the twist $\theta(x,t)$, and the centerline $y(x,t)$, given in Cartesian coordinates. The dynamical equation for θ reduces to a damped wave equation $(\mu/\rho)\theta_{xx} = \theta_{tt} + 2b\theta_t$ for $x \in [0, L/2]$, and

bending is described by the Euler-Bernoulli beam equation $EIy_{xxxx} + \rho A y_{tt} = 0$, where subscripts are used to denote derivatives.

The starting point for this reduction is the Kirchhoff equations with twist damping (3.1). Appropriate boundary conditions follow from analyzing the experimental set up. In our twist experiments, the ends of the rod are hinged in such a way that $\mathbf{d}_3|_{0,L}$ can equilibrate as the ends are brought closer together (Fig. 3-3A,B). After fracture, however, the inertia of the rod is dominated by the inertia of the hinge, so we take boundary conditions which are clamped at $s = 0$ and free at $s = L/2$

$$\begin{aligned} \boldsymbol{x}(0,t) = \dot{\mathbf{d}}_{\mathbf{i}}|_{s=0} = 0 \\ \mathbf{M}(L/2,t) = \mathbf{F}(L/2,t) = 0 \end{aligned} \tag{3.7}$$

The centerline curve is parametrized using the global Cartesian basis:

$$\boldsymbol{x} = x\mathbf{e}_x + y(x,t)\mathbf{e}_y + z(x,t)\mathbf{e}_z = (x, y(x,t), z(x,t)) \tag{3.8}$$

We make the following assumptions

$$\begin{aligned} 1 \gg y_x, z_x \qquad & \text{(small deflections)} \\ y \gg z,\ y_x \gg z_x \qquad & \text{(approximate planarity)} \end{aligned}$$

We set $y_x = O(\alpha)$ and neglect terms of higher order. The planarity assumption indicates that terms of order z_x should be neglected, however we will retain time derivatives of z.

Properties of the rod can be calculated in the Cartesian basis (3.8). Since the parametrization of the curve has changed, the arc length is

$$\frac{ds}{dx} = \sqrt{1 + y_x^2 + z_x^2} = 1 + O(\alpha^2)$$

Therefore $d/ds = d/dx$ holds to $O(\alpha^2)$. In Cartesian coordinates, the Frenet frame

defined in equation (2.23) is given by

$$\mathbf{t} = \mathbf{d}_3 = (1,\ y_x,\ 0)\,, \qquad \kappa\mathbf{n} = \mathbf{t}' = (0,\ y_{xx},\ 0)\,, \qquad \kappa\mathbf{b} = \mathbf{t} \times \mathbf{t}' = (0,\ 0,\ y_{xx})$$

These equations are valid to leading order. From the definition of $\boldsymbol{\kappa}$ as $\mathbf{t}' = \boldsymbol{\kappa} \times \mathbf{t}$, we get $\boldsymbol{\kappa} = \kappa\mathbf{b} + \theta_s\mathbf{t}$

$$\boldsymbol{\kappa} = (\theta_x,\ \theta_x y_x,\ y_{xx})$$
$$\mathbf{M} = EI\kappa\mathbf{b} + \mu J\theta'\mathbf{t} = (2\mu I\theta_x,\ 2\mu I\theta_x y_x,\ EIy_{xx})$$

The expression for $\mathbf{M}$ follows from the identity $\kappa_1\mathbf{d}_1 + \kappa_2\mathbf{d}_2 = \mathbf{d}_3 \times \mathbf{d}_3' = \mathbf{t} \times \mathbf{t}'$. The twist compatibility equation, (2.29c), related ω_3 to θ

$$\omega_{3,s} = \theta_{st} - \kappa\dot{\mathbf{t}} \cdot \mathbf{b} = \theta_{st} + O(\alpha^2)$$

This follows from the identity $\dot{\boldsymbol{\kappa}} - \boldsymbol{\omega}' = \boldsymbol{\omega} \times \boldsymbol{\kappa}$ (see (2.21)). With a suitable choice of coordinates, this therefore gives $\omega_3 = \theta_t$, and the following expressions for $\boldsymbol{\omega}$ and $\mathbf{S}$

$$\boldsymbol{\omega} = (\theta_t,\ \theta_t y_x,\ y_{xt})\,, \qquad \mathbf{S} = 2\rho I\,(\theta_t,\ \theta_t y_x,\ y_{xt})$$

The twist damping term is

$$4b\rho I\omega_3\mathbf{t} = 4b\rho I(\theta_t, \theta_t y_x, 0)$$

The 6 Kirchhoff equations (3.1) can now be written down in the coordinates x, y, z, θ.

We write $\mathbf{F} = (F^x, F^y, F^z)$ in the Cartesian basis.

$$\begin{aligned}
F^x_x &= 0 \\
F^y_x &= \rho A y_{tt} \\
F^z_x &= \rho A z_{tt} \\
2\mu I \theta_{xx} + y_x F^z &= 2\rho I \theta_{tt} + 4b\rho I \theta_t \\
2\mu I \left(\theta_x y_x\right)_x - F^z &= 2\rho I \left(\theta_t y_x\right)_t + 4b\rho I \theta_t y_x \\
E I y_{xxx} + F^y - y_x F^x &= 2\rho I y_{xtt}
\end{aligned}$$

We assume $y_x F^y, y_x F^z$ are small compared to the other terms in the equations in which they appear, and so we drop these terms

$$\begin{aligned}
F^y_x = \rho A y_{tt}, \quad F^z_x &= \rho A z_{tt} \\
\mu \theta_{xx} &= \rho \theta_{tt} + 2b\rho\theta_t \\
2\mu I(\theta_x y_x)_{xx} - F^z &= 2\rho I \left(\theta_t y_x\right)_{xt} + 4b\rho I \theta_t y_x \\
E I y_{xxx} + F^y &= \rho I y_{xtt}
\end{aligned}$$

Consider the y equation

$$E I y_{xxx} + F^y = \rho I y_{xtt}$$

This equation can be simplified using a scaling argument. In the time independent case we have $E I y_{xxx} \sim F^y$, and in the time dependent case, $\rho A y_{tt} = F^y_x \sim F^y/L$ equation. Combining these scalings gives

$$\begin{aligned}
E I y_{xxx} &\sim F^y \\
\rho I y_{xtt} &\sim \frac{F^y I}{A L^2} \sim F^y \frac{h^2}{L^2}
\end{aligned}$$

Since $h/L \ll 1$, the $\rho I y_{xtt}$ term can be dropped. Eliminating F gives equations with

decoupled bending and twist

$$\mu\theta_{xx} = \rho\theta_{tt} + 2b\rho\theta_t \tag{3.9a}$$

$$2\mu I(\theta_x y_x)_{xx} - \rho A z_{tt} = 2\rho I\left(\theta_t y_x\right)_{xt} + 4b\rho I\theta_t y_x \tag{3.9b}$$

$$EIy_{xxxx} = -\rho A y_{tt} \tag{3.9c}$$

The bending dynamics reduce to the Euler-Bernoulli beam equation, which has been shown to describe certain aspects of elastic rod fracture [6]. From these equations, timescales for bending and twist can be obtained in the absence of damping

$$T_{\text{twist}} = L\sqrt{\frac{\rho}{\mu}}, \qquad T_{\text{bend}} = L^2\sqrt{\frac{\rho A}{EI}}$$

This shows that twist waves propagate on a faster timescale than bending waves

$$\frac{T_{\text{bend}}}{T_{\text{twist}}} = \frac{L}{h}\sqrt{\frac{2}{1+\nu}} \gg 1 \tag{3.10}$$

This is the fundamental scaling underlying our analysis of twist modes and bending modes.

3.6 Fracture dynamics

By analyzing the twist and bending equations separately, we show that twist does not play a role in the secondary fracture events. This involves finding the times T_θ^0, T_b^0, taken for bending and twist waves respectively to travel distance λ_0, where λ_0 is the minimum fragment length. In particular, we show that $T_b^0 > 4T_\theta^0$. In our twist experiments, where the ends of the rod are brought together slowly, this distance is measured to be $\lambda_0 \approx 30\,\text{mm}$. In addition, we show that the time taken for twist waves to dissipate, T_θ^{diss}, is approximately equal to $2T_b^0$.

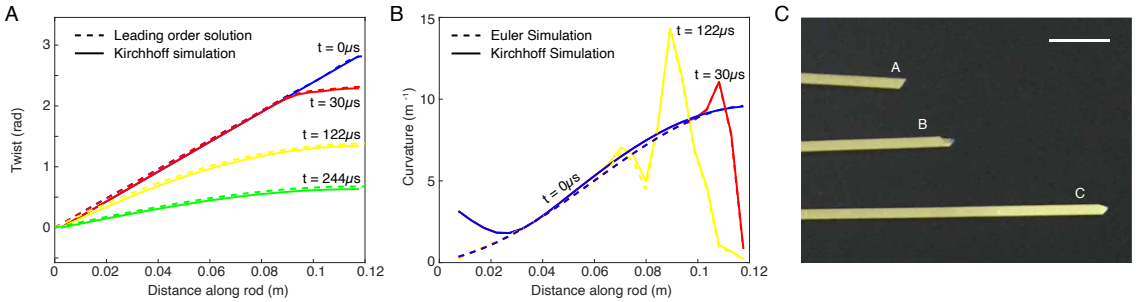

Figure 3-5: **Twist acts on faster timescales than bending.** (**A**,**B**) Evolution of twist and curvature after fracture of rod. (**A**) Twist can be neglected after time $t = L\sqrt{\rho/\mu} \approx 244\,\mu$s. (**B**) The curvature near the free end increases after fracture, while the curvature profile away from the free end changes slowly. Euler and Kirchhoff simulations coincide near the free end; discrepancies at high twist are due to out of plane buckling near $s = 0$. (**C**) Twist induced cracks (B,C) and curvature induced cracks (A) are shaped differently. Scale bar 1 cm.

Twist waves

Twist satisfies the damped wave equation

$$c_\theta^2 \theta_{xx} = \theta_{tt} + 2b\theta_t \tag{3.11}$$

where $c_\theta^2 = \mu/\rho$. The fracture problem has initial conditions

$$\theta(x,0) = \frac{Tw}{L}x, \qquad \theta_t(x,0) \quad = 0 \tag{3.12}$$

and boundary conditions (3.7)

$$\theta(0,t) = 0, \qquad \theta_x(L/2,t) \quad = 0 \tag{3.13}$$

It is important to note that the boundary conditions are incompatible with the initial conditions. The same issue arises in the y equation describing curvature. In both cases, this inconsistency may be attributed to a boundary layer [6] very close to the newly fractured free end at $x = L/2$. Nevertheless, we can find an approximate solution by solving the Sturm-Liouville problem given by the BCs and then expanding the initial condition in the Sturm-Liouville eigenbasis. Such a solution will satisfy all

the above conditions except very close to the endpoint $x = L/2$. Separating variables with $\theta = X(x)T(t)$ we obtain

$$X_{xx} + k_n^2 X = 0$$
$$T_{tt} + 2bT_t + c_\theta^2 k_n^2 T = 0$$

with the following initial conditions and boundary conditions: $X(0) = X_x(L/2) = 0$, $T(0) = 1$, $T_t(0) = 0$. Setting $k_n' = \sqrt{|b^2 - c_\theta^2 k_n^2|}$, we obtain the full solution

$$\begin{aligned}
\theta(x,t) &= \sum_n A_n \sin(k_n x) f_n(t) \\
k_n &= \frac{(2n+1)\pi}{L} \\
A_n &= \frac{4}{L}\int_0^{L/2} x \sin(k_n x)dx \\
f_n(t) &= e^{-bt}\left(\sum_{c_\theta k_n < b}\left(\frac{b}{k_n'}\sinh k_n' t + \cosh k_n' t\right) + \sum_{b < c_\theta k_n}\left(\frac{b}{k_n'}\sin k_n' t + \cos k_n' t\right)\right)
\end{aligned}$$

Only a few modes are necessary to obtain a good approximation, so issues of convergence related to the boundary layer can be ignored. At $b = 0$ (no damping), we find $f_n(t) = \cos(k_n c_\theta t)$, so the rod has smallest frequency $\omega_0 = c_\theta k_0 = \pi c_\theta / L$. From $t = 0$ to $L/2c_\theta$ the undamped solution corresponds to a zero stress region with $\theta_x = 0$ growing at speed c_θ until $t = L/2c_\theta$, when $\theta = \theta_x = 0$ everywhere. In the presence of damping, the zero twist stress region only grows at speed c_θ at early times. In particular, the time taken for the zero twist stress front to travel distance λ_0, the minimum fragment length, is

$$T_\theta^0 = \frac{\lambda_0}{c_\theta} \tag{3.14}$$

Over longer lengthscales $\ell > \lambda_0$, the damping term becomes important. The scalings of the terms in the damped wave equation (3.11) show that the zero twist front travels

distance ℓ in time $T_\theta^\ell = b\ell^2/c_\theta^2$. Our measured value of b is $b \approx \pi c_\theta/L$, which gives

$$T_\theta^\ell = \frac{\pi \ell^2}{c_\theta L} \tag{3.15}$$

In addition, since $b \approx \omega_0$, the lowest mode is approximately critically damped. We therefore obtain a solution where twist stress may be neglected after a time $t = L/c$ instead of $t = L/2c$ (Fig. 3-5A). This gives the dissipation timescale for twist

$$T_\theta^{\text{diss}} = \frac{L}{c_\theta} \tag{3.16}$$

This is still fast when compared to bending waves (Fig. 3-5B) as can be seen from the fracture interfaces (Fig. 3-5C). The geometry of these fracture interfaces supports our picture of fragmentation in which twist causes the first fracture, and bending waves cause subsequent fractures.

Bending waves

We analyse the speed of bending modes in a similar way. The equation for bending is given by

$$EIy_{xxxx} = -\rho A y_{tt} \tag{3.17}$$

subject to pre-fracture initial conditions

$$y(x,0) = y^0(x), \qquad y_t(x,0) = 0 \tag{3.18}$$

and boundary conditions which are clamped at $x = 0$ and free at $x = L/2$:

$$y(0,t) = y_{xt}(0,t) = 0, \qquad y_{xx}(L/2,t) = y_{xxx}(L/2,t) = 0 \tag{3.19}$$

The initial shape $y^0(x)$, is set by solving the time independent Kirchhoff equations at a given twist, so y^0 depends both on the twist of the sample and the critical curvature

at the point of fracture. At non-zero twist, the time independent Kirchhoff equations yield a non-planar solution with twist dependent shape. The curve y^0 is found by neglecting the out of plane components of this shape. This procedure yields accurate results on the time scales relevant to fracture (Fig. 3-5B). As with twist, the initial condition is incompatible with the free end boundary conditions. However the high energy curvature waves triggered as a result travel slowly compared to the twist waves (Fig. 3-5A,B).

Our data show that fractures are caused by the pulse of maximum bending stress (solid line in Fig. 3-1D). The path of this pulse can be found analytically in the linear regime [6]. The explicit solution for the curvature in this regime is [6]

$$\kappa(x,t) = y''(x,t) = 2\kappa_0 S\left(\frac{x}{\sqrt{\pi r c_s t}}\right) \tag{3.20}$$

where $S(x)$ is the Fresnel sine integral, $c_s = \sqrt{E/\rho}$ is the speed of sound in the rod, and $y''(x,0) \equiv \kappa_0$ to linear order. The function $S(w)$ has a maximum at $w = \sqrt{2}$. Substituting this into the above curvature solution gives the time at which the point of maximum curvature reaches a position ℓ

$$t = \frac{\ell^2}{2\pi h c_s} = \frac{\ell^2}{2\pi h}\sqrt{\frac{\rho}{E}} \tag{3.21}$$

This result may also be derived by considering the bending wavepackets. The speed of a bending wavepacket peaked at wavenumber k is given by $c_b = 2k\sqrt{EI/\rho A}$. If we take $k = 2\pi/\ell$, then the time taken for the bending wavepacket to travel distance ℓ is $T_b^\ell \approx \ell\left[(4\pi/\ell)\sqrt{EI/\rho A}\right]^{-1} = (\ell^2/2\pi h)\sqrt{\rho/E}$. We can use these results to compare the timescales on which twist and bending operate:

$$T_b^0 = \frac{\lambda_0}{2\pi h}\left[\frac{1}{2(1+\nu)}\right]^{1/2} T_\theta^0 \tag{3.22a}$$

and

$$T_b^\ell = \frac{L}{2\pi^2 h}\left[\frac{1}{2(1+\nu)}\right]^{1/2} T_\theta^\ell \tag{3.22b}$$

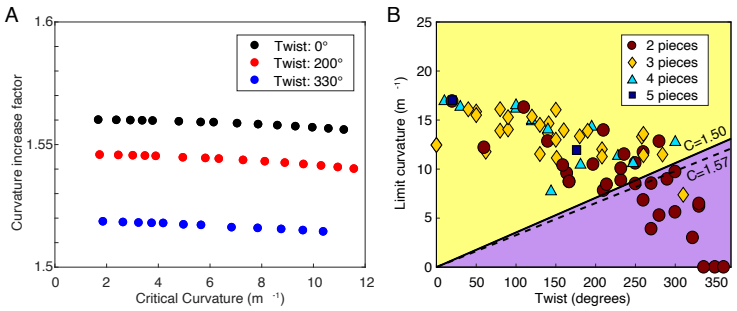

Figure 3-6: **Binary fracture depends weakly on the curvature increase factor** (**A**) The curvature increase factor, C, lies in a narrow range for different pre-fracture twists and critical curvatures. $C = 1.5$ to 1dp for twist angles relevant to binary fracture in our samples, and it is calculated by simulating the full Kirchhoff equations. (**B**) Critical lines exhibit weak dependence on C. All simulations carried out using the experimental material parameters, $E = 3.8\,\mathrm{GPa}$, $\nu = 0.3$, $\rho = 1.5\,\mathrm{g/cm}^3$, $L = 24\,\mathrm{cm}$, $2h = 1.4\,\mathrm{mm}$.

Using the measured value $\lambda_0 \approx 30\,\mathrm{mm}$, we find $T_b^0 > 4T_\theta^0$ and $T_b^\ell > 5T_\theta^\ell$, indicating that twist dissipates before bending waves can trigger another fracture. In addition, we find that $T_\theta^{\mathrm{diss}} \approx 2T_b^0$, which further suggests that twist plays no role in future fracture events. The above difference in propagation times is a robust result. For example, Timoshenko theory predicts even slower bending waves than Euler-Bernoulli theory [54], although both beam models agree very closely in our parameter regime.

Binary fracture criterion

To complete the binary fracture argument, we observe that all the fractures occur before reflection of the bending waves at $s = 0$ becomes important. Another fracture will then be triggered if and only if $\sigma(s,t) > \sigma_c$ for any s satisfying the minimum fragment length criterion and $t \in [0, t_0]$, where t_0 is the time for the high energy bending waves to reach $s = 0$. Since twist dissipates before the bending waves become relevant, we have $\max_{t\in[0,t_0]} \sigma^2 = E^2 I \max_{t\in[0,t_0]} \kappa^2$. Let C be such that $\max_{t\in[0,t_0]} \kappa = C\kappa_c$. Even though twist dissipates quickly, the initial twist still determines the shape of the rod at $t = 0$, so C is a function of $\kappa_c L, Tw$ and possibly other parameters. The linear solution (3.20), gives a value of $C = 2S(\sqrt{2}) \approx 1.43$. We calculate C numerically from the full Kirchhoff equations for our experimental parameters, and

find to one decimal place $C = 1.5$ for all relevant values of $\kappa_c L$ and Tw (Fig. 3-6A). Further precision is not required, since the critical region for binary fracture depends only weakly on C (Fig. 3-6B). The criterion that the rod only breaks into two pieces then takes the form $E^2 I C^2 \kappa_c^2 < \sigma_c^2$. Using (3.4) to eliminate σ_c, the criterion for binary fracture becomes:

$$\kappa_c < \frac{Tw}{\sqrt{2}L(1+\nu)\sqrt{C^2-1}}. \tag{3.23}$$

In terms of the dimensionless Li-number from Eq. (3.3), this condition is approximately $\mathrm{Li} > 1$. The right hand side of this inequality describes a weakly ν-dependent straight line in the curvature-twist plane (Fig. 3-4E). Ideal elastic rods that undergo their first fracture at values κ_c and Tw satisfying (3.23) lie below this line (purple region in Fig. 3-4E) and are expected to break into exactly two pieces. This prediction agrees well with the mean number of fragments measured in our experiments (Fig. 3-4F). Additional data for samples of a different length and radius also show good agreement with Eq. (3.23). The raw data show that binary fracture events can occur with low probability outside the critical region (Fig. 3-4E), which could be caused by sample defects and inhomogeneities. The distinct transition from binary to non-binary fracture in the averaged data (Fig. 3-4F) indicates however that defects do not dominate the fracture statistics. Our results for the low-twist regime are consistent with those of Audoly and Neukirch [6] who reported non-binary fracture at zero twist. By contrast, binary fracture becomes almost certain in the high-twist regime.

3.7 Quench controlled fracture

Twist fracture experiments are carried out for a fixed speed $v = 3\,\mathrm{mm/s}$ in the near-adiabatic regime. To systematically explore how quenching affects elastic rod fracture, we built a second fracture device coupling a DC stepper motor to a linear stage (Fig. 3-3C). By adjusting the motor velocity, we can vary the quench speed v, defined as absolute relative velocity of the ends, by more than two orders of magnitude

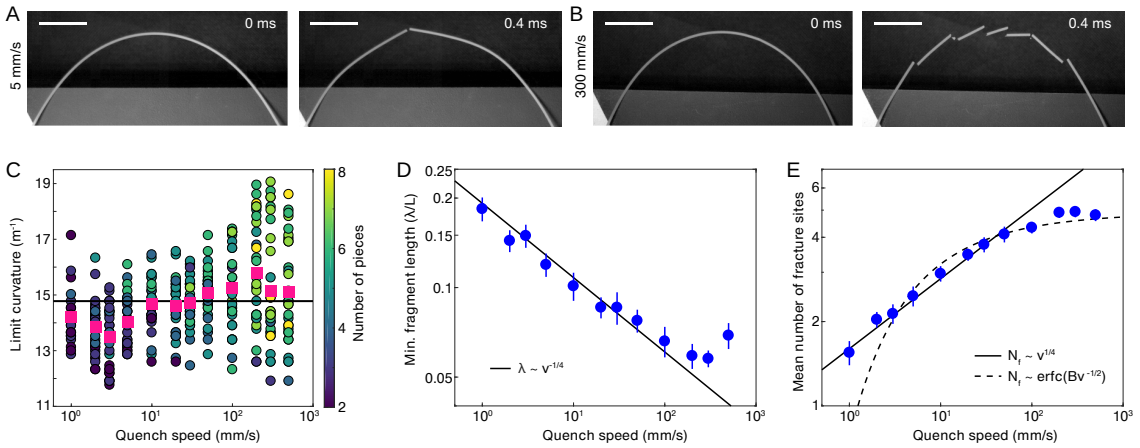

Figure 3-7: **Dynamically quenched fracture in brittle elastic rods.** (**A**) Experiment at low quench speed v showing binary fracture. (**B**) Experiment at high quench speed v showing fracture into multiple fragments, even though the limit curvature before the first fracture is similar to that in (A). (**C**) Distributions of the limit curvature (mean values highlighted in pink) are not significantly affected by the quench speed v, but the mean number fragments increases with v ($n = 350$). (**D**) The mean length of the smallest fragments follows the theoretically predicted power law scaling. (**E**) At low speed, the number of fracture sites approaches an asymptotic power law (solid line) as expected from (D). At high speeds, saturation occurs in agreement with stochastic fracture theory (dashed line). At the lowest quench speed ($v = 1\,\mathrm{mm/s}$) the rod breaks into fewer than three pieces on average. Scale bars in (A,B) 30 mm. Error bars in (D,E) show standard error.

(Fig. 3-7). Our nonadiabatic quench protocol allows the rod to bend before fracturing, in contrast to ultra-fast diabatic protocols [45] that cause fracture by exciting buckling modes in the unbent state. Previous studies have shown that the fractal nature of fragmentation [137] and the effects of disorder [31] can give rise to universal power laws. Here, we will see that nonadiabatic quenching leads to a new class of asymptotic power law relations that involve the quench parameter v and can be rationalized through scaling arguments.

To investigate how quenched bending dynamics affects fracture, we performed 350 fracture experiments distributed over 12 different quench speeds v ranging from 1 mm/s to 500 mm/s, with rods of length $L = 24\,\mathrm{cm}$, as in the twist experiments. Experiments were conducted in two batches at different environmental conditions, yielding consistent data. Select trials were recorded at 75000 fps (Fig. 3-7A,B). Generally, our experiments show that an increase in the quench speed v has only a weak

effect on the curvature prior to fracture (Fig. 3-7C), in stark contrast to the effects of twist discussed above. Changing v does however affect strongly both the minimal size of the fragments (Fig. 3-7D) and the number of fragments (Fig. 3-7E,F).

To understand why quench speed (at zero twist) only weakly affects the limit curvature, note that the critical curvature of the samples at first fracture is of the order of $10\,\mathrm{m}^{-1}$ across all experiments (Fig. 3-7C). This means that the potential energy density at the first fracture is $E_P \approx EI\kappa^2 \approx 10^{-1}\,\mathrm{J/m}$. For comparison, for a hypothetical quench speed of $v = 1\,\mathrm{m/s}$, considerably higher than realized in our experiments, the kinetic energy density is $E_K \approx \rho A v^2/2 \approx 10^{-3}\,\mathrm{J/m} \ll E_P$.

Yet, higher quench speeds v lead to higher fragment numbers (Fig. 3-7A,B), reflecting the fact that the minimum fragment length λ decays with v (Fig. 3-7D). We can rationalize this using dimensional analysis. The dynamics of the rod are overdamped, so during a quench the force on any element scales as $F \sim v$. In one dimension, force has units of energy density so we will balance F against the other fundamental energy density of the system, the potential energy density. The energy density of the k'th bending mode scales as $E_k \sim k^4$, yielding $k \sim v^{1/4}$ and hence $\lambda \sim v^{-1/4}$ in agreement with the data (Fig. 3-7D).

The same scaling is implied by the following more detailed argument. Suppose the rod is initially approximately flat, lying on the x-axis at time $t = 0$, with endpoints at $(x, y) = (\pm L/2, 0)$. Consider the shape of the rod as it is quenched at speed v. The overdamped, or quasistatic assumption tells us that at time t, we only need to solve the static problem of a rod whose endpoints are at $(x, y) = (\pm(L/2 - vt), 0)$. The static Euler-Bernoulli equation, $y_{xxxx} = 0$, and the symmetry of our problem yield a solution $y(x, t) = A_0 - A_1 x^2$ subject to $y(\pm(L/2 - vt)) = 0$. Note that $2A_1 = \kappa_0$, the maximum curvature in the rod. We will relate κ_0 to v, t, L via the inextensibility constraint

$$\frac{L}{2} = \int_0^{\frac{L}{2}-vt} dx \sqrt{1 + \kappa_0^2 x^2}$$

Assume $\kappa_0 x < 1$, so $\sqrt{1 + \kappa_0^2 x^2} = 1 + \kappa_0^2 x^2/2 + O(\kappa_0^4 x^4)$. Then the above integral can

be calculated

$$\begin{aligned}\frac{L}{2} &= \int_0^{\frac{L}{2}-vt} dx \left(1 + \frac{1}{2}\kappa_0^2 x^2\right) + O(\kappa_0^4 x^4) \\ &= \frac{L}{2} - vt + \frac{1}{6}\kappa_0^2 \left(\frac{L}{2} - vt\right)^3 + O(\kappa_0^4 x^4)\end{aligned}$$

Now take $\frac{L}{2vt} > 1$

$$\begin{aligned}vt &= \frac{1}{48}\kappa_0^2 L^3 \left(1 - \frac{2vt}{L}\right)^3 + O(\kappa_0^4 x^4) \\ \kappa_0 &= \sqrt{\frac{48vt}{L^3}} + O\left(\frac{vt}{L}\right) + O(\kappa_0^4 x^4)\end{aligned}$$

Thus we arrive at the scaling

$$\epsilon_0 \sim h\kappa_0 \sim \sqrt{\frac{vtr^2}{L^3}}$$

However, as the rod is pushed, low energy bending waves must necessarily equilibrate its shape. We balance the dominant frequency ω of these waves with the strain rate above, $\dot{\epsilon}_{\max}^2 \sim (vh^2/tL^3) \sim \omega^2$. Finally, the dispersion relation for bending waves, $\omega \sim c_s h k^2$ yields $v/tL^3 \sim c_s^2 k^4$. This scaling then gives the dominant wavenumber k in the equilibration wave packet for a given quench speed v. Our data indicate that λ is independent of the rod radius h, which suggests a role for acoustic waves triggered by the equilibration wave packet. These acoustic waves will weaken the rod at their anti-nodal high strain sites. At early times, the dominant acoustic wavenumber can be matched with the dominant equilibration wavenumber, yielding a minimum fragment length $\lambda \sim k^{-1} \sim v^{-1/4}$.

In one-dimensional fragmentation the number of fracture sites N_f and the minimal fragment length λ are predicted [53] to scale as $\lambda \sim N_f^{-1}$. N_f is related to the number of fragments N by $N = N_f + 1$. Combining these scaling results, we obtain the prediction $N_f \sim v^{1/4}$ at small v, in agreement with our data (Fig. 3-7F). In particular, this also explains why rods can undergo binary fracture when the quench

velocity is very small (Fig. 3-7A). At sufficiently high quench speeds, the number of fracture sites, and hence the number of fragments, saturates (Fig. 3-7E). Stochastic fracture theory provides a possible explanation for this effect. The picture of quenched fragmentation which emerges is as follows: The quench speed releases bending and acoustic waves of particular wavelengths which weaken the rod in certain patterns. At low speeds the number of fracture sites simply increases as a power law, whereas at high speeds this growth is limited by the rate of subcritical crack growth.

3.8 Stochastic fracture theory

To understand the saturation of N_f, we return to the first timescale involved in fragmentation, the time taken for the crack to grow to the critical Griffith length (Fig. 3-1A). We refer to this timescale as the break-up time. Consider a crack at a single site along the rod. We assume the crack depth $\boldsymbol{X}$ is a random variable which increases diffusively, with strain-dependent diffusion constant [140], D. Under this assumption, the time $\boldsymbol{T}$ taken for the crack to reach the critical depth x_* is Levy distributed and can be calculated using the reflection principle

$$\begin{aligned}\mathbb{P}\left(\boldsymbol{T} < t\right) &= 2\mathbb{P}(\boldsymbol{X}(t) > x_*) \\ &= \frac{2}{\sqrt{4\pi D t}} \int_{x_* - x_0}^{\infty} dx e^{-\frac{(x_* - x_0)^2}{4Dt}}\end{aligned}$$

with probability density function

$$f_{\boldsymbol{T}}(t) \propto (x_* - x_0) t^{-3/2} e^{(x_* - x_0)^2/4Dt}$$

where x_0 is the initial penetration depth of the crack. The mean of this distribution diverges, but a typical breakup time t_* can be extracted by maximizing $f_{\boldsymbol{T}}(t)$. This yields $t_* \sim (x_* - x_0)^2 D^{-1}$. To apply this to fragmentation, consider the number of sites at which breakup can occur in time $T_b^{L/2}$, the time taken for a bending wave to

travel half the length of the rod. Assuming the sites are independent, this gives

$$N_f \propto \mathbb{P}(\boldsymbol{T} < T_b^{L/2}) \propto \mathrm{erfc}(Bt_*^{1/2})$$

where B is a constant to carry dimensions, and erfc is the complementary error function. Finally, we note the strain dependence of t_*. From above we know how strain changes as the rod is quenched, $\epsilon \sim \sqrt{vth^2/L^3}$. The characteristic timescale for strain variation is thus $\tau_1 \sim L^3/vh^2$. Balancing the typical break-up time with the strain timescale of the rod yields $t_* \sim 1/v$, and thus $N_f \propto \mathrm{erfc}(Bv^{-1/2})$, where B carries dimensions as before. At large quench speeds, this agrees with the data for $B^2 \approx 1\,\mathrm{mm/s}$ (Fig. 3-7E).

3.9 Robustness under parameter variations

The key results for twist and quench controlled fracture are reproducible in different environmental conditions (humidity and temperature) and for samples of different dimensions. We are able to experimentally verify the existence of a critical binary fracture region for samples of different diameters and lengths (Fig. 3-8A). Further, the fracture criterion developed and verified for samples with $2h = 1.4\,\mathrm{mm}$, $L = 24\,\mathrm{cm}$, shows good agreement with the fracture data of samples with $2h = 1.7\,\mathrm{mm}$ and $L = 20\,\mathrm{cm}$ (Fig. 3-8B). In the case of quenched fracture, we note that experiments at higher humidity appear to show a weak dependence between limit curvature and quench speed. We understand this as a consequence of the ductility of spaghetti. In warmer, more humid conditions, spaghetti is expected to soften slightly.

3.10 Numerical methods

Numerical results in Fig. 3-4B,D were obtained by simulating the Kirchhoff equations (3.1) using the discrete differential geometry algorithm introduced in Refs.[14, 13] and discussed in Chapter 2. Each rod was discretized into 50 elements (Fig. 3-9) and one time-step of simulation time corresponded to 1μs of real time. Time-stepping

was performed with a Verlet scheme. Fracture was simulated by disconnecting the rod in 1 time-step wherever the fracture criterion was satisfied. The radius of the rod has been enhanced in simulation images (Fig. 3-4B,D) for visualization purposes. The curvatures in Fig. 3-4E,F and Fig. 3-7C were obtained numerically from the observed end-to-end distance by initializing a rod with the appropriate boundary conditions and twist, and allowing it to relax to its lowest energy state via gradient descent. In the case of zero twist, there is a closed form relationship between end-to-end distance and maximum curvature, which we used to validate the code.

3.11 Experimental methods

The experiments were conducted with Ronald Heisser, who built the apparatus. All experiments used Barilla no. 1, 3 or 5 raw spaghetti of length $L = 24\,\text{cm}$ or $20\,\text{cm}$. High air humidity and large temperature fluctuations can affect bending and fracture behavior of the samples. Experiments were conducted in two batches, each with consistent environmental conditions. Humidity was in the range 21%-34% in the first batch, 41%-51% in the second batch. Temperature during both sets of experiments was kept in the range $21 - 26\,\text{C}$. The rod diameter was measured using calipers for 5 samples. The density was obtained by weighing 10 samples cut to 24 cm. Treating the samples as cylinders of radius h we obtained $\rho = 1.5 \pm 0.1\,\text{g/cm}^3$. The Young's modulus, E, was measured by applying a slowly increasing longitudinal compression force to samples positioned upright upon a scale. The sample length ℓ and the mass m shown on the scales at the point of buckling were recorded. We repeated this for 20 samples of varying lengths, and in each case calculated E from the Euler buckling criteria, $mg = \pi^2 EI/\ell^2$, to find $E = 3.8 \pm 0.3\,\text{GPa}$. The shear modulus was measured by attaching a mass of known moment of inertia, I_0, to samples of varying length to create a torsion pendulum. The angular frequency, $\omega^2 = \mu J/I_0 L$, was obtained for 5 samples, by filming the pendulum with an Edgertronic SC2 at 1972 fps. The Poisson's ratio, $\nu = (E/2\mu) - 1$ was calculated from the mean values of E and μ. Using standard error of these mean values to quantify uncertainty gives $\nu = 0.3 \pm 0.1$. The

twist damping parameter was obtained from the decay rate of the torsion pendulum.

Twist experiments

Twist experiments were performed using a custom-built device comprising of a manual linear stage with two freely pivoting manual rotary stages placed on both sides. Aluminum gripping elements were attached to each rotary stage to constrain samples close to the torsional and bending axes of rotation. In the first batch, we used Barilla no. 3 cut to 24cm and completed 73 trials at various twist angles up to 360 degrees, corresponding to the approximate pure torsion yield stress of the samples. In the second batch, we used Barilla no. 5 cut to 20cm for 33 trials. To ensure reproducible twisting of the samples within the desired range, the ends of each rod were coated with Devcon® 5 minute epoxy gel. The epoxy increased friction between each sample and the gripping element in our testing device, enabling us to twist samples to the point of torsional failure. Each sample was loaded into the device, twisted to the chosen angle, and bent until fracture occurred. Ends were moved together slowly ($< 3\,\mathrm{mm/s}$) to ensure a quasi-static regime. The end-to-end distance at the onset of fracture was recorded for each trial. Select trials were recorded with an Edgertronic SC2 at 1972 fps.

Quench experiments

Kinetic quench experiments consisted of 20 trials each for 12 speeds ranging from $1\,\mathrm{mm/s}$ to $500\,\mathrm{mm/s}$ in the first batch, and 10 trials each for 11 speeds from $2\,\mathrm{mm/s}$ to $500\,\mathrm{mm/s}$ in the second. Data for quench trials are combined in Fig. 3-7C. Trials were conducted using a custom single-axis linear stage controlled by a NEMA 17 Bipolar DC Stepper Motor. The device moved the ends of each sample towards each other at a fixed speed v while allowing them to pivot freely as bending occurred. The end-to-end distance at the onset of fracture was obtained by recording each trial with a high speed camera and examining the playback. Occasionally, small flakes would be ejected from the sample at high quench speeds (Fig. 3-7B). Fragments

were only counted if they had length longer than the rod radius. The cameras used were the Photron FASTCAM Mini AX200 at 9000 fps and the Phantom v611 at 75000 fps. Select trials were stored permanently. Crack propagation was filmed using the Phantom v611 at 1000000 fps, using a thicker spaghetti (diameter 1.7 mm) for improved visualization.

3.12 Conclusions

We have demonstrated two distinct protocols for achieving controlled binary fracture in brittle elastic rods. By generalizing classical fracture arguments [6] to account for twisting and quenching, we were able to rationalize the experimentally observed fragmentation patterns (Fig. 3-1). Due to their generic nature, the above theoretical considerations can be expected to apply to torsional and kinetic fracture processes in a wide range of engineered [60] and natural [132, 104] one-dimensional structures. In addition, our experimental results suggest several directions for future research. New theory beyond the Kirchhoff model is needed to clarify conclusively the microscopic origin of the minimum fragment length. Moreover, a detailed experimental analysis of the crack propagation dynamics will require going beyond MHz time-resolution. From a practical perspective, it will be interesting to explore whether, and how, twist can be utilized to control the fracture behavior of two- and three-dimensional materials.

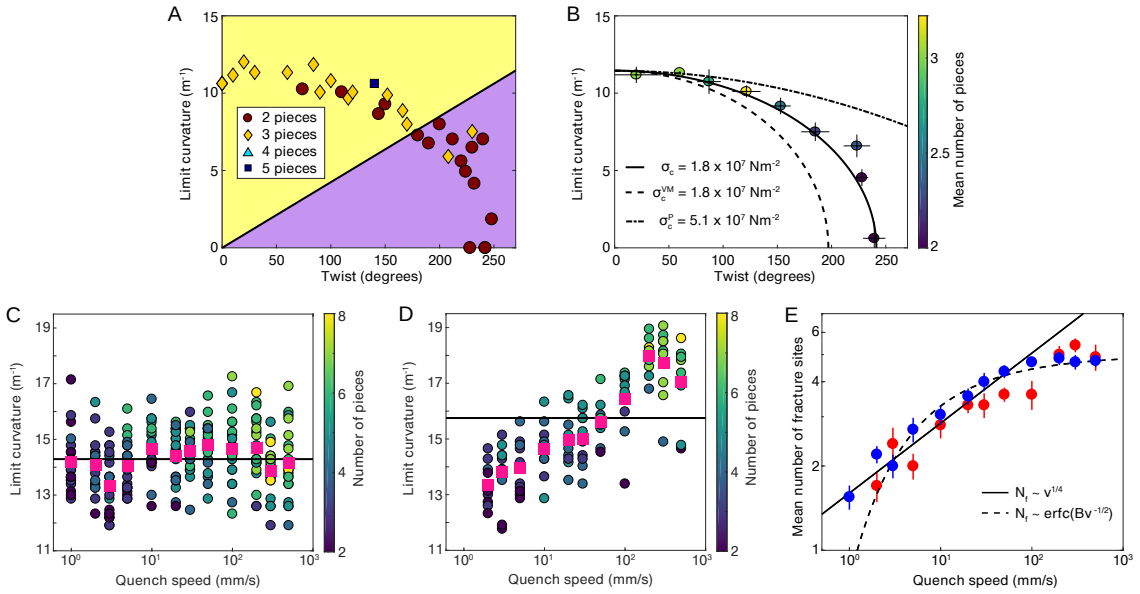

Figure 3-8: **Twist and quench controlled fracture results are robust under parameter variations.** (**A**) Agreement between theoretical prediction of a critical binary fracture region (purple) and experiments conducted with samples of length $L = 20\,\mathrm{cm}$ and diameter $2h = 1.7\,\mathrm{mm}$. These results complement the agreement found for samples with length $L = 24\,\mathrm{cm}$ and diameter $2h = 1.4\,\mathrm{mm}$, shown in Fig. 3-4. (**B**) Experimental data from (A), averaged over 10 sectors defined by the rays $(\mu^2 JL^{-1}\cos(n\pi/20), E^2 I \sin(n\pi/20))$ for $n = 0, 1 \ldots 10$, follow the theoretically predicted critical ellipse (solid curve). The dashed curve shows the von Mises ellipse, and the dash-dotted curve shows the parabola of constant maximum principal stress, with critical stress values $\sigma_c = \sigma_c^{\mathrm{VM}} = \sigma_c^P/\sqrt{8} = 1.8 \times 10^7\,\mathrm{N/m^2}$ at zero twist. Error bars show standard deviations. (**C**) At low humidity (21% - 34%, first batch of experiments), distributions of the limit curvature (mean values highlighted in pink) are not significantly affected by the quench speed v, but the mean number fragments increases with v. Solid line shows total mean limit curvature. (**D**) At high humidity (41% - 51%, second batch of experiments), distributions of the limit curvature (mean values highlighted in pink) show a weak dependence on the quench speed v. Solid line shows total mean limit curvature. (**E**) Relationship between number of fractures and quench speed is robust across the first (blue) and second (red) batches.

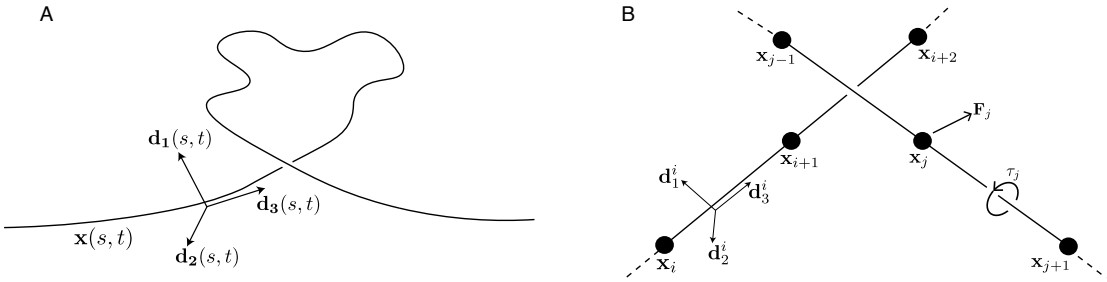

Figure 3-9: **Discretization of Kirchhoff rods.** (**A**) Dynamical variables of the Kirchhoff rod. (**B**) Discretization of the Kirchhoff rod.

Chapter 4

Knots and tangles

Knotted structures play a fundamental role in the dynamics of biological and physical systems, from DNA strands and polymers to liquid crystals and turbulent plasmas. However, knots are also crucial in the more quotidian contexts of climbing, weaving, sailing and surgery. In this chapter, we investigate the dynamics of knots as they appear in these settings. Despite having been empirically studied for centuries, the subtle interplay between topology and mechanics in such knotted elastic materials remains poorly understood. Here we analyze knots by combining theory and simulations with experiments using optomechanical color changing fibers, designed by Professor Mathias Kolle's lab. Exploiting a previously unrecognized analogy with long-range ferromagnetic spin systems, we identify simple counting rules to predict the relative mechanical stability of knots and tangles. In particular, we show that for knots of a certain kind, the writhe of the knot is related to its self-torque, thus playing a key role in knot stability. The topological counting rules we find are in agreement with numerical simulations and experimental measurements for commonly used climbing and sailing knots. The underlying topological principles provide a conceptual foundation for understanding the roles of twist and writhe in untangling processes, and are expected to find broad applications in the description and control of systems with complex entanglements.

4.1 History

Knots are among the oldest, most enduring human technologies, as valuable to ancient builders [138] and mariners [3] as to modern engineers [121] and surgeons [136]. Thought to predate the wheel [138], knotted structures owe their remarkable longevity and widespread usage to an inherent mechanical robustness that arises from the subtle interplay of topology, elasticity and friction. Over the course of many centuries, sailors, weavers, climbers and surgeons have acquired a wealth of knowledge about the benefits and drawbacks of various types of knots [3, 138, 37]. Yet, much of this empirical wisdom is still awaiting proper theoretical explanation. While experience has taught us that certain knots are more stable than others, we are still largely unable to predict the mechanical behavior of knots and tangles from basic topological observables [1], such as the number and relative ordering of crossings. Although recent experimental and theoretical research has revealed important insights into the competition between force transmission and friction in special classes of knots [5, 63], hitches [12] and fabrics [143, 89], there currently exists no comprehensive mathematical theory [19] linking the topological and mechanical properties of knotted elastic structures.

Physical knots and their topology first assumed a central role in science with the introduction of Kelvin's vortex-atom model in the 1860s [134]. Ever since, the fundamental importance of entangled structures has become firmly established in a diverse range of disciplines and contexts [19]. In physics, for example, interactions between knotted defect lines are essential to understanding and controlling the dynamics and the mixing in classical and complex fluids [95, 97, 76, 124, 82], including liquid crystals [135], plasmas [133] and quantum fluids [77]. Whereas the energetic costs associated with topological transformations are typically low in liquids and gases [77], they tend to become prohibitively large in entangled solids [5, 63]. This fact has profound consequences for the stability and function of natural and engineered structures, from the microscopic knots in DNA [129, 78], proteins [141, 85, 15, 29, 52] and polymers [56, 10, 106] to knitted clothes [143] and macroscopic meshworks [9]. In each

case, elastic models are crucial in resolving local stresses and strains. However, since basic concepts from elasticity theory and topology remain applicable over this wide range of scales, deciphering the topological principles [19, 5, 63] that determine the mechanical stability of knots and tangles promises insights into a broad spectrum of systems. Hence, it is our main goal here to identify generic topological counting rules that enable us to estimate which members of a given knot family are most robust against untying. To this end, we combine elements from mathematical and physical knot theory [67, 19] with optomechanical experiments and quantitative continuum modeling.

Our analysis is guided by a fundamental problem that is as relevant to the tying of shoe laces [30], surgical sutures [136], and arthroscopic knots [103] as to the staging of a safe prison escape. We are interested in tying two lines together such that they form a stable longer rope, a task known as 'tying a bend' among sailors [3]. Mathematically, this configuration describes an oriented 2-tangle, defined as the union of two oriented open curves embedded in space [1]. Although an elegant mathematical formalism exists to describe certain simple families of 2-tangles [46, 28], very little is known theoretically about even the most basic bend knots used in practice. Physically, such devices may be modelled as elastic fibers in the regime where persistence length dominates system size. Empirical knowledge [3] indicates that many phenomena are independent of the remaining relevant material parameter, the elastic modulus. Below, we construct a topological phase diagram that explains the relative stability of a selection of bends that are commonly used in the sailing and climbing communities. To validate the underlying topological model, we compare its predictions to simulations of an optomechanically verified continuum theory and to quantitative measurements via laboratory 'prison escape' experiments.

4.2 Modelling knots with self-contact and friction

A theoretical description of knots requires a model for self-contact and friction. In this contact, we show how to introduce these features, and describe our model of

knotted ropes.

We assume the knotted ropes are uniform, naturally straight elastic rods, with circular cross section and natural radius and length given by h and L, respectively. The rod has centerline $\boldsymbol{x}(s,t)$, and orthonormal material frame $\{\mathbf{d}_1, \mathbf{d}_2, \mathbf{d}_3\}$ satisfying $\mathbf{d}_i' = \boldsymbol{\kappa} \times \mathbf{d}_i$ and $\dot{\mathbf{d}}_\mathbf{i} = \boldsymbol{\omega} \times \mathbf{d}_i$. In the absence of contact interactions, we describe the underlying elastic fibers by the overdamped Kirchhoff equations (2.33).

$$\frac{\delta \mathcal{E}_b}{\delta \boldsymbol{x}} + \frac{\delta \mathcal{E}_t}{\delta \boldsymbol{x}} + \frac{\delta \mathcal{E}_s}{\delta \boldsymbol{x}} = \eta A \dot{\boldsymbol{x}}'' \tag{4.1}$$

$$\frac{\delta \mathcal{E}_t}{\delta \theta} = 2\eta I (\omega_3 \mathbf{d}_3)'' \cdot \mathbf{d}_3 \tag{4.2}$$

$$\omega_3' + \mathbf{d}_3 \cdot \left(\mathbf{d}_3' \times \dot{\mathbf{d}}_3 \right) = \dot{\theta}' \tag{4.3}$$

where the bend, twist and stretch energies (2.30) are

$$\mathcal{E}_b = \frac{1}{2} \int_0^L ds \; E_b I \kappa^2, \qquad \mathcal{E}_t = \frac{1}{2} \int_0^L ds \; \mu J \theta'^2, \qquad \mathcal{E}_s = \frac{1}{2} \int_0^L ds \; EA \left(|\boldsymbol{x}'| - 1 \right)^2$$

Here, we have distinguished between the Young's modulus E, and the bending modulus E_b. In general $E_b = E$, however for some fibers, E_b may be up to two orders of magnitude smaller. We take $\mu = E_b/(2 + 2\nu)$. For a circular cross section, the parameters A, I, J, are given by $A = \pi h^2$, and $J = 2I = \pi h^4/2$, as before.

To discuss the dynamics, we define the scalar $\omega = \boldsymbol{\omega} \cdot \mathbf{d_3}$, so ω is the angular velocity in the tangential direction.

Simulation framework

Along with the elastic Kirchhoff forces, our simulation includes terms to account for contact, damping, and friction-like collision interactions [108]. We begin by discretizing the rod into $n + 2$ beads at positions $\boldsymbol{x}_0, ..., \boldsymbol{x}_{n+1}$ and $n + 1$ links [14], where the i'th link lies between the i and $i + 1$'th beads (Fig. 3-9B). The material frame is naturally defined on the links [14], giving angles $\theta_0, ...\theta_n$. We must additional keep track of the angular velocity component $\omega_3 = \boldsymbol{\omega} \cdot \mathbf{d}_3$. To simplify notation, we set $\omega := \omega_3$ in this section, so the discretized angular velocities defined on the links are

$\omega_0, ...\omega_n$. The discretized bending, twisting and stretching energies give the elastic force $\mathbf{F}_i^{\text{elast}}$ on the i'th bead of the rod. The torque, τ_i^{elast} on the i'th link is obtained similarly.

Contact forces

To model the soft contacts inside knots, consider the compression strain due the contact between link i and j of the rod, given by $p_{ij} = 1 - R_{ij}/2h$, where R_{ij} is the distance between the midpoints of the links. To derive the contact force we postulate a quartic strain potential

$$V(p) = \frac{1}{2}\left(p^2 + p_0^2 p^4\right)$$

This compression energy is quadratic for small strain but becomes nonlinear when $p^2 \sim p_0^2 p^4$. This occurs when $p \sim 1/p_0$. We assume that the linear elastic response to compression is valid up to 15% compression strain, which gives $p_0^2 = 50$. The contact force on the i'th link is then $KA_{ij}V'(p_{ij})$ where K is the bulk modulus, given by $K = E/(3-6\nu)$, and A_{ij} is the contact area, calculated by approximating the links as cuboids. We convert this link force into a force on beads as follows. The total contact force on the i'th bead is given by averaging over the forces on the links either side of this bead, namely the i'th and $(i-1)$'th link. This gives

$$\mathbf{F}_i^{\text{con}} = \frac{1}{2}\sum_{\langle i-1,j\rangle} KA_{i-1,j}V'(p_{i-1,j}) + \frac{1}{2}\sum_{\langle i+1,j\rangle} KA_{i+1,j}V'(p_{i+1,j}) \tag{4.4}$$

where the angle brackets denote rod elements (beads or links) in contact. In the continuum case, this would become a contact force density

$$\boldsymbol{f}^{\text{con}}ds = Kds\int_0^L ds'\, V'\left(1 - \frac{|\boldsymbol{x}(s) - \boldsymbol{x}(s')|}{2h}\right) \tag{4.5}$$

Internal damping forces

The internal damping on the i'th bead or link is simulated via forces and torques proportional to the relative velocities and angular velocities (respectively) between the i'th and $(i \pm 1)$'th elements.

$$\mathbf{F}_i^{\text{damp}} = -\eta A \left(\frac{\dot{\boldsymbol{x}}_i - \dot{\boldsymbol{x}}_{i-1}}{\ell_{i-1}} + \frac{\dot{\boldsymbol{x}}_i - \dot{\boldsymbol{x}}_{i+1}}{\ell_i} \right)$$
$$\tau_i^{\text{damp}} = -\eta J \left(\frac{\omega_i - \omega_{i-1} \mathbf{d}_3^i \cdot \mathbf{d}_3^{i-1}}{\ell_{i-1}} + \frac{\omega_i - \omega_{i+1} \mathbf{d}_3^i \cdot \mathbf{d}_3^{i+1}}{\ell_i} \right)$$

where ℓ_i is the neutral length of the i'th link, and η is the damping coefficient. Note that these damping terms are essentially second (spatial) derivatives of the velocities, while η plays the role of a diffusion constant

$$\mathbf{F}_i^{\text{damp}} = -\eta A \left(\frac{\dot{\boldsymbol{x}}_i - \dot{\boldsymbol{x}}_{i-1}}{\ell_{i-1}} + \frac{\dot{\boldsymbol{x}}_i - \dot{\boldsymbol{x}}_{i+1}}{\ell_i} \right) = \eta A \bar{\ell}_i \, \partial_{ss} \dot{\boldsymbol{x}}_i + O(\ell_i^2)$$

where $2\bar{\ell}_i = \ell_i + \ell_{i-1}$ for $1 \leq i \leq n$ and $2\bar{\ell}_i = \ell_i$ for $i = 0, n+1$. In particular, η/ρ has the dimensions of a diffusion constant, so $\rho L^2/\eta$ is the relaxation timescale for the damping forces.

Friction-like collision forces

At locations where the rod is in contact with itself, there are additional collision terms. We assume the rod elements (beads and links) in a self-contact region want to equilibrate their velocities, which suggests four types of interaction: the velocity of a bead can influence the velocity or angular velocity of another element, and the angular velocity of a link can influence the velocity or angular velocity of another element. We consider problems where a knot is pulled, so only linear velocity is directly supplied to the rope. Thus we focus on the former two interactions, and neglect the others. The velocity equilibration assumption suggests $\mathbf{F}_i^{\text{col}} = f\left(\dot{\boldsymbol{x}}_i - \dot{\boldsymbol{x}}_{j_1},\ \dot{\boldsymbol{x}}_i - \dot{\boldsymbol{x}}_{j_2}, \dots\right)$ when the

i'th and j_r'th beads are in contact. By analogy with $\mathbf{F}^{\text{damp}}$, we will set

$$\mathbf{F}_i^{\text{col}} = -\eta A \bar{\ell}_i \sum_{\langle i,j \rangle} \frac{\dot{\boldsymbol{x}}_i - \dot{\boldsymbol{x}}_j}{\ell_{ij}^2} \tag{4.6}$$

where ℓ_{ij} is the distance between the i'th and j'th beads. Note that $\mathbf{F}_i^{\text{damp}}$ can be written in the same form when $\ell_i = \ell_{i-1}$. By the same logic, we find the collision torque

$$\tau_i^{\text{col}} = -\eta J \ell_i \sum_{\langle i,j \rangle} \frac{1}{\bar{\ell}_{ij}^2} \left(\omega_i - \frac{(\hat{\boldsymbol{r}}_{ji} \times (\dot{\boldsymbol{x}}_j - \dot{\boldsymbol{x}}_i)) \cdot \mathbf{d}_3^i}{\bar{\ell}_{ij}} \right) \tag{4.7}$$

where $\bar{\ell}_{ij}$ is the distance between the i'th link and the j'th bead, and $\hat{\boldsymbol{r}}_{ji}$ is the unit vector pointing from the i'th link to the j'th bead. Since we are directly supplying the knot with linear velocity, we will neglect the ω term in τ^{col}.

These forms of the collision terms are appropriate for $\ell_i/\ell_{ij} = O(1)$. In a continuum theory, the collision force on a fiber element should be expressed as an integral. Accordingly, we can make the the $\bar{\ell}_j$ dependence of $\mathbf{F}_i^{\text{col}}$ explicit.

$$\mathbf{F}_i^{\text{col}} = -\eta A \bar{\ell}_i \bar{\ell}_j \sum_{\langle i,j \rangle} \frac{\dot{\boldsymbol{x}}_i - \dot{\boldsymbol{x}}_j}{\ell_{ij}^3} \tag{4.8}$$

This differs from the earlier expression (4.6) by an $O(1)$ factor. In particular, modifying η only by an $O(1)$ factor will make them equivalent. The same argument gives the following expression for the collision torque

$$\tau_i^{\text{col}} = \eta J \ell_i \ell_j \sum_{\langle i,j \rangle} \frac{1}{\bar{\ell}_{ij}^3} \left(\frac{(\hat{\boldsymbol{r}}_{ji} \times (\dot{\boldsymbol{x}}_i - \dot{\boldsymbol{x}}_j)) \cdot \mathbf{d}_3^i}{\bar{\ell}_{ij}} \right) \tag{4.9}$$

where the ω term has been neglected. In the continuum case, we find expressions for

the collision force density $\boldsymbol{f}^{\text{col}}$ and collision torque density $\tilde{\tau}^{\text{col}}$

$$\begin{aligned}
\boldsymbol{f}^{\text{col}}(s)ds &= -\eta A ds \int_0^L ds'\, \Theta\left(1 - \frac{|\boldsymbol{x}(s) - \boldsymbol{x}(s')|}{2h}\right) \frac{\dot{\boldsymbol{x}}(s) - \dot{\boldsymbol{x}}(s')}{|\boldsymbol{x}(s) - \boldsymbol{x}(s')|^3} \\
\tilde{\tau}^{\text{col}}(s)ds &= \eta J ds \int_0^L ds'\, \Theta\left(1 - \frac{|\boldsymbol{x}(s) - \boldsymbol{x}(s')|}{2h}\right) \frac{(\boldsymbol{x}(s') - \boldsymbol{x}(s)) \times (\dot{\boldsymbol{x}}(s') - \dot{\boldsymbol{x}}(s)) \cdot \mathbf{d}_3(s)}{|\boldsymbol{x}(s) - \boldsymbol{x}(s')|^4}
\end{aligned} \tag{4.10}$$

where Θ is the Heaviside step function. In discrete form, the equations of motion for the i'th bead and link are

$$\begin{aligned}
\mathbf{F}_i^{\text{elast}} + \mathbf{F}_i^{\text{con}} + \mathbf{F}_i^{\text{ext}} &= \eta A \sum_{j=i\pm1} \frac{\dot{\boldsymbol{x}}_i - \dot{\boldsymbol{x}}_j}{\ell_{ij}} + \eta A \bar{\ell}_i \bar{\ell}_j \sum_{\langle i,j \rangle} \frac{\dot{\boldsymbol{x}}_i - \dot{\boldsymbol{x}}_j}{\ell_{ij}^3} \\
\tau_i^{\text{elast}} + \tau_i^{\text{ext}} &= \eta J \sum_{j=i\pm1} \frac{\omega_i - \omega_j \mathbf{d}_3^i \cdot \mathbf{d}_3^j}{\ell_{ij}} + \eta J \ell_i \ell_j \sum_{\langle i,j \rangle} \frac{(\hat{\boldsymbol{r}}_{ji} \times (\dot{\boldsymbol{x}}_i - \dot{\boldsymbol{x}}_j)) \cdot \mathbf{d}_3^i}{\bar{\ell}_{ij}^4}
\end{aligned} \tag{4.11}$$

For simplicity, we use the same coefficient η in the damping forces and interaction forces. These coefficients do not need to be equal in general, however. We can confirm that the overdamped approximation is appropriate in this case. Let T be the timescale relevant for knot tightening, and recall that the timescale of equilibration is $T_0 \sim \rho L^2/\eta$. When modelling tightening knots, we have $T_0/T \ll 1$. The relationship between inertia and damping may be written in terms of these timescales

$$\frac{\text{inertia}}{\text{damping}} = \frac{\rho A \ell_i \frac{L}{T^2}}{\eta A \ell_i \frac{L}{TL^2}} = \frac{\rho L^2}{T\eta} = \frac{T_0}{T} \ll 1$$

Within this framework, we consider three types of boundary conditions

$$\begin{aligned}
\text{Free end: } & \mathbf{F}_i^{\text{ext}} = 0,\ \tau_i^{\text{ext}} = 0 \\
\text{Clamped end: } & \mathbf{F}_i^{\text{ext}} = -\mathbf{F}_i^{\text{elast}},\ \tau_i^{\text{ext}} = -\tau_i^{\text{elast}},\ \mathbf{F}_i^{\text{damp}} = 0,\ \tau_i^{\text{damp}} = 0 \\
\text{Pulled end: } & \mathbf{F}_i^{\text{ext}} = \mathbf{F}^{\text{pull}},\ \tau_i^{\text{ext}} = -\tau_i^{\text{elast}}
\end{aligned}$$

At clamped and pulled ends, we assume that $\mathbf{F}_i^{\text{con}} = \mathbf{F}_i^{\text{col}} = 0$ and $\tau_i^{\text{col}} = 0$. The prison escape experiments consist of two ropes, labelled a, b, with 4 ends in total (Fig. 4-7). Suppose their indices are a_0, b_0, a_1, b_1. To test for stability, we simulate clamping one

end and pulling on another until the ropes separate out, which corresponds to the following boundary conditions

$$\text{Free end: } a_0, b_0$$

$$\text{Clamped end: } a_1$$

$$\text{Pulled end: } b_1$$

and $\mathbf{F}_i^{\text{ext}}$ and τ_i^{ext} vanish everywhere else.

Friction measurement

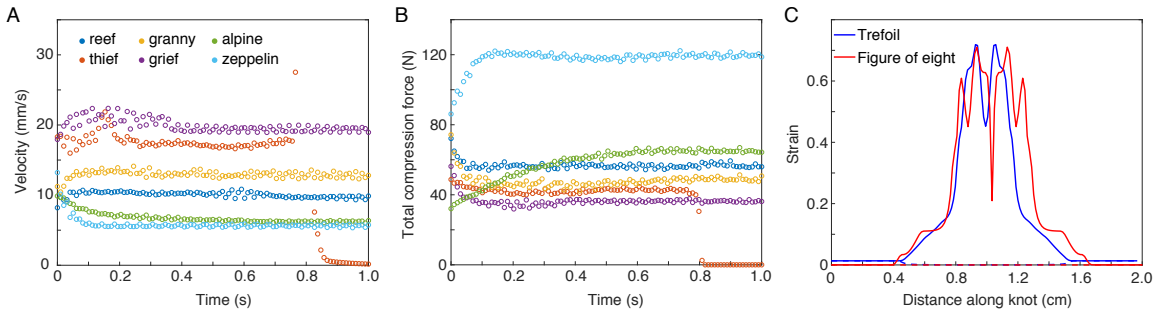

Figure 4-1: **Simulation data reveal the interactions that govern knot mechanics.** (**A**) Velocity at the pulled end provides a consistent way of differentiating between knots. Stronger knots move at a lower velocity. The thief knot unties completely after 0.7 s. (**B**) Measurement of Coulomb type friction forces yields the same knot rankings as the velocity based friction parameter. The total compression force is the sum of the elastic forces compressing a every link of the fiber. (**C**) Twist strain (dashed lines) is a negligible contribution to total strain (solid lines) in the tight trefoil and figure-of-eight knots.

To understand the relationship between the damping model described above and traditional Coulomb friction, we consider a simple continuum test problem of a pinched rope. The rope is described by $\boldsymbol{x}(s,t) = (s + u(s,t), 0, 0)$ for $s \in [-L/2, L/2]$ with $u(s,0) = 0$. Suppose the rope is pinched along the region $-a/2 < s < a/2$, compressing the rope by $h - \ell/2$ on each side, where h is the rope radius. The rope

is pulled to the right by a constant force $F > 0$. The equation of motion is

$$EAu_{ss} + \eta A u_{tss} = \begin{cases} 0 & s+u < -a/2 \\ \frac{2\eta A}{\ell^2} u_t & -a/2 < s+u < a/2 \\ 0 & a/2 < s+u \end{cases}$$

$$EAu_s(L/2,t) = F$$

$$EAu_s(0,t) = 0$$

We will look for solutions with $u_t = v$ is constant. We find $u_{ss} = 0$ for $|s+u| > a/2$. Using the boundary condtions this has solution

$$u_s = \begin{cases} 0 & s+u < -a/2 \\ \frac{F}{EA} & s+u > a/2 \end{cases}$$

In the pinched region, $|s+u| < a/2$, we have

$$u_{ss} = \frac{2\eta v}{\ell^2 E} = V$$

We look for solutions of the form $u_s = f(s+u)$, so $u_{ss} = f'(1+f) = V$. This gives solution

$$u_s = \sqrt{2V(s+u)+c} - 1$$

Matching u_s at $s+u = \pm a/2$ gives $c = 1 + Va$ and

$$\sqrt{2Va+1} = \frac{F}{EA} + 1$$

$$\frac{4\eta A v a}{\ell^2} = \frac{F^2}{EA} + 2F$$

Thus v carries information about the total friction. Assuming that F/EA is small,

we can take the following dimensionless parameter as a measure of friction (Fig. 4-7)

$$c_f = \frac{F\ell}{\eta A v}$$

For knots, we set $\ell = 2h$, and take v to be the relative velocity of the pulled end to the clamped end.

Now consider Coulomb friction. This depends upon a normal reaction force, F_N, due to the pinching. This force should increase as a increases or ℓ decreases, just like the parameter c_f. Thus we expect c_f to produce the same ranking of knots as Coulomb friction (Fig. 4-1A,B).

4.3 Optomechanical fiber experiments

The optomechanical experiments use color-changing photonic fibers recently developed by Mathias Kolle's lab [79], that allow for the direct imaging of strain in knots (Fig. 4-2A,B). These fibers derive structural color from a multilayer cladding, composed of alternating layers of transparent elastomers with distinct refractive indices, wrapped around an elastic core. Their coloration varies with the thickness of layers in the periodic cladding, which changes upon elongation or bending. Our theoretical framework is validated through direct comparison with photographs obtained by Joseph Sandt, depicting the strain-induced color changes in mechano-responsive photonic fibers (Fig. 4-2A-C). Simulating the tightening process of a 1-tangle, corresponding to a single knotted fiber pulled at both ends (Fig. 4-2A,B), reveals the relative strengths and spatio-temporal localization of the bending and stretching strains (Fig. 4-2D,E), which are not individually discernible in our experiments.

Given material parameters for the fibers, our numerical framework is able to simulate the tightening and calculate the strain in the knot. We take material parameters $E = E_b = 1\,\mathrm{MPa}$, $\nu = 0.3$, $h = 0.02\,\mathrm{cm}$, $\rho = 1\,\mathrm{g\,cm^{-3}}$, and pulling force $F = 0.02\,\mathrm{N}$ at both pulled ends. To set the damping parameter η, recall that the timescale for equilibration within a fiber of length L is $T_0 \sim \rho L^2/\eta$. For realistic fibers, this timescale

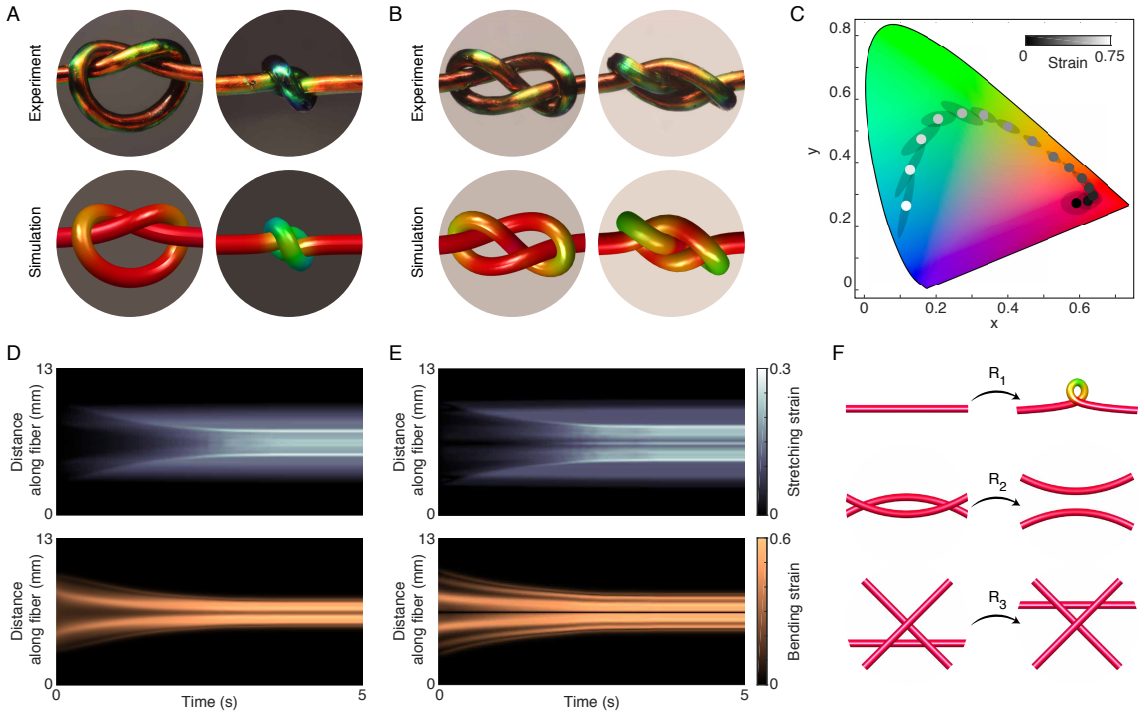

Figure 4-2: **Experiments and simulations reveal mechanical properties of knots.** (**A, B**) Experiments conducted by Joseph Sandt with color-changing, mechano-responsive fibers confirm the stress patterns predicted by continuum simulations for the trefoil knot (A) and figure-of-eight knot (B) over the tightening process. Fiber diameter 0.4 mm. (**C**) The dependance of fiber color on strain is visualized as a trajectory in the CIE 1931 XYZ color space. This strain color coding is used in panels (A), (B) and (F). (**D**, **E**) Simulations reveal the relative strength of bending and stretching strains along knots. Panels (D) and (E) show the evolution of these two complementary strain contributions during tightening of the trefoil in (A) and the figure-of-eight knot in (B). Pulling force 0.02 N and elastic moduli are given in Section 4.3. (**F**) The topology-preserving Reidemeister moves are not all physically equivalent, as R_1 requires higher energy than R_2 and R_3, highlighting that both topological and elastic properties determine the mechanical behavior of knots.

is fast. We assume that when a fiber of length 1 m is stretched, the strain equilibrates in $O(1)$s. This gives $\eta = 10^4\,\mathrm{g\,cm^{-1}\,s^{-1}}$ in cgs units. The simulated fibers are colored according to a measure of true strain. At position s along the fiber, this measure is given by the maximum value of $\log\left(1+\sqrt{\epsilon_{ij}\epsilon_{ij}}\right)$ on the boundary of the cross section $C(s)$ at s, where

$$\max_{\partial C(s)} \epsilon_{ij}\epsilon_{ij} = \frac{1}{2}h^2\theta'(s)^2 + \left(h\kappa(s) + |\boldsymbol{x}'| - 1\right)^2$$

While the colored fibers do not respond to twist, the twist strain in the trefoil and figure-of-eight knots (Fig. 4-2) is negligible (Fig. 4-1C).

The Kirchhoff model highlights why topological considerations [1] alone do not suffice to explain the mechanical behaviors [3] of real-world knots: Loosening or tightening a knot transforms any of its planar projections according to a sequence of three elementary topology-preserving Reidemeister moves, R_1, R_2 and R_3 (Fig. 4-2F). Despite being topologically equivalent, the move R_1 is energetically distinct as it involves significant changes in strain, whereas moves R_2 and R_3 are energetically favored soft modes (Fig. 4-2F), implying that physical knots preferentially deform via R_2 and R_3. Thus, to link the physical properties of tangled fibers to their topology, one must merge concepts from classical mathematical knot theory [1] with elasticity theory [19, 87, 5, 63].

4.4 Twist fluctuation energy

Continuum simulations provide guidance for how one can complement bare topological knot diagrams [1] with coarse-grained mechanical information that is essential for explaining why certain popular knots are more stable than others (Fig. 4-3). In contrast to a 1-tangle, which is tightened by pulling diametrically at its only two ends (Fig. 4-3A), each strand of a bend knot has one pulled and one free end (Fig. 4-3B). Consequently, the local fiber velocity directions in the center-of-mass frame of the bend knot define natural fiber orientations on the underlying 2-tangle (Fig. 4-3B), thus establishing a mapping between bend knots and oriented 2-tangles. At each contact crossing, the fibers mutually generate a frictional self-torque with well defined handedness, depending on the relative velocity and ordering of the two fiber strands (Fig. 4-3B,C). In analogy with the coarse-graining procedure underlying Ising-type spin models, we can associate a unit twist charge $q_i = \pm 1$ with each vertex i in the planar 2-tangle diagram, where the sign of q_i reflects the combined handedness of the torques acting on the two intersecting strands (Fig. 4-3C). In this section, we will show that the sum $Wr = \sum_i q_i$, mathematically known as the writhe, represents

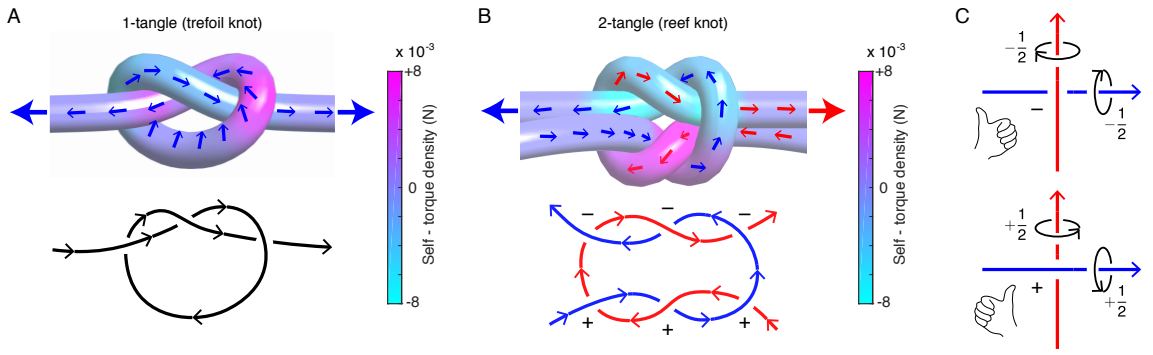

Figure 4-3: **Topology and self-twisting in 1-tangles and 2-tangles.** (**A**) Top: A 1-tangle is tightened by pulling its two ends in opposite directions (large exterior arrows). The induced fiber velocity field (small interior arrows) in the center-of-mass (c.o.m.) frame reverses its orientation near the fiber midpoint. Bottom: As the velocity field is incompatible with any chosen global fiber orientation (black arrows), self-torque data cannot be consistently assigned to a topological 1-tangle diagram. (**B**) Top: Due to the presence of the two free ends, the pulling directions of a bend knot (large exterior arrows) define a canonical global orientation on each of the two fibers in the corresponding 2-tangle.
Bottom: The alignment of local velocity directions and fiber orientation permits the discretization of self-torque data over crossings by assigning twist charges $q_i = \pm 1$ to each vertex i. (**C**) Each fiber strand passing through vertex i contributes $\pm 1/2$ to the vertex twist charge q_i, with the sign reflecting the handedness of the induced rotation. Blue-blue and red-red self-crossings found in more complex 2-tangles can be labeled accordingly. The sum of the q_i defines the total writhe Wr, providing a coarse-grained approximation of the total self-torque in 2-tangles; the reef knot has $Wr = 0$. Fiber diameter 0.4 mm, pulling force 15 N in (A,B).

the total self-torque of a 2-tangle, establishing a concrete link between topology and mechanics.

Knot theory

To demonstrate the correspondence between writhe and self-torque, we begin by introducing some basic concepts from knot theory. The quantities we consider are well defined on knots and links, i.e. collections of n oriented closed curves embedded in $\mathbb{R}^3$. However, the bend knots we study are oriented 2-tangles, consisting of two open oriented space curves. We will therefore adapt some quantities to deal with the open curve case. A diagram will refer to a 2D projection of the knot, link or tangle

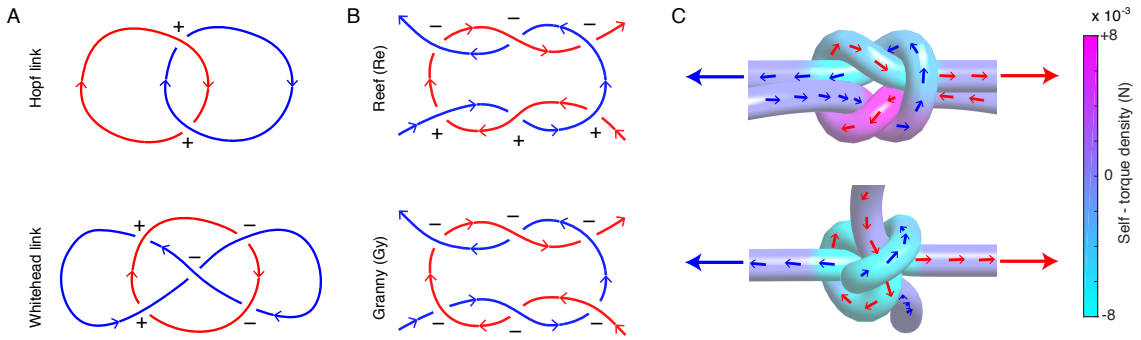

Figure 4-4: **Link, writhe and self-torque.** (**A**) The linking number (Lk) is the sum of the signs of the crossings between the two separate components of the diagram, while the writhe (Wr) is the total signed crossing number. For example, the Hopf link (top) has $Lk = Wr = 2$ while the Whitehead link (bottom) has $Lk = 0$, $Wr = -1$. (**B,C**) Signed crossing data from knot diagrams oriented by pulling direction correctly predict the difference in self-torque between the reef and granny knots. (**C**) Pulling direction (large arrows) defines a knot orientation which is aligned with normalized fiber velocity (small arrows) in the center-of-mass frame. Apparent differences in velocity magnitude are due to out of plane effects. (Diameter 0.4 mm, pulling force 15 N.)

together with crossing information (Fig. 4-4A,B). Topological equivalence of knots or tangles in space, known as ambient isotopy, descends to diagrams as equivalence under Reidemeister moves $1, 2, 3$ (Fig. 4-2F). Since R_1 is energetically more costly, we will sometimes consider equivalence under just moves R_2 and R_3, known as regular isotopy.

Most of the knot theoretic quantities we need can be defined in terms of knot diagrams. For example the crossing number of a diagram is an easily obtainable measure of complexity. The minimum crossing number of a knot is the smallest crossing number of any diagram of the knot, and is a topological invariant.

Consider now a link consisting of two closed curves C_1, C_2. The linking number, $Lk(C_1, C_2)$ is defined by the signed crossing number of a projection of C_1 and C_2, where only crossings between C_1 and C_2 are counted (Fig. 4-4). This quantity is topological (i.e. an invariant of ambient isotopy) and so does not depend on the projection chosen. On the other hand, the writhe, Wr, is the total signed crossing number of a diagram, and is only invariant under Reidemeister moves R_2 R_3. It

is thus an invariant of regular isotopy and not ambient isotopy. The 3d writhe, $Wr_3(C)$, defined for a single closed curve in space, is given by the average signed crossing number over all projections. Wr_3 is geometrical and so is not constant over different projections.

Writhe and torque

We can now derive the relationship between writhe and self-torque (Fig. 4-4). To do this, we introduce a result about writhe without proof, which we will justify later. We will need the integral expression for Wr_3 of a curve C parametrised by γ

$$Wr_3(C) = \frac{1}{4\pi} \int_{C\times C} \frac{\det\left(\dot{\gamma}(s), \dot{\gamma}(t), (\gamma(s) - \gamma(t))\right)}{|\gamma(s) - \gamma(t)|^3} ds\, dt$$

Using these results, we can deduce a correspondence between Wr_3 and self-torque for a 2-tangle (bend knot). Suppose we are in a regime where the knot pulls through at approximately constant speed. In this 'reptation' limit we expect the velocity to be tangent to the curve up to a global rotation, and the stretching to be roughly constant. Thus $\boldsymbol{v} = v\mathbf{d_3} + \boldsymbol{\Omega} \times \boldsymbol{x}$, and $\boldsymbol{x}' = (1+\epsilon)\mathbf{d_3}$ for constant v, ϵ, Ω. We further assume ϵ is small, and can be neglected. Let the components of the bend knot be C_1 and C_2, oriented by pulling direction, and let C be a closure of C_1, C_2 such that C is a single oriented closed curve. Extending $\boldsymbol{x}, \mathbf{d_3}$ etc. to C gives

$$\begin{aligned} Wr_3(C) &= \frac{1}{4\pi} \int_{C\times C} \frac{\boldsymbol{x}'(s) \cdot (\boldsymbol{x}'(s') \times (\boldsymbol{x}(s) - \boldsymbol{x}(s')))}{|\boldsymbol{x}(s) - \boldsymbol{x}(s')|^3} ds\, ds' \\ &= \frac{1}{4\pi} \int_{C\times C} \frac{\boldsymbol{x}'(s) \cdot (\boldsymbol{r}(s,s') \times \boldsymbol{x}'(s'))}{|\boldsymbol{r}(s,s')|^3} ds\, ds' \end{aligned}$$

where $\boldsymbol{r}(s,s') = \boldsymbol{x}(s') - \boldsymbol{x}(s)$. Now consider evaluating this integral only over the curves $C' \times C'$ where $C' = C_1 \cup C_2$. Observe that $Wr_3(C)$ is large whenever $|\boldsymbol{r}(s,s')|$ is small, which happens for s close to s' or when the rope touches itself nonlocally.

However, for $s' = s + \delta s$ we find the writhe density vanishes to leading order

$$\begin{aligned}
\mathcal{W}r_3(s,s') &= \frac{\boldsymbol{x}'(s)\cdot(\boldsymbol{r}(s,s')\times\boldsymbol{x}'(s'))}{|\boldsymbol{r}(s,s')|^3} \\
&= \frac{1}{\delta s^3}\boldsymbol{x}'(s)\cdot\left(\delta s\boldsymbol{x}'(s)+\frac{1}{2}\delta s^2\boldsymbol{x}''(s)+\frac{1}{6}\delta s^3\boldsymbol{x}'''(s)\right)\times \\
&\qquad\qquad \left(\boldsymbol{x}'(s)+\delta s\boldsymbol{x}''(s)+\frac{1}{2}\delta s^2\boldsymbol{x}'''(s)\right)+O(\delta s) \\
&= \frac{1}{\delta s^3}\boldsymbol{x}(s)\cdot\big(O(\delta s^4)\big)+O(\delta s) \\
&= O(\delta s)
\end{aligned}$$

Thus Wr_3 is dominated by contributions due to nonlocal rope interactions. Provided the closure C does not introduce more such interactions we can approximate Wr_3 by an integral over the open curves $C'\times C'$

$$\begin{aligned}
Wr_3(C) &= \frac{1}{4\pi}\int_{C\times C}\frac{\boldsymbol{x}'(s)\cdot(\boldsymbol{r}(s,s')\times\boldsymbol{x}'(s'))}{|\boldsymbol{r}(s,s')|^3}ds\,ds' \\
&\approx \frac{1}{4\pi}\int_{C'\times C'}\frac{\boldsymbol{x}'(s)\cdot(\boldsymbol{r}(s,s')\times\boldsymbol{x}'(s'))}{|\boldsymbol{r}(s,s')|^3}ds\,ds' \\
&= \frac{1}{4\pi}\int_{C'\times C'}\frac{\mathbf{d_3}(s)\cdot(\boldsymbol{r}(s,s')\times\mathbf{d_3}(s'))}{|\boldsymbol{r}(s,s')|^3}ds\,ds' \\
&= \frac{1}{4\pi}\int_{C'\times C'}\frac{\mathbf{d_3}(s)\cdot(\boldsymbol{r}(s,s')\times(\mathbf{d_3}(s')-\mathbf{d_3}(s)))}{|\boldsymbol{r}(s,s')|^3}ds\,ds' \\
&= \frac{1}{4\pi v}\int_{C'\times C'}\frac{\mathbf{d_3}(s)\cdot(\boldsymbol{r}(s,s')\times(\boldsymbol{v}(s')-\boldsymbol{v}(s)))}{|\boldsymbol{r}(s,s')|^3}ds\,ds'
\end{aligned}$$

The self-torque due to the interaction forces has a similar form

$$\begin{aligned}
\tilde{\tau}_{\text{self}}(s) &= \eta J\int_{C'\times C'}\frac{\mathbf{d_3}(s)\cdot(\boldsymbol{r}(s,s')\times(\boldsymbol{v}(s')-\boldsymbol{v}(s)))}{|\boldsymbol{r}(s,s')|^4}\Theta(2h-|\boldsymbol{r}|)ds' \\
\tau_{\text{self}} = \int_0^L\tilde{\tau}_{\text{self}}(s)ds &= \eta J\int_{C'\times C'}\frac{\mathbf{d_3}(s)\cdot(\boldsymbol{r}(s,s')\times(\boldsymbol{v}(s')-\boldsymbol{v}(s)))}{|\boldsymbol{r}(s,s')|^4}\Theta(2h-|\boldsymbol{r}|)ds\,ds'
\end{aligned}$$

Finally, we approximate Wr_3 by considering points (s,s') where $|\boldsymbol{r}(s,s')|$ is has a local minimum and $s\neq s'$. This gives approximations for the self-torque and self-torque

density in terms of the writhe and writhe density

$$\frac{1}{\eta J}\tau_{\text{self}} \approx \frac{8\pi v}{h} Wr_3(C)$$
$$\frac{1}{\eta J}\tilde{\tau}_{\text{self}} \approx \frac{8\pi v}{h} \int_C \mathcal{W}r_3(s,s')\, ds'$$

We connect this to the 2d writhe Wr by considering Reidemeister moves. Since moves R_2 and R_3 preserve Wr in any projection and are energetically favored (Fig. 4-2F), we expect $Wr_3(C) \approx Wr_3(C') \approx Wr_3(C_0')$ where C_0' is the elastically relaxed initial configuration of the bend knot. Since this initial configuration is approximately planar and Wr_3 is an average over all 2d projections, we conclude that $Wr_3(C) \approx Wr(C_0')$. Therefore

$$\tau_{\text{self}} \sim Wr(C_0')$$
$$\tilde{\tau}_{\text{self}} \sim \int_{C_0'} \mathcal{W}r_3(s,s')\, ds'$$

Note that the second relationship tells us information about the torque distribution throughout the knot. In the loose state, the self interactions of the knot are effectively a series of 2-particle interactions corresponding to crossings in the relaxed planar diagram. The signs of the crossings therefore correspond to units of self-torque (Fig. 4-4).

The role of regular isotopy and writhe also demonstrates the importance of the energetically gapped Reidemeister move R_1 (Fig. 4-2F) in understanding the configurational complexity of knots. We can think of knots as a collection of R_1 type loops locked in place. Although forming such loops costs bending energy, pulling them out costs twist energy, via the mechanism of writhe-twist conversion.

Twist fluctuation energy

A key puzzle of physical knot theory [19], the empirically observed mechanical difference between the visually similar reef and granny knots (Fig. 4-5A,B), may be understood as a consequence of this torque-writhe correspondence in 2-tangles. The

underlying mechanism becomes evident by considering a pair of crossings as shown in Fig. 4-5C: while equally directed torques lead to rolling, opposite torques promote locking and hence stabilize a knot against untying. The overall stability of 2-tangles therefore depends on the self-torque distribution along the fibers, as encoded by the vertex twist charges $q_i = \pm 1$ in an untightened knot diagram (Fig. 4-5D-F). The above argument suggests the following topological twist fluctuation energy per site,

$$\tau = \frac{1}{N} \sum_i (q_i - \bar{q})^2 \tag{4.12}$$

where N is the crossing number, and $\bar{q} = (1/N) \sum_i q_i = Wr/N$ is the average writhe. This expression can be rewritten in the form of a spin-spin type interaction

$$\begin{aligned}
\tau &= \frac{1}{N} \sum_i (q_i - \bar{q})^2 \\
&= \frac{1}{N} \left(\sum_i q_i^2 \right) - \bar{q}^2 \\
&= 1 - \left(\frac{1}{N} \sum_i q_i \right)^2 \\
&= 1 - \frac{1}{N^2} \sum_i q_i^2 - \frac{2}{N^2} \sum_{i<j} q_i q_j \\
&= \tau_0(N) - \frac{2}{N^2} \sum_{i<j} q_i q_j
\end{aligned}$$

where $\tau_0 = 1 - 1/N$ can be interpreted as a ground state energy density. Strikingly, τ has the form of a ferromagnetic energy for an Ising-type spin model with long-range interactions, emphasizing the picture of knots as strongly coupled systems. From the third equality above, we also find that τ is a function of writhe.

$$\tau = 1 - \left(\frac{1}{N} \sum_i q_i \right)^2 = 1 - \left(\frac{Wr}{N} \right)^2$$

Writhe integral

Writhe, and the closely related link, can also be defined geometrically. This both serves to clarify their meaning and to better understand their mechanical implications.

Consider a smooth map between manifolds of the same dimension $\phi : M \to N$ where N is equipped with a volume form g. The degree of ϕ is defined by

$$\deg \phi = \frac{\int_M \phi^* g}{\int_N g} \in \mathbb{Z}$$

where $\phi^* g$ is the pullback of the form g over M. For example, let M be a surface in $\mathbb{R}^3$ parametrized by $X(u, v) \in \mathbb{R}^3$, and consider the Gauss map

$$\begin{aligned} N : M &\to S^2 \\ X(u, v) &\mapsto \frac{X_u \times X_v}{|X_u \times X_v|} \end{aligned}$$

Then $\phi^* g = K(u, v) du \wedge dv$ where g is the standard volume form on S^2 and $K(u, v)$ is the Gauss curvature of M at $X(u, v)$. The degree of the Gauss map is the total Gauss curvature of M

$$4\pi \deg N = \int_M K du\, dv = \int_M (N_u \times N_v) \cdot N \, du\, dv = \int_M \det dN du\, dv \tag{4.13}$$

The second equality comes from finding the area element on a sphere in terms of u, v. We note that this equality (and the final equality) are artefacts of the embedding in $\mathbb{R}^3$. Since the metric on S^2 is induced by $\mathbb{R}^3$ with the standard Euclidean metric, we can immediately calculate area elements in terms of N_u, N_v. For example, suppose C_1, C_2 are parametrized by $\gamma_1(s), \gamma_2(s)$ respectively, and consider the following map

$$\begin{aligned} \Gamma : C_1 \times C_2 &\to S^2 \\ (s, t) &\mapsto \frac{\gamma_1(s) - \gamma_2(t)}{|\gamma_1(s) - \gamma_2(t)|} \end{aligned}$$

The linking number is given by $lk(C_1, C_2) = \deg \Gamma$.

We can use this formulation of linking number to derive an integral expression for $Lk(C_1, C_2)$, which we will now calculate explicitly. To find the pullback of the volume form on S^2, it convenient to write Γ as a composition of simpler maps

$$\begin{aligned} \alpha : C_1 \times C_2 &\to \mathbb{R}^3 & \beta : \mathbb{R}^3 &\to S^2 \\ (s,t) &\mapsto \gamma_1(s) - \gamma_2(t) & (x,y,z) &\mapsto (\frac{x}{r}, \frac{y}{r}, \frac{z}{r}) \end{aligned}$$

The volume form on S^2 is given by $g = \sin\theta d\theta \wedge d\phi$ in spherical polar coordinates. To calculate $\beta^*(g)$, we use $\cos\theta = z/r$ and $\phi = \arctan y/x$ to find

$$\begin{aligned} \sin\theta d\theta &= -\frac{dz}{r} + \frac{xzdx + yzdy + z^2dz}{r^3} \\ d\phi &= \frac{xdy - ydx}{x^2 + y^2} \end{aligned}$$

Then

$$\begin{aligned} \beta^*(g) &= \frac{(xzdx + yzdy - (x^2+y^2)dz) \wedge (xdy - ydx)}{r^3(x^2+y^2)} \\ &= \frac{zdx \wedge dy + xdy \wedge dz + ydz \wedge dx}{r^3} \\ &= \frac{1}{2r^3}\epsilon_{ijk}x^i dx^j \wedge dx^k \end{aligned}$$

Finally, to pullback the form along α, we use $d\mathbf{x} = \dot{\gamma_1}(s)ds - \dot{\gamma_2}(t)dt$

$$\begin{aligned} \Gamma^*(g) &= \frac{1}{2|\gamma_1(s) - \gamma_2(t)|^3}\epsilon_{ijk}\left(\gamma_1(s) - \gamma_2(t)\right)^i \left(\dot{\gamma_1}(s)ds - \dot{\gamma_2}(t)dt\right)^j \wedge \left(\dot{\gamma_1}(s)ds - \dot{\gamma_2}(t)dt\right)^k \\ &= \frac{(\dot{\gamma_2}(t) \times \dot{\gamma_1}(s)) \cdot (\gamma_1(s) - \gamma_2(t))}{|\gamma_1(s) - \gamma_2(t)|^3} ds \wedge dt \end{aligned}$$

This form is only defined up to an overall sign, since we are free to reverse the orientation of either curve. This freedom matches the topological definition, where the sign of the linking number also depends on arbitrary choices of orientation for the

curves. Thus we find

$$Lk(C_1, C_2) = \frac{1}{4\pi} \int_{C_1 \times C_2} \frac{\det\left(\dot{\gamma_1}(s), \dot{\gamma_2}(t), (\gamma_1(s) - \gamma_2(t))\right)}{|\gamma_1(s) - \gamma_2(t)|^3} ds\, dt \tag{4.14}$$

The writhe is limiting value of this integral as $C_2 \to C_1$

$$Wr_3(C_1) = \frac{1}{4\pi} \int_{C_1 \times C_1} \frac{\det\left(\dot{\gamma}(s), \dot{\gamma}(t), (\gamma(s) - \gamma(t))\right)}{|\gamma(s) - \gamma(t)|^3} ds\, dt \tag{4.15}$$

The linking number is guaranteed to be an integer as it is the degree of a smooth map. The writhe, on the other hand, appears to be the "degree" of a discontinuous map. when $C_1 = C_2$ we find

$$\lim_{t \to s^{\pm}} \Gamma(s,t) = \mp \mathbf{t}(s)$$

As an alternative, we can derive the integral formulas by directly calculating the volume of S^2 covered by the map Γ, instead of calculating the pullback of the volume form. This equivalence is noted above in (4.13) for the case of the Gauss map.

$$Lk(C_1, C_2) = \frac{1}{4\pi} \int_{C_1 \times C_2} (\Gamma_s \times \Gamma_t) \cdot \Gamma \, ds\, dt \tag{4.16}$$

We will explicitly show that (4.16) and (4.14) are equivalent. To simplify notation, let $\mathbf{r}(s,t) = \gamma_1(s) - \gamma_2(t)$ be the pointing vector, and let $P_{ij} = \delta_{ij} - r_i r_j / r^2$ be the projection operator onto the plane normal to r. The derivatives of $\Gamma = \mathbf{r}/r$ then become

$$\begin{aligned} \Gamma_s &= \frac{\dot{\gamma}_1}{r} - \frac{(\mathbf{r} \cdot \dot{\gamma}_1)\, \mathbf{r}}{r^3} = \frac{1}{r} P_{ij} \left(\dot{\gamma}_1\right)_j \\ \Gamma_t &= -\frac{\dot{\gamma}_2}{r} + \frac{(\mathbf{r} \cdot \dot{\gamma}_2)\, \mathbf{r}}{r^3} = -\frac{1}{r} P_{ij} \left(\dot{\gamma}_2\right)_j \end{aligned}$$

Using the multilinear and alternating properties of det, the integrand in (4.16) be-

comes

$$\begin{aligned}(\Gamma_s \times \Gamma_t) \cdot \Gamma &= -\frac{1}{r^3} \det\left(P\dot{\gamma}_1, P\dot{\gamma}_2, \mathbf{r}\right) \\ &= -\frac{1}{r^3} \det\left(\dot{\gamma}_1, \dot{\gamma}_2, \mathbf{r}\right)\end{aligned}$$

Which matches the expression in (4.14) up to a sign. Similarly, letting $C_1 \to C_2$, we find

$$Wr_3(C_1) = \frac{1}{4\pi} \int_{C_1 \times C_1} (\Gamma_s \times \Gamma_t) \cdot \Gamma \, ds \, dt \tag{4.17}$$

We can now show that Wr_3 is the average value of Wr over all projections. Consider changing variables from $(s,t) \in C_1 \times C_1$ to $\boldsymbol{n} \in S^2$ via $d^2\boldsymbol{n} = |\det d\Gamma| \, ds \, dt$. Since the map Γ is many to one, we have to keep track of the sets $\Gamma^{-1}(\boldsymbol{n})$.

$$Wr_3(C_1) = \frac{1}{4\pi} \int_{S^2} \sum_{(s,t) \in \Gamma^{-1}(\boldsymbol{n})} (\Gamma_s \times \Gamma_t) \cdot \Gamma \left|\det d\Gamma|_{(s,t)}\right|^{-1} \, d^2\boldsymbol{n}$$

We can explicitly write down the map $d\Gamma|_{(s,t)}$

$$\begin{aligned} d\Gamma|_{(s,t)} : \mathbb{R}^2 &\to T_{\Gamma(s,t)} S^2 \\ (x,y) &\to x\Gamma_s + y\Gamma_t \\ \det d\Gamma|_{(s,t)} &= (\Gamma_s \times \Gamma_t) \cdot \Gamma \end{aligned}$$

Where the last line follows from considering the area change of a unit cell under by $d\Gamma$. Substituting this into the writhe integral gives

$$Wr_3(C_1) = \frac{1}{4\pi} \int_{S^2} \sum_{(s,t) \in \Gamma^{-1}(\boldsymbol{n})} \operatorname{sgn}\left(\det d\Gamma|_{(s,t)}\right) \, d^2\boldsymbol{n} \tag{4.18}$$

Observe that $\operatorname{sgn}\left(\det d\Gamma|_{(s,t)}\right)$ is simply the sign of the crossing at (s,t) when the curve is projected along the direction $\boldsymbol{n} = \Gamma(s,t)$. The integrand above is therefore the average signed crossing number, or Wr, of the curve, over all projection directions

in S^2.

4.5 Circulation energy

In addition to twist locking for large values of τ, knots can be stabilized when their internal structure forces fiber segments to slide tangentially against each other. For example, the reef knot and the infamous thief knot both have $\tau = 1$ but, because their pulled ends differ, such friction makes the reef more stable (Fig. 4-5D,G). At the coarse-grained level of planar knot diagrams, these friction effects correspond to edge-edge interactions, dominated by pairs of edges sharing a face and pulled in opposite directions (Fig. 4-5D-F). To formalize this notion, each edge around a face F is assigned a weight $+1$ or -1 if it winds around F in the anti-clockwise or clockwise direction, respectively. Each face then contributes a friction 'energy' given by the net circulation of the edges around the face, C_F, normalized by the total number of edges e_F. This yields the total circulation energy

$$\Gamma = \sum_F \frac{|C_F|}{e_F} \tag{4.19}$$

where the sum is taken over all faces of the knot diagram. The normalization encodes the assumption that every face has the same perimeter in the tight limit, ensuring that each face contributes a maximum of $+1$ to Γ.

Whitney index

The circulation energy is related to another fundamental regular isotopy invariant, namely the Whitney index [70], Wh. Unlike the torque-writhe correspondence however, this relationship is informal. The Whitney index is defined as follows. Consider a closed plane curve C, parametrized by $\gamma(s)$, with everywhere nonvanishing tangent vector. We note that C is allowed to be self intersecting, so in particular C can be a

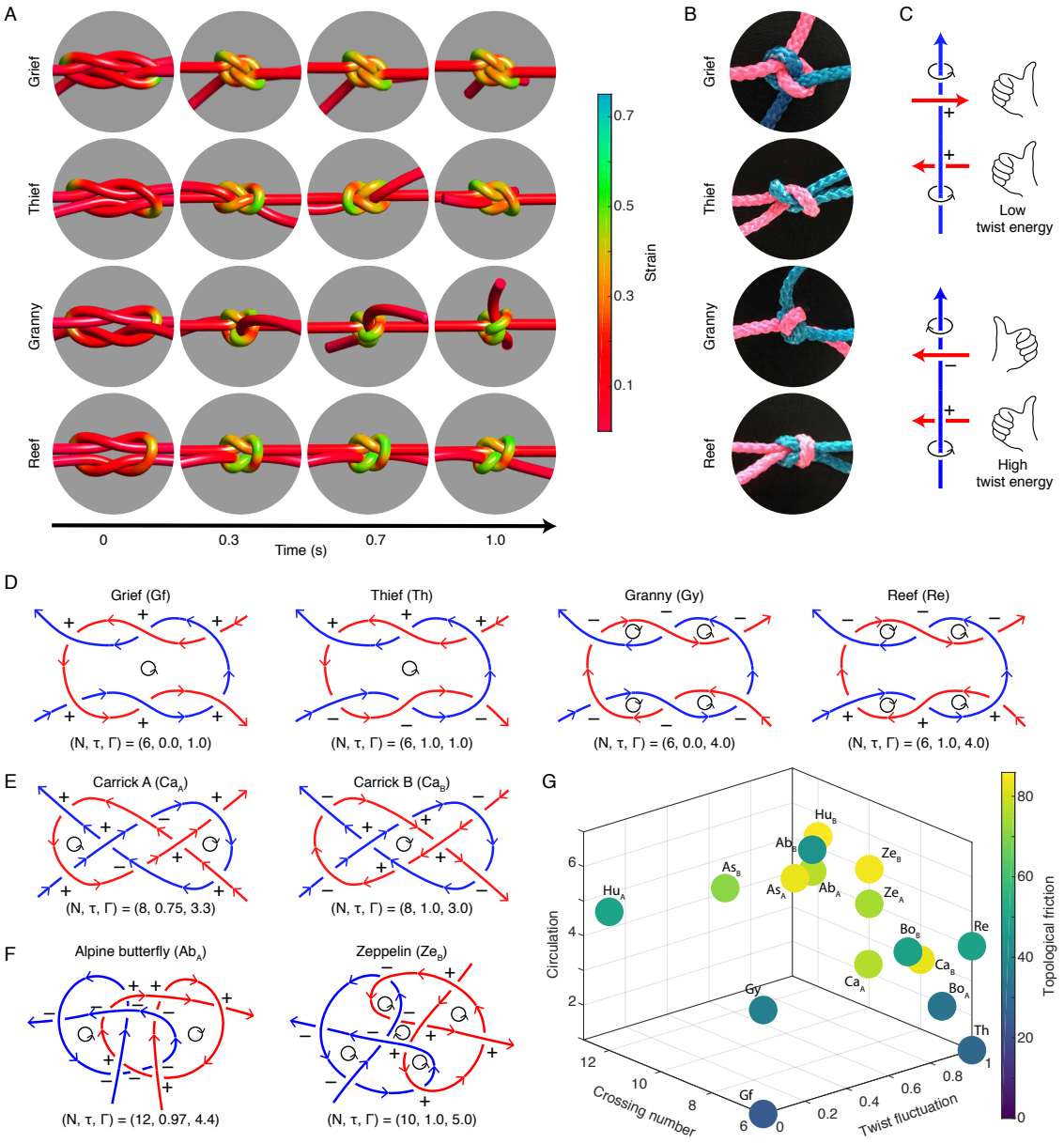

Figure 4-5: **Topology determines the mechanical stability of 2-tangles.** (**A**) Small modifications in topology lead to dramatic changes in the mechanical behavior of 2-tangles, exemplified by the presence or absence of global rotation of the knot body upon pulling; fiber diameter 0.4 mm, pulling force 15 N. Knots are shown in order of least stable (grief) to most stable (reef). (**B**) Simulated tight configurations of knots are validated with real knots tied in nylon rope (diameter 20 mm). (**C**) Tight knots act on themselves via right-handed (positive) and left-handed (negative) torques. Equally directed torques lead to rolling (top), whereas opposite torques promote locking (bottom) and hence stabilize a knot against untying. (Continued on the following page)

Figure 4-5: (D-F) Knot diagrams oriented by pulling direction correspond to a topological state defined as the triple of crossing number N, twist fluctuation τ and circulation Γ. These parameters explain the relative stability of knots in the reef group (D), and Carrick group (E). (F) The zeppelin bend is more stable than the alpine butterfly bend, displaying both higher twist fluctuation and higher circulation. (G) The topological state reveals the underlying structure of bend knots, and separates stable knots from unstable knots. The dimensionless topological friction, obtained from simulation, is determined by the velocity response when the knot is pulled with a given force, and is a measure of the friction force due to the knot. Labels in (G) correspond to those in (D,E,F) and additional knots listed in Fig. 4-7.

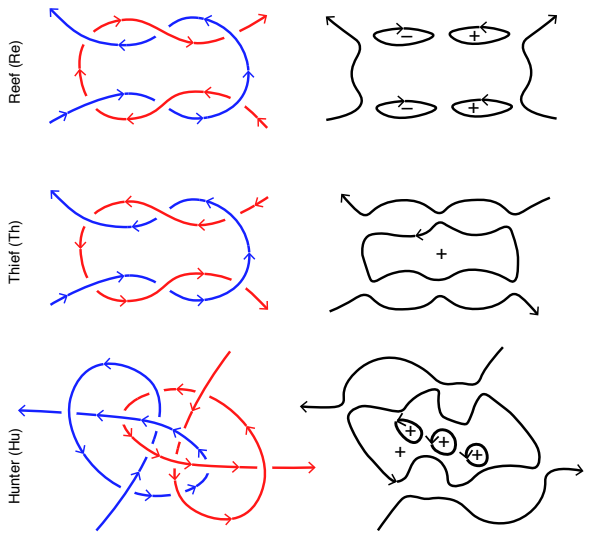

Figure 4-6: **Whitney index for bend knots.** The Whitney index of an oriented plane curve is calculated by resolving crossings and summing the signs of all resulting closed loops.

nontrivial knot diagram. The Whitney index is the degree of the map

$$\phi : C \to S^1$$
$$s \to \frac{\dot{\gamma}(s)}{|\gamma(s)|}$$

This definition can be extended to a collection of open curves by resolving the crossings of C (Fig. 4-6). This geometric picture suggests that Wh could yield another topological counting rule or even a spin system analogy in the same way as Wr. However we note that while the Whitney index does distinguish between the reef and thief knots, which was the main motivation behind introducing the circulation energy

Γ, it does not present a coherent physical picture for more complex knots (Fig. 4-6).

4.6 Topological counting rules

The topological parameters N, τ and Γ allow us to rationalize the stability of a large class of popular knots used by sailors and climbers (Fig. 4-5G). These variables are both easy to evaluate from knot diagrams (Fig. 4-5D-F) and reflect topology-induced forces and torques throughout the knot. As such, the triplet (N, τ, Γ) captures both essential topological and mechanical structure hidden within knots. The (N, τ, Γ) phase diagram explains existing empirical knowledge for simple knots [3] as well as predictions of the Kirchhoff model about the relative strength and stability of more complex 2-tangles (Fig. 4-5G). We verified these predictions independently in experiments by mimicking the prisoner's escape problem (Fig. 4-8A) with two thin Dyneema fibers tied together. Of the two pulled ends for each knot, one is fixed in the experimental apparatus, with the other being perturbed while suspending incrementally higher masses until the knot pulls through. Although the Kirchhoff model cannot account for surface contact details [87], the experimental data for the critical loads agree quantitatively with the simulations for simple knots and, more importantly, confirm the predicted qualitative stability differences between various commonly used knots (Fig. 4-8B). Notably, both theory and experiments indicate that the zeppelin knot is more secure against untying than the popular alpine butterfly (Fig. 4-8B,C).

For the prison escape simulations we take material parameters corresponding to a thin, flexible nylon fiber, $E = 1\,\mathrm{GPa}$, $E_b = 0.1\,\mathrm{GPa}$, $\eta = 10^6\,\mathrm{g\,cm^{-1}\,s^{-1}}$, $\nu = 0.3$, $h = 0.02\,\mathrm{cm}$, $\rho = 1\,\mathrm{g\ cm^{-3}}$, and pulling force $F = 15\,\mathrm{N}$ at both pulled ends. Note that η here is much larger than for the optomechanical fiber simulations, due to the fact that nylon is less flexible. While the framework described above could in principle be used to simulate stiffer rods, this would require smaller time-steps.

4.7 Experimental methods

Optomechanical experiments relating knot color to fiber strain

Optomechanical fiber experiments were performed by Joseph Sandt, using a strain-sensitive, color-changing elastomer photonic fiber [79]. The color map relating the observed color of the fiber to its logarithmic strain, ϵ, was obtained experimentally. One end of the fiber was fixed to a load cell, and the other was fixed to a motorized translation stage, allowing the fiber to be stretched to any predetermined strain value. Color data were collected by stretching the fiber from $\epsilon = 0$ to $\epsilon = 0.7$ and back to $\epsilon = 0$, in strain increments of 0.05. As the fiber was stretched and relaxed, we kept track of 5 equally spaced material points. At each level of strain, reflection spectra (normalized to complete reflection of the light source) were collected from each of these 5 points using a custom microscope [123] with input illumination from a Thorlabs SLS201 stabilized broadband light source, and output via optical fiber to a spectrometer. Each spectrum was converted into tristimulus values X, Y and Z in the CIE 1931 color space, and transformed to (x, y) co-ordinates representing the colors in the CIE x-y chromaticity diagram. The mean (x, y) co-ordinates for different strains lie on a curve in CIE space (Fig. 4-2C). Uncertainty in these co-ordinates is represented by standard deviation ellipses oriented according to the principal directions of the data (obtained from principal component analysis), with axis lengths given by the corresponding standard deviations in these directions. A more thorough description of the stretching and optical measurement process, and the custom microscope used therein, may be found in earlier work [123]. The colormap obtained from this process contains color data for 15 strain values from $\epsilon = 0$ to $\epsilon = 0.7$. In simulations we use a colormap with values for intermediate strains generated by linear interpolation.

Images of knots tied in an elastomer photonic fiber were collected using a Canon EOS Rebel T3i DSLR camera fitted with a macro lens. Photos were taken at 4x magnification with the f-stop set to f/16. The distance between the fiber and the camera lens was typically a few centimeters. The samples were prepared by initially tying a loose knot in the fiber. Each end was then gripped in a small drill chuck affixed

to translational and rotational stages (Fig. 4-9A). These stages allowed for controlled tightening and rotation of the knot, in order to capture images at desired angles. A tubular fluorescent light positioned above and behind the camera illuminated the fiber.

'Prison escape' experiments: testing the stability of bend knots

The 'prison escape' experiments were conducted in collaboration with Joseph Sandt. To determine the relative stability of bend knots joining two lines, each knot was set up with one end of the first line fixed in a drill chuck, and one end of the second line fed over a pulley to be loaded with mass (Fig. 4-9B,C). The other end of each line was left free. Masses were suspended from the pulled end, while perturbations were applied to the knot by flicking the line down and up near the body of the knot. The perturbation device consisted of a plastic arm tipped with silicone tubing, manipulated by an Arduino-driven servomotor (Fig. 4-9C). The flick was triggered manually by a button press. Experimental trials consisted of tying a bend and affixing it within the system, starting with a relatively low mass on the pulled end. The knot was flicked five times at each mass. Upon observing motion (i.e. partial or complete pull-through of either line through the knot), the weight of the mass at which the knot slipped was recorded. In the absence of observable motion, the mass was increased by 20 grams and the line was flicked five more times. This incremental increase of pulling mass continued until motion was observed. A camera was used to record the behavior of the knot in each experiment, to verify observations of motion. Berkley FireLine (6-lb test, "Smoke" color) was used in all such stability experiments.

4.8 Conclusions

To conclude, the above analysis shows how basic topological counting rules can be used to estimate the relative stability of frequently encountered knots and tangles. From a theoretical perspective, the parallels with long-range coupled spin systems suggest that the statistical mechanics [85, 1] of general knotted structures can be for-

mulated within this framework. Tangled vortices [76, 77] in complex fluids and defect loops in liquid crystals [135] may permit a statistical description through reduction to topological crossing diagrams. In elastic systems, joint experimental and theoretical progress is needed to untangle longstanding puzzles regarding the statistics of knots in DNA [129] and proteins [141, 85, 15, 29], where thermal effects induce a finite persistence length, and other macroscopic structures [9, 143]. In sailing, climbing and many other applications, non-topological material parameters and contact geometry [87] also play important mechanical roles, and must be included in more refined continuum models to quantitatively describe practically relevant knotting phenomena. From a broader conceptual and practical perspective, the above topological mechanics framework seems well-suited for designing and exploring new classes of knots with desired behaviors under applied load.

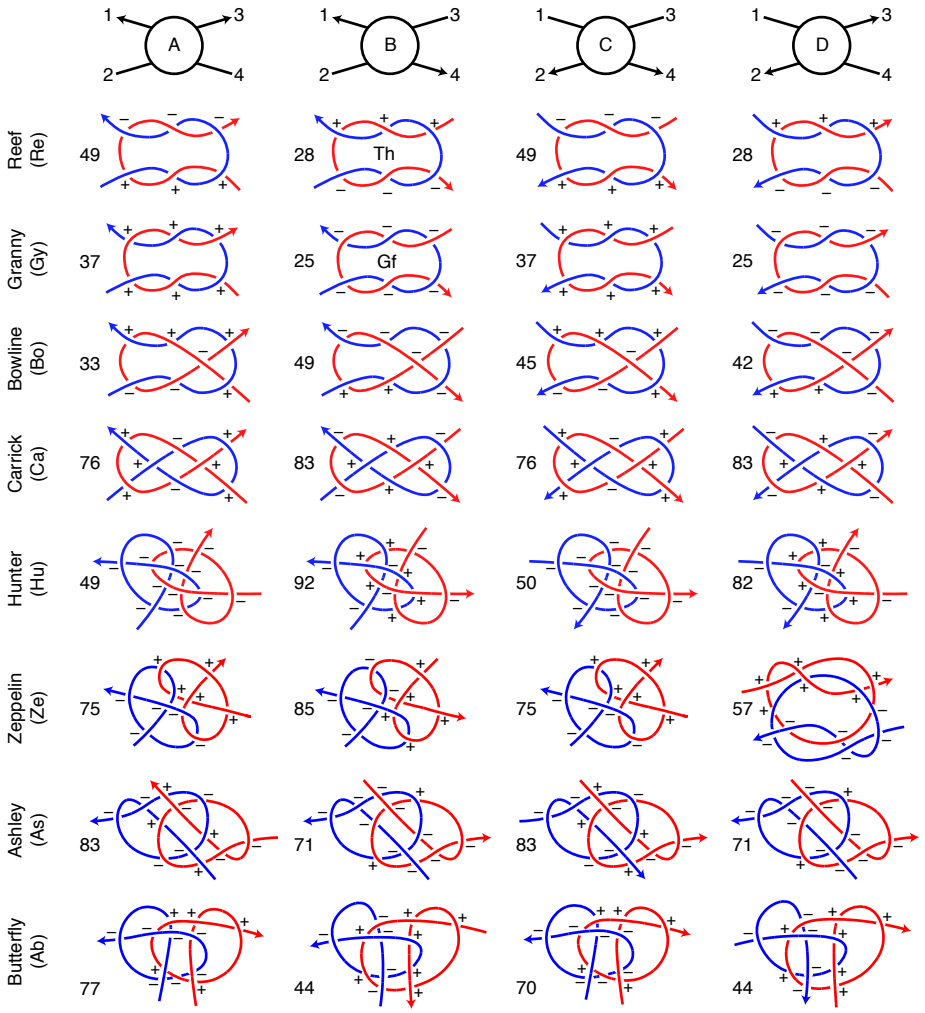

Figure 4-7: **Planar diagrams for all simulated knots.** The top row illustrates the four different possible pulling directions for the diagrams we simulate. Knots are labelled by row and pulling direction, with the exception of the specially named thief (Th) and grief (Gf) knots. While none of the knots above have diagonally opposite ends of the same color, this is theoretically possible, and would require different pulling directions to those specified above. The phase diagram (Fig. 4-5G) contains topological friction information (denoted by numbers above) from only the first two columns, since switching both pulling directions often results in a knot of identical or similar stability, with the same topological state variables (N, τ, Γ), as in columns 1 and 3, or 2 and 4. Changing pulling direction can cause the knot to warp into a different initial planar configuration (e.g. Ze, column 4; As, column 4; Ab, columns 2 and 3).

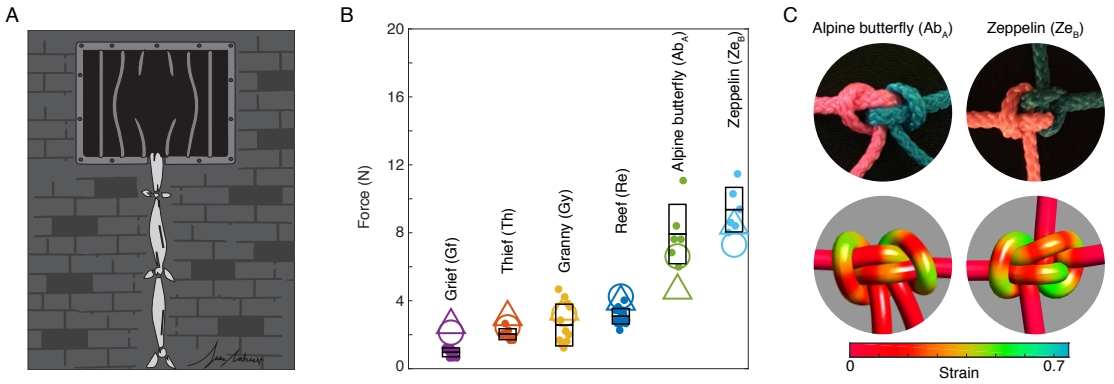

Figure 4-8: **Experiments for commonly used knots validate the theoretically predicted phase diagram.** (**A**) Our experimental setup mimics the classical prison escape problem by determining the critical pulling force $F = mg$ at which two lines untie. (**B**) Experiments measuring the critical mass m at which two Dyneema fibers (diameter 0.15 mm) untie confirm the ranking of knot stability predicted by the simulations. For simpler knots with crossing number $\lesssim 8$, averages (horizontal lines) over individual experiments (small filled circles) agree quantitatively with the relative strength predicted from simulations measuring both the velocity based friction (large empty circles) and the total compression force (large empty triangles) within the knot; black boxes indicate standard deviations of the individual experiments. For complex knots with high crossing number, such as the Zeppelin bend, more sophisticated models accounting for material-specific friction forces and three-dimensional contact details need to be developed in the future. (**C**) Nonetheless, simulations of complex bends with generic friction show good shape agreement with tight configurations of bends in nylon ropes (diameter 20 mm), and reveal the highly non-uniform strain distributions in such knots.

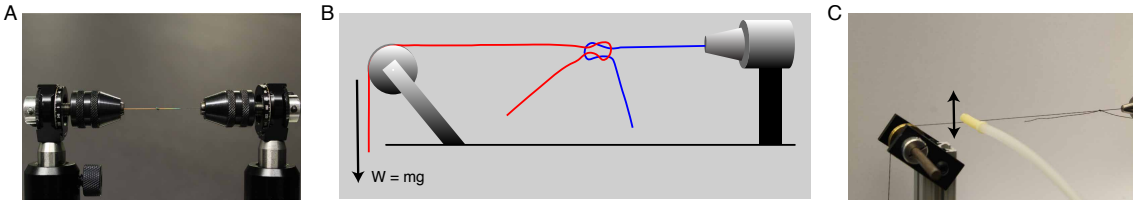

Figure 4-9: **Experimental apparatus.** (**A**) Device for manipulating knotted photonic fibers (Fig. 4-2A,B). (**B**) The knot is held in a drill chuck at one end while the other end is loaded. (**C**) A robotic flicker is used to perturb the knot.

Chapter 5

Topological batteries

Topological constraints have long been known to provide efficient mechanisms for localizing and storing energy across a range of length scales. Despite recent theoretical and experimental progress on the preparation of topological states, the role of topology in the discharging dynamics is not well understood. In this chapter, we investigate robust topological energy release protocols in elastic fiber systems through simulations of 238 knots of varying twist and topology. By breaking the elastic fiber, such topological batteries can perform mechanical work or drive fluid flows. Our study reveals topologically resonant states for which energy release becomes superslow. Owing to their intrinsic stability we expect such tunable topological batteries to have broad applications to storage and directed release of energy in soft matter.

5.1 Introduction

Topological protection provides a robust means for storing and controlling energy, an effect widely used in a variety of biological and physical systems [141, 95, 126, 47, 36, 118]. On small scales, knotted topologies play important functional roles [71] in the behavior of tangled DNA, proteins and polymers [88, 85, 117, 128, 48]. In continuum systems, foundational work on topology has revealed the origin of helicity conservation in classical [95, 76] and complex fluids [72], and the dynamo effect in turbulent plasmas [133, 119]. Recent experimental advances in mechanical lat-

tices [130, 120] and soft robotics [73], bring the question of topologically tunable designer materials into the experimentally accessible realm. Although the study of topological modes [111] has dramatically improved our understanding of soft matter, harnessing topology to perform useful work such as driving flows [44, 125, 91] continues to present fundamental challenges.

Here we study how topology affects energy release dynamics in knotted elastic fibers [5, 63, 110], demonstrating a realization of a topological battery. Topology mediated buckling and instability phenomena underlies the discharging rates and functional capabilities of the batteries. Knotted filaments present an intuitive mechanical realization of a topological battery: By initializing closed elastic loops in tight knotted states [20, 69, 63] with varying twist [96, 25], energy may be stored robustly (Fig 5-2). Cutting the knot at the point of maximum stress results in a controlled topology dependent energy discharge. Through this process, we find special topologically resonant states that are characterized by superslow energy release, exemplifying control of discharging dynamics through topology.

5.2 Energy release dynamics in elastic knots

Kirchhoff model with contact friction

Tying a knot in an elastic fiber and fusing together the free ends produces our main example of a topological battery. By twisting the free ends before fusing, knotted batteries can be studied along the two axes of knot type and twist density (Fig 5-1).

We model the knot system using equations (4.11), presented in Chapter 4. The fibers have natural length L, radius h, and circular cross section with moment of inertia $I = \pi h^4/4$ and cross sectional area $A = \pi h^2$. The state of the fiber is defined by its centerline curve $\boldsymbol{x}(s)$, and an orthonormal material frame, $\{\mathbf{d}_1(s), \mathbf{d}_2(s), \mathbf{d}_3(s)\}$, with $\mathbf{d}_i' = \boldsymbol{\kappa} \times \mathbf{d}_i$, and $\dot{\mathbf{d}}_i = \boldsymbol{\omega} \times \mathbf{d}_i$. The twist density, θ' is defined by $\theta' = \kappa_3$. Here, we make the additional assumption that torsional friction is negligible. The overdamped

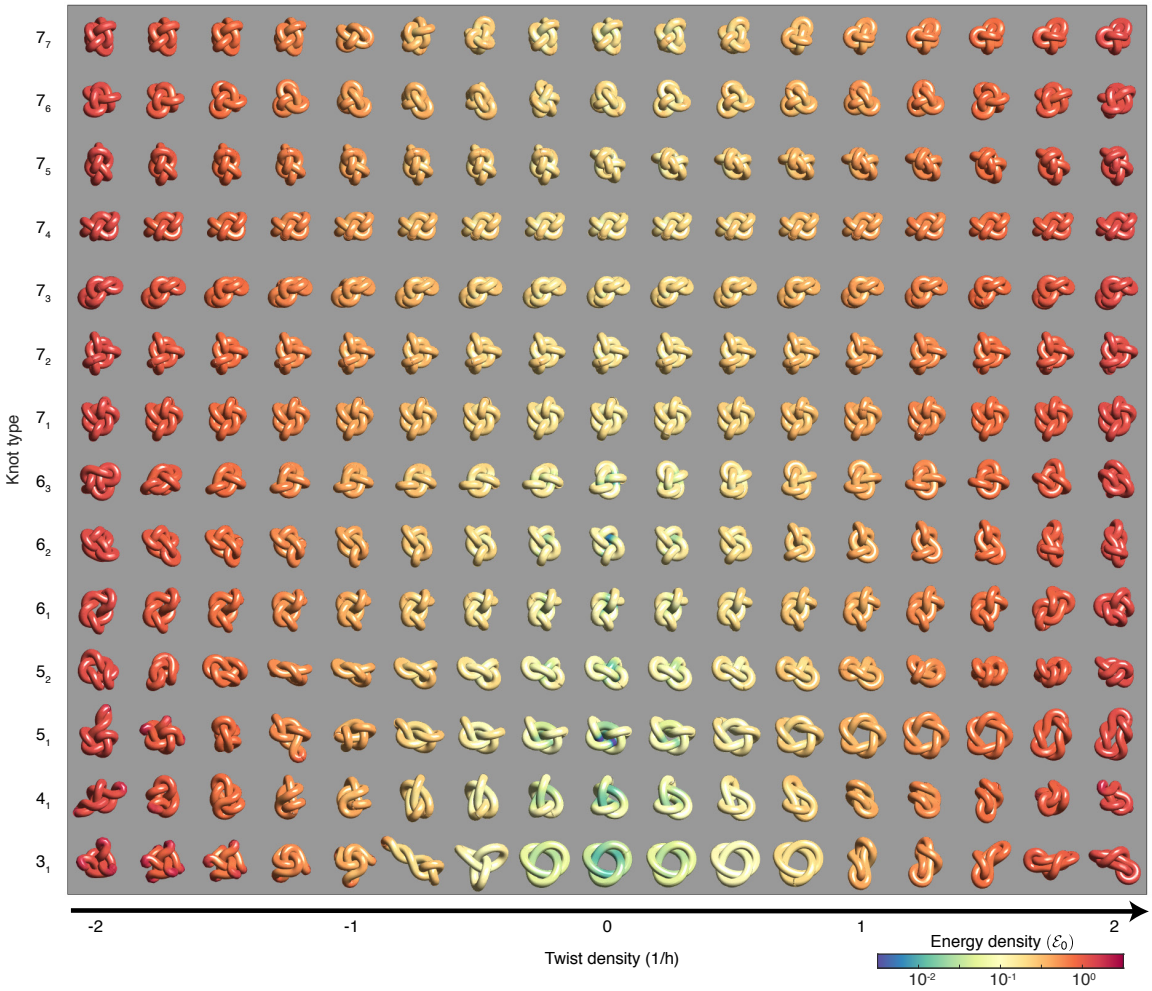

Figure 5-1: Knotted topological batteries are simulated for 238 initial configurations, representing 17 different twist densities for 14 knot types. Simulation parameters: $\nu = 0.3,\ \gamma = 5,\ L/h = 50$.

equations of motion (2.33), together with the collision terms are

$$\begin{aligned} \frac{\delta \mathcal{E}_b}{\delta \boldsymbol{x}} + \frac{\delta \mathcal{E}_t}{\delta \boldsymbol{x}} + \frac{\delta \mathcal{E}_s}{\delta \boldsymbol{x}} &= \eta A \dot{\boldsymbol{x}}'' + \boldsymbol{f}^{\text{col}} \\ \frac{\delta \mathcal{E}_t}{\delta \theta} &= 2\eta I (\omega_3 \mathbf{d}_3)'' \cdot \mathbf{d}_3 \\ \omega_3' + \mathbf{d}_3 \cdot \left(\mathbf{d}_3' \times \dot{\mathbf{d}}_3 \right) &= \dot{\theta}' \end{aligned}$$

where the bend, twist and stretch energies (2.30) are

$$\mathcal{E}_b = \frac{1}{2} \int_0^L ds\ E_b I \kappa^2, \qquad \mathcal{E}_t = \frac{1}{2} \int_0^L ds\ \mu J \theta'^2, \qquad \mathcal{E}_s = \frac{1}{2} \int_0^L ds\ EA \left(|\boldsymbol{x}'| - 1 \right)^2$$

with friction forces (4.10)

$$\boldsymbol{f}^{\mathrm{col}}(s) = -\eta_f A \int_0^L ds' \, \Theta\left(1 - \frac{|\boldsymbol{x}(s) - \boldsymbol{x}(s')|}{2h}\right) \frac{\dot{\boldsymbol{x}}(s) - \dot{\boldsymbol{x}}(s')}{|\boldsymbol{x}(s) - \boldsymbol{x}(s')|^3}$$

In contrast to Chapter 4, we take $\eta_f/\eta = 0.1$ (instead of setting $\eta_f = \eta$). Further, instead of choosing specific values for the elastic constants, E_b, μ, E, we note that the dynamics depends on the relative magnitudes of the bend, twist and stretch energies. In particular, the total energy has the form

$$\mathcal{E} = \frac{E_b A}{2} \int_0^L ds \left[\frac{1}{4} h^2 (\kappa^2 + (\nu+1)^{-1} \theta'^2) + \gamma (|\boldsymbol{x}'| - 1)^2\right] \tag{5.1}$$

Here $E = \gamma E_b$ and ν is the Poisson's ratio. The dimensionless parameters ν and γ therefore govern the dynamics. The intrinsic energy density, $\mathcal{E}_0 = E_b h^2$, and energy, $E_0 = E_b h^2 L$, of the system correspond to the bending energy associated with $\kappa \sim 1/h$. We choose an intrinsic timescale, $T_0 = 2L\eta/hE_b$, as an intermediate scale between the relxation times of pure twist, $T_{tw} = \eta(\nu+1)/E_b$, and pure bending $T_b = 2L^2\eta/\pi^2 h^2 E_b$. The model applies to a range of different materials; a specific candidate system are thin lubricated silicone fibers with $\nu \sim 0.3,\ \gamma \sim 5,\ \eta \sim 10\,\mathrm{kPa{\cdot}s},\ E_b \sim 10\,\mathrm{MPa}$.

5.3 Charging

Charging knotted filaments with twist results in a series of topology mediated buckling instabilities (Fig 5-2A). The twist in the buckled state is typically lower than the initial twist supplied to the pre-buckled state [50]. The evolution of the total twist in the fiber, Tw, follows from relating spatial and time derivatives of the frame

$$\frac{d}{dt} Tw = [\boldsymbol{\Omega} \cdot \mathbf{d}_3]_0^L + \int_0^L ds \; \mathbf{d}_3 \cdot \left(\mathbf{d}_3' \times \dot{\mathbf{d}}_3\right) \tag{5.2}$$

When the fiber is closed, the first term on the right hand side vanishes. Although initializing a fiber with a specific twist requires a time dependent torque application

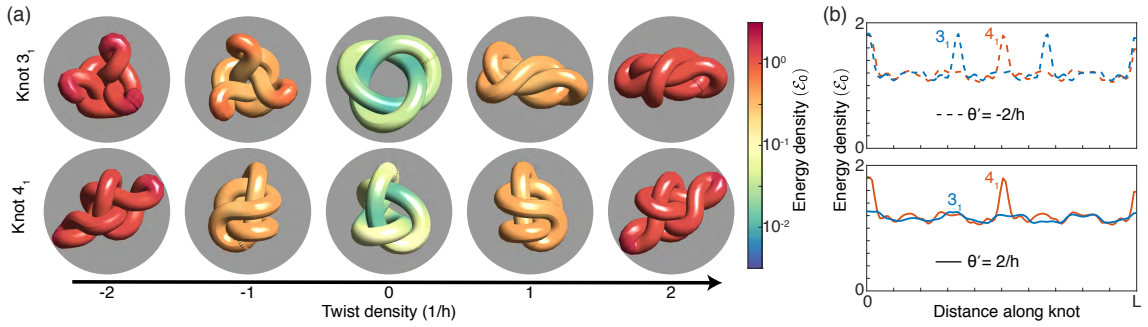

Figure 5-2: Charging topological batteries with knot tying and twist, illustrated for two knot types. (**A**) Energy storage in elastic batteries depends on both knot type and initial twist density. The chiral trefoil knot (3_1, top) exhibits different buckled states at positive and negative twist whereas the achiral figure-of-eight knot (4_1, bottom) does not. (**B**) Chirality-dependent buckling leads to different energy density profiles for the trefoil knot when charged with positive twist ($\theta' = 2/h$) and negative twist ($\theta' = -2/h$). Simulation parameters: $\nu = 0.3,\ \gamma = 5,\ L/h = 50$.

protocol, the amount of buckling provides an indicator of the twist charge within the battery, for a given knot type. For example, twist produces initial battery states with varying post-buckled geometries (Fig 5-2A) and energy densities (Fig 5-2B). Additionally, twist is sensitive to certain underlying topological properties. In our simulations, chiral knots generally exhibit handedness-dependent buckling (Fig 5-2A, top), whereas achiral knots tend to buckle independently of twist handedness (Fig 5-2A, bottom).

5.4 Discharging dynamics and topological resonance

As knotted mechanical batteries unravel, the competition between bending and twisting energies reveals a landscape of topological resonances, where certain initial states lead to super slow energy discharge. After being broken at the point of maximum stress, different transient, metastable states occur (Fig. 5-3A). The discharge dynamics separate into a bending dominated regime and a twist dominated regime, as evident from the initial state of the battery (Fig. 5-3B). The crossover between the two regimes corresponds to the scaling of strains associated with twisting and bending. From (5.1), the characteristic strains for tightly knotted configurations are

$\varepsilon_b \sim h\kappa \sim 1$ for bending and $\varepsilon_{tw} \sim h\theta' \sim hTw/L$ for twisting. As a result, twist dominates the discharge dynamics at high twist densities with $\theta' h > 1$ (Fig. 5-3C-E). Since the effects of varying knot type are more naturally related to the bending energy, twist can be thought of as washing out topology. Indeed, at high twist, $\theta' h > 1$, the batteries discharge quickly, independent of knot type (Fig. 5-3D,E). By contrast, at low twist, knot topology essentially determines the discharging dynamics (Fig 5-3E). In particular, select knots exhibit extremely long discharge times (Fig. 5-3D,E). We can explain these slow topological resonances by considering the mechanisms by which knots release twist and bending energy. Bending forces point in the $\mathbf{d}_3'$ direction, which lies in the fiber's local osculating plane, spanned by $\mathbf{d}_3$ and $\mathbf{d}_3'$. From (5.2), twist changes when $\dot{\mathbf{d}}_3$ has a component in the $\mathbf{d_3} \times \mathbf{d_3}'$ direction; twist relaxation therefore pushes the fiber out of plane. The topologically resonant slow knots can thus be thought of as maximally non-planar and therefore self-confining.

5.5 Conclusions

Topology and mechanics interact to produce long-lived states that are central to the observed topological resonances. For elastic batteries, these states are the intermediate knots that can form as a fiber unties. At small or zero twist, these configurations trap bending energy, leading to long relaxation times. More generally, this principle of topologically activated slow modes can provide a conceptual framework for understanding topological resonances in other soft matter settings.

To conclude, knotted elastic fibers provide a prime demonstration of a topological battery with controlled triggering of energy release via fracture. Our above analysis shows how elastic batteries can be topologically optimized to achieve slow or fast discharge. Owing to the inherent robustness of topological structures, the above ideas translate to a wide range of scales. The energy stored in topological batteries may be harnessed to drive flows or perform mechanical or electrical work, thus opening an avenue for topological control of soft systems.

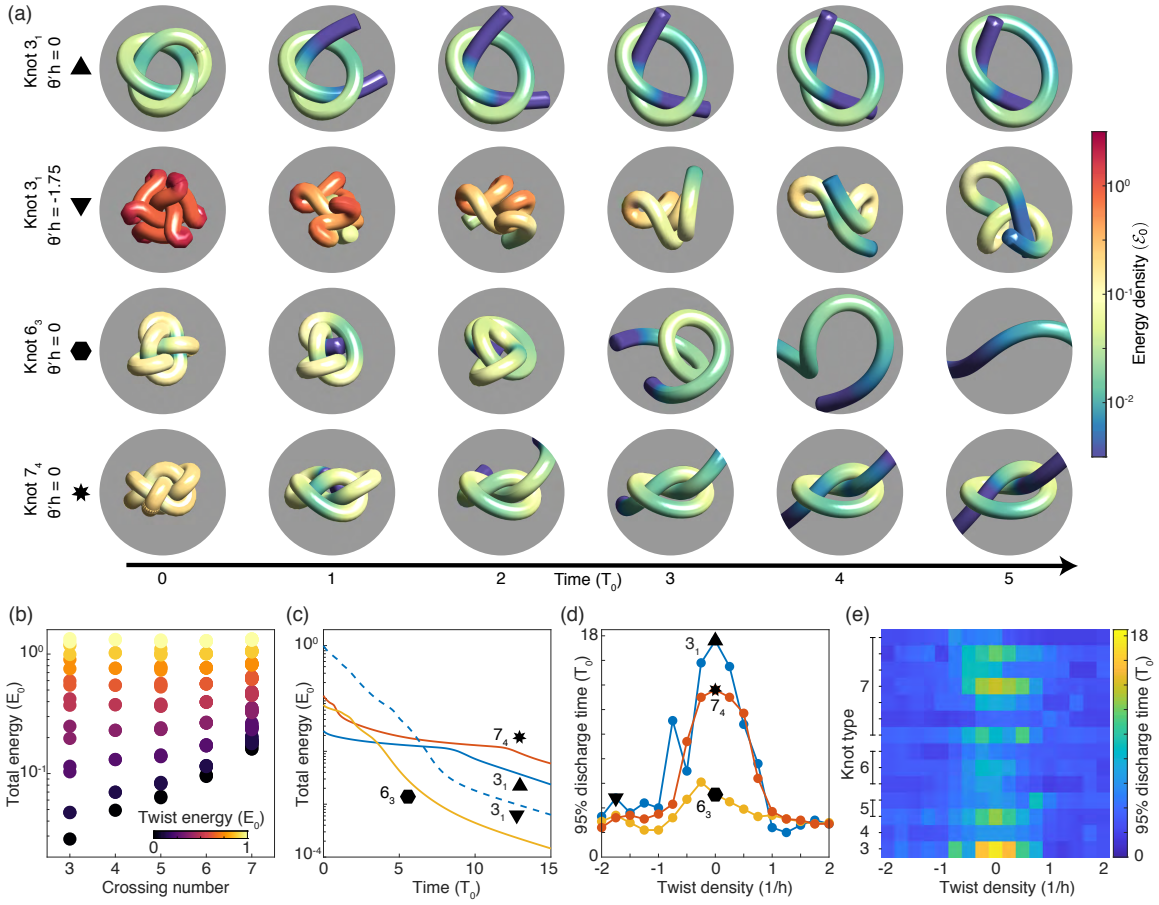

Figure 5-3: Discharging knotted elastic fibers. (**A**) The relaxation dynamics depend strongly on knot type and twist state. (**B**) At low twist, the initial knot energy varies with knot type, while high twist negates the effect of topological changes. (**C**) Energy is released in phases as intermediate metastable topological states form and untie. Topology dependent obstructions cause certain knot types to untie more slowly at zero twist $(3_1, 7_4)$. Higher twist states typically discharge faster but the final discharge rates are set by the relaxed length of the fiber. (**D**) Topological resonances occur predominantly at low twist. (**E**) High twist leads to fast untying for all knot types. At scales where bending dominates, topology dependent resonance effects become visible. Total number of initial knot configurations simulated for (e) is 238 (Fig. 5-1) using the algorithm from Refs. [110, 20].

Chapter 6

Surgical knots

Knot tying is an essential component of surgery. In this brief chapter, we explore applications of the topological model developed in Chapter 4 to the realm of surgical knots. We present numerical results for a class of knots which includes commonly used suturing knots. Our model predicts that the most commonly used surgical knots are indeed the most mechanically stable and balanced. Furthermore, our numerical framework allows the mechanical properties of the sutured wound to be probed in detail. In particular, we demonstrate that the shear forces induced on the underlying tissue by the surgical knot are topology dependent. Beyond our simplified suture model, modern surgical techniques utilize a broad range of knots for a variety of different functions, and we believe that further topological and mechanical study of these systems could yield improved surgical knots.

6.1 Introduction

The rich history of knots in surgery [86, 57, 93] runs parallel to their development for sailing [3] and tool construction [138]. In the context of sutures and orthopedic slings, the medical applications of knots are thought to have been known to several ancient civilizations [86, 57]. Modern surgery uses knots in a range of settings, from hemorrhage prevention [24] to vascular grafts in cardiac surgery [43, 105]. Although recent developments present alternatives to knots in certain scenarios [51], they continue to

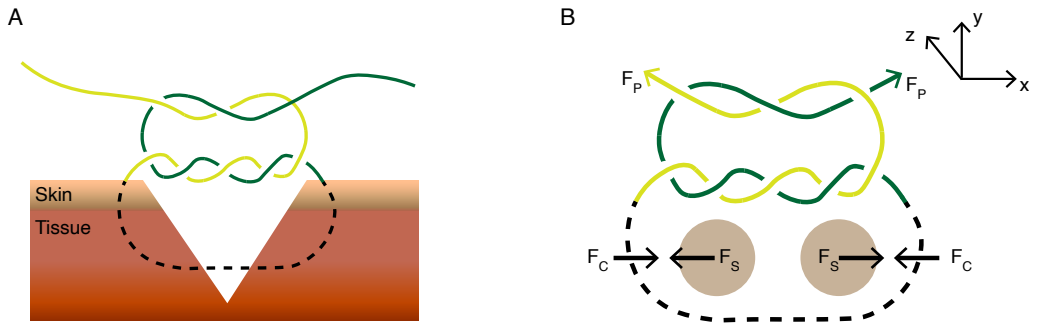

Figure 6-1: Schematic of suturing system. (**A**) A suture knot is used to close up a wound. (**B**) The simplified suture system consists of a knot tied around 2 cylinders representing skin. The skin boundaries are a nonzero distance apart at rest. The knot is pulled with force F_P, causing compression force F_C to act on the cylinders, which experience restoring forces F_S.

be an essential medical tool across many fields [38, 21]. From medical robotics [62, 65] to spaceflight [116], surgical knot training remains essential.

Despite recent important work on surgical mechanics [90, 81, 83], the behavior of surgery knots has not been well studied from a mechanical and topological perspective. Here, we consider the problem of suturing a wound. This scenario, common in surgery, is also closely related to the bend knots we studied in Chapter 4. A key difference is that a suture knot consists of just one strand tied into a loop, which then experiences forces due to skin tension (Fig. 6-1). Based on this, we study a reduced model of a suture (Fig. 6-1B). Such simplified settings are used to train surgeons in knot tying [38]. Below, we present numerical results obtained from simulating this suture system for six different knots. The question of knot stability can be addressed by the results of Chapter 4. The presence of a loop (Fig. 6-1B) gives rise to additional observables. The skin shear force in particular, arises from the collapse of the loop, and appears to be topology dependent.

6.2 Suture model

We model the knot system using equations (4.11), presented in Chapter 4. To summarize, the fiber is described by a centerline curve $\boldsymbol{x}(s,t)$, and an orthonormal material

frame, $\{\mathbf{d}_1, \mathbf{d}_2, \mathbf{d}_3\}$, with $\mathbf{d}_i' = \boldsymbol{\kappa} \times \mathbf{d}_i$, and $\dot{\mathbf{d}}_i = \boldsymbol{\omega} \times \mathbf{d}_i$. The overdamped equations of motion (2.33) are

$$\begin{aligned} \frac{\delta \mathcal{E}_b}{\delta \boldsymbol{x}} + \frac{\delta \mathcal{E}_t}{\delta \boldsymbol{x}} + \frac{\delta \mathcal{E}_s}{\delta \boldsymbol{x}} &= \eta A \dot{\boldsymbol{x}}'' + \boldsymbol{f}^{\text{col}} \\ \frac{\delta \mathcal{E}_t}{\delta \theta} &= 2\eta I (\omega_3 \mathbf{d}_3)'' \cdot \mathbf{d}_3 + \tilde{\tau}^{\text{col}} \\ \omega_3' + \mathbf{d}_3 \cdot \left(\mathbf{d}_3' \times \dot{\mathbf{d}}_3 \right) &= \dot{\theta}' \end{aligned}$$

where the bend, twist and stretch energies (2.30) are

$$\mathcal{E}_b = \frac{1}{2} \int_0^L ds \; E_b I \kappa^2, \qquad \mathcal{E}_t = \frac{1}{2} \int_0^L ds \; \mu J \theta'^2, \qquad \mathcal{E}_s = \frac{1}{2} \int_0^L ds \; EA \left(|\boldsymbol{x}'| - 1 \right)^2$$

with friction forces (4.10)

$$\begin{aligned} \boldsymbol{f}^{\text{col}}(s) &= -\eta A \int_0^L ds' \; \Theta \left(1 - \frac{|\boldsymbol{x}(s) - \boldsymbol{x}(s')|}{2h} \right) \frac{\dot{\boldsymbol{x}}(s) - \dot{\boldsymbol{x}}(s')}{|\boldsymbol{x}(s) - \boldsymbol{x}(s')|^3} \\ \tilde{\tau}^{\text{col}}(s) &= \eta J \int_0^L ds' \; \Theta \left(1 - \frac{|\boldsymbol{x}(s) - \boldsymbol{x}(s')|}{2h} \right) \frac{(\boldsymbol{x}(s') - \boldsymbol{x}(s)) \times (\dot{\boldsymbol{x}}(s') - \dot{\boldsymbol{x}}(s)) \cdot \mathbf{d}_3(s)}{|\boldsymbol{x}(s) - \boldsymbol{x}(s')|^4} \end{aligned}$$

The material properties are identical to those used for the optomechanical fiber simulations in Section 4.3, as these parameters are similar to those of real suture materials [101]. The pulling force F_P (Fig. 6-1B) is set at 0.01 N.

A suture knot pulls the boundaries of a wound together. We treat the skin boundaries of the wound as long cylinders of radius h_s which, due to the presence of the wound, are separated at rest (Fig. 6-1B). In the $z = 0$ plane, suture tightening appears to bring together 2 disks, representing the cross sections of the skin boundaries. Let $\mathbf{w}_0^a$ and $\mathbf{w}_0^b$ be the centers of these disks before the knot is tightened. In other words, $\mathbf{w}_0^a$ and $\mathbf{w}_0^b$ are the intersection between the axes of the boundary cylinders and the $z = 0$ plane. Let $\mathbf{w}^a(t)$ and $\mathbf{w}^b(t)$ be their positions at time t, where tightening begins at $t = 0$, and let $\mathbf{w}_f^a$ and $\mathbf{w}_f^b$ be their final, tight positions. As the knot is tightened, we assume the skin boundary feels an elastic restoring force which acts to reopen the

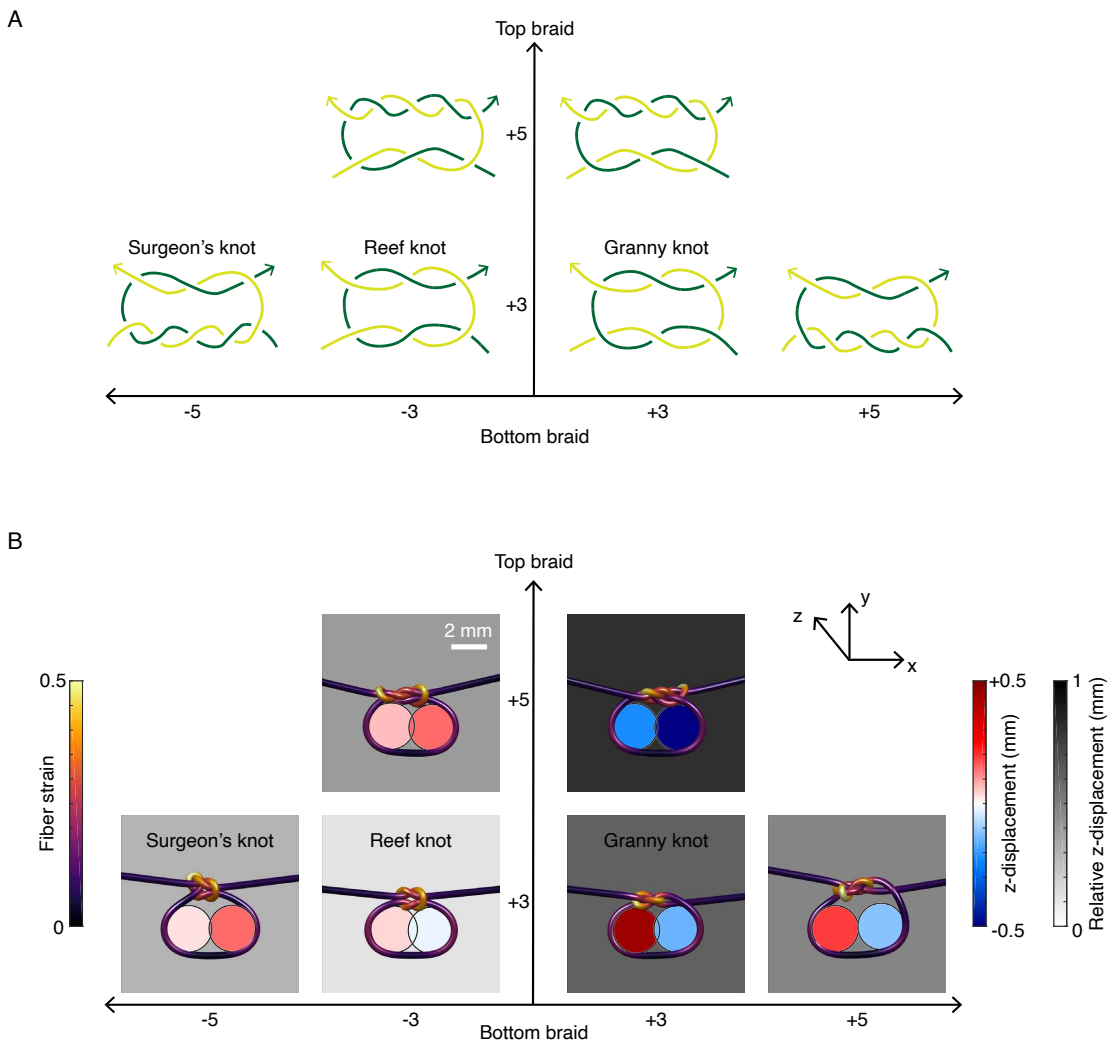

Figure 6-2: Skin shear depends on suture knot topology. (**A**) Knots consisting of 2 braids can be classified by the length and handedness of the top and bottom braids. Only the top part of each suture knot is shown. The reef knot and surgeon's knot are used for suturing in practice. (**B**) Knots with braids of opposite handedness induce less z-displacement in each skin boundary and less relative z-displacement between the two skin boundaries.

wound. This force is

$$\mathbf{F}_S^i(t) = k_s \left(\mathbf{w}(t)^i - \mathbf{w}_0^i \right) \tag{6.1}$$

where $i = a, b$. Together with the fiber equations above, these skin response equations define the suture model.

6.3 Results

Knot stability

Using our model of the suture system, we test 6 different knots, each having the form of 2 braids tied on top of each other (Fig. 6-2A). Although these knots are not 2-tangles, and consist only of 1 fiber, the topological model introduced in Chapter 4 can still provide useful stability information. This is due to the pinching of the bottom loop of the knot by the skin (Fig.6-1). The pinching effect means that, for the purposes of stability, these suture knots are approximately 2-tangles with the bottom ends held fixed and the top ends pulled with force F_P. The writhe (Fig.4-4) of the 2-braid knots we consider (Fig. 6-2A) can be expressed simply in terms of the handedness of the bottom braid, b_K, and the handedness of the top braid, t_K

$$Wr = b_K + t_K$$

For example, the writhe of the surgeon's knot is -2, and the writhe of the granny knot is $+6$, as discussed in Chapter 4. Recall the twist fluctuation energy (4.12)

$$\tau = 1 - \left(\frac{Wr}{N}\right)^2$$

This suggests that the suture knots with smaller writhe, whose top and bottom braids have opposite chirality, will be more stable. This is borne out by surgical practice. Of the knots we simulate, it is the surgeon's knot and reef knot that are used to suture real wounds.

Suture induced shear forces

In addition to stability, we can use our numerical model to access other mechanical properties of the suture system. Calculating the forces applied on the skin and wound by the suture knot has particular biological relevance. Since a tightening suture knot always brings the skin boundaries together in the x, y plane (Fig. 6-2B), we

focus on the z-displacement induced by the knot. The z-displacement measures the response of the skin to the shear forces applied by the knot. Our numerical model predicts that knots with lower writhe, on the left hand side of the phase diagram (Fig. 6-2B), impart smaller shear forces on the skin. This can be seen from either the absolute displacement of each skin boundary, given by $\mathbf{e}_z \cdot \mathbf{w}_f^i,\ i = a, b$, or the relative displacements of the skin boundaries, $|\mathbf{w}_f^a - \mathbf{w}_f^b|$. Once again, we find that the surgeon's knot and reef knot impart the least shear.

That the knots which are more stable topologically are also those producing the smallest shear forces can be understood as a consequence of twist. The shear forces are caused by the non-planar collapse of the loop as the knot is tightened. The twist compatibility equation relates centerline velocity to twist

$$\omega_3' + \mathbf{d}_3 \cdot \left(\mathbf{d}_3' \times \dot{\mathbf{d}}_3\right) = \dot{\theta}'$$

From this equation, we see that non-planar motion produces twist through the triple product term, $\mathbf{d}_3 \cdot \left(\mathbf{d}_3' \times \dot{\mathbf{d}}_3\right)$. Similarly, the twist fluctuation energy is related to the self-torque of the knot (Section 4.4). Thus we expect high shear forces and low stability to be correlated through their relationship with twist production. Taken together, these results suggest that certain knot topologies can control twist and produce stable, balanced mechanics.

6.4 Conclusions

In conclusion, we have introduced a model of a simplified suture knot system, and used it to relate topology to mechanics. This model can be used to calculate key mechanical properties, such as the forces imparted by the knot on the underlying tissue. Experimental validation of these predictions is a crucial next step in gaining a deeper understanding of the complex mechanics at play [66, 55]. In conjunction with experiments, there is considerable scope to use more precise models to study more elaborate surgical systems. A particularly interesting case is that of cardiac surgery,

where knots are often used to graft tubes onto each other [51]. In this scenario, the mechanics and topology of the knot also interact with underlying biological forces. For example, the knots and stitches used must be stable under the periodic forcing induced by blood flow. Expanding the tools introduced here to explore knot tying in these biological contexts is a key direction for future research.

Chapter 7

Conclusions and outlook

In this thesis, we have demonstrated the fundamental role twist plays in the structural and topological stability of elastic rods and fibers. In the first case, twist works by allowing the applied stress to be partitioned into multiple modes, namely the bending and twist modes. The twist stress, which arises from the internal structure of the rod, ultimately has a global effect on the fragmentation process. This suggests a natural generalization to heterogeneous metamaterials with microscopic structures. Such systems have internal modes analogous to twist. The distribution of external stresses and strains over these hidden, internal modes could lead to unexpected changes in macroscopic observables. An interesting question is the extent to which these ideas can be applied to emerging fields in metamaterials such as the study of structured biological matter [115]. A further direction is understanding the continuum properties of bundles of fibers [127], with a focus on the physical consequences of the enlarged space of internal degrees of freedom.

In the second half of this thesis, we showed that topology and mechanics interact through twist, and proposed a topological framework for understanding knot stability. This model necessarily gives an approximate picture of the friction within the knot. However, the agreement between this topological model and experiments suggests that it captures a real effect of the friction. Further progress on knot mechanics requires a much more detailed description of knots than we have presented here. For example, surface details must be modelled, and the full 3D theory may even be

necessary [66, 8]. More detailed models along these lines could also generate new insights into the topological aspects of friction. The surface geometry of contact interactions [55] is a particularly promising direction through which to further study topological friction. In addition, these kinds of refined models could yield further insights into surgical knots.

The topological model presented in Chapter 4 also has applications to higher dimensional systems, such as understanding topological phenomena in field configurations of driven and active fluids. In certain regimes, the effective dynamics of the system in 3D are governed by the behavior of a tangle of 1D objects, such as defect lines or vorticity curves in nematic and classical fluids. Recent work on 3D active nematics in this area explores the dynamical role of disclination loops [34]. The topological model could be applied to the dynamics of more general defect tangles. Biological matter, often comprised of chiral constituents such as actin and DNA, encompasses a variety of possible model systems with which to study the active generalizations of such tangle dynamics.

Bibliography

[1] C. C. Adams. *The Knot Book: An Elementary Introduction to the Mathematical Theory of Knots*. American Mathematical Society, Providence, Rhode Island, 2004.

[2] A. Albrecht, E. Badel, V. Bonnesoeur, Y. Brunet, T. Constant, P. Défossez, E. De Langre, S. Dupont, M. Fournier, B. Gardiner, et al. Comment on "critical wind speed at which trees break". *Phys. Rev. E*, 94(6):067001, 2016.

[3] C. W. Ashley. *The Ashley book of knots*. Doubleday Books, 1944.

[4] U. Attmannspacher, B. E. Scharf, and R. M. Harshey. FliL is essential for swarming: motor rotation in absence of FliL fractures the flagellar rod in swarmer cells of salmonella enterica. *Mol. Microbiol.*, 68(2):328–341, 2008.

[5] B. Audoly, N. Clauvelin, and S. Neukirch. Elastic knots. *Phys. Rev. Lett.*, 99(16):164301, 2007.

[6] B. Audoly and S. Neukirch. Fragmentation of rods by cascading cracks: Why spaghetti does not break in half. *Phys. Rev. Lett.*, 95:095505, 2005.

[7] B. Audoly and Y. Pomeau. *Elasticity and geometry*. Oxford University Press, Oxford, 2010.

[8] C. Baek, P. Johanns, T. G. Sano, P. Grandgeorge, and P. M. Reis. Finite element modeling of tight elastic knots. *J. Appl. Mech.*, 88(2):024501, 2021.

[9] C. Baek, A. O. Sageman-Furnas, M. K. Jawed, and P. M. Reis. Form finding in elastic gridshells. *Proc. Natl. Acad. Sci. U.S.A.*, 115(1):75–80, 2018.

[10] R. C. Ball, M. Doi, S. F. Edwards, and M. Warner. Elasticity of entangled networks. *Polymer*, 22(8):1010–1018, 1981.

[11] R. H. Baughman, A. A. Zakhidov, and W. A. de Heer. Carbon nanotubes–the route toward applications. *Science*, 297(5582):787–792, 2002.

[12] B. F. Bayman. Theory of hitches. *Am. J. Phys.*, 45(2):185–190, 1977.

[13] M. Bergou, B. Audoly, E. Vouga, M. Wardetzky, and E. Grinspun. Discrete viscous threads. *ACM Trans. Graph.*, 29(4):116:1–116:10, 2010.

[14] M. Bergou, M. Wardetzky, S. Robinson, B. Audoly, and E. Grinspun. Discrete elastic rods. *ACM Trans. Graph.*, 27(3):63, 2008.

[15] D. Bölinger, J. I. Sułkowska, H.-P. Hsu, L. A. Mirny, M. Kardar, J. N. Onuchic, and P. Virnau. A stevedore's protein knot. *PLOS Comput. Biol.*, 6(4):e1000731, 2010.

[16] E. Bouchaud. Scaling properties of cracks. *J. Phys. Condens. Matter*, 9(21):4319, 1997.

[17] C. P. Broedersz and F. C. MacKintosh. Modeling semiflexible polymer networks. *Rev. Mod. Phys.*, 86:995–1036, 2014.

[18] H. Brutzer, N. Luzzietti, D. Klaue, and R. Seidel. Energetics at the DNA supercoiling transition. *Biophys. J.*, 98:1267–1276, 2010.

[19] J. A. Calvo, K. C. Millett, and E. J. Rawdon, editors. *Physical Knots: Knotting, Linking, and Folding Geometric Objects in* $\mathbb{R}^3$, volume 304 of *Contemporary Mathematics*. American Mathematical Society, Providence, Rhode Island, 2001.

[20] J. Cantarella, A. LaPointe, and E. J. Rawdon. Shapes of tight composite knots. *J. Phys. A*, 45(22):225202, 2012.

[21] J. Causer, J. N. Vickers, R. Snelgrove, G. Arsenault, and A. Harvey. Performing under pressure: quiet eye training improves surgical knot-tying performance. *Surgery*, 156(5):1089–1096, 2014.

[22] T. O. Channel. Lazaro borges (cub) snaps pole - pole vault - london 2012 olympics. Published on Aug 8, 2012.

[23] N. Charles, M. Gazzola, and L. Mahadevan. Topology, geometry, and mechanics of strongly stretched and twisted filaments: solenoids, plectonemes, and artificial muscle fibers. *Phys. Rev. Lett.*, 123(20):208003, 2019.

[24] J. H. Cho, H. S. Jun, and C. N. Lee. Hemostatic suturing technique for uterine bleeding during cesarean delivery, 2000.

[25] A. Y. Chui and H. K. Moffatt. The energy and helicity of knotted magnetic flux tubes. *Proc. R. Soc. Lond*, 451(1943):609–629, 1995.

[26] A. Clebsch. *Theorie der elasticität fester körper*. Teubner, 1862.

[27] B. D. Coleman, E. H. Dill, M. Lembo, Z. Lu, and I. Tobias. On the dynamics of rods in the theory of Kirchhoff and Clebsch. *Arch. Ration. Mech. Anal.*, 121:339–359, 1993.

[28] J. H. Conway. An enumeration of knots and links, and some of their algebraic properties. In *Computational problems in abstract algebra*, pages 329–358. Elsevier, 1970.

[29] P. Dabrowski-Tumanski and J. I. Sulkowska. Topological knots and links in proteins. *Proc. Natl. Acad. Sci. U.S.A.*, 114(13):3415–3420, 2017.

[30] C. A. Daily-Diamond, C. E. Gregg, and O. M. O'Reilly. The roles of impact and inertia in the failure of a shoelace knot. *Proc. Math. Phys. Eng. Sci.*, 473(2200):20160770, 2017.

[31] Z. Danku and F. Kun. Fracture process of a fiber bundle with strong disorder. *J. Stat. Mech. Theory Exp.*, 2016(7):073211, 2016.

[32] M. D. Demetriou, M. E. Launey, G. Garrett, J. P. Schramm, D. C. Hofmann, W. L. Johnson, and R. O. Ritchie. A damage-tolerant glass. *Nat. Mater.*, 10(2):123–128, 2011.

[33] E. H. Dill. Kirchhoff's theory of rods. *Arch. Hist. Exact Sci.*, pages 1–23, 1992.

[34] G. Duclos, R. Adkins, D. Banerjee, M. S. Peterson, M. Varghese, I. Kolvin, A. Baskaran, R. A. Pelcovits, T. R. Powers, A. Baskaran, et al. Topological structure and dynamics of three-dimensional active nematics. *Science*, 367(6482):1120–1124, 2020.

[35] E. Evans. Probing the relation between force—lifetime—and chemistry in single molecular bonds. *Annu. Rev. Biophys. Biomol. Struct.*, 30(1):105–128, 2001.

[36] D. Ferraro, M. Campisi, G. M. Andolina, V. Pellegrini, and M. Polini. High-power collective charging of a solid-state quantum battery. *Phys. Rev. Lett*, 120(11):117702, 2018.

[37] T. Fink and Y. Mao. *The 85 ways to tie a tie: The science and aesthetics of tie knots*. Broadway, 2000.

[38] L. Fischer, T. Bruckner, B. P. Müller-Stich, J. Höer, H.-P. Knaebel, M. W. Büchler, and C. M. Seiler. Variability of surgical knot tying techniques: do we need to standardize? *Langenbeck's archives of surgery*, 395(4):445–450, 2010.

[39] B. Gardiner, P. Berry, and B. Moulia. Wind impacts on plant growth, mechanics and damage. *Plant Sci.*, 245:94–118, 2016.

[40] S. J. Gerbode, J. R. Puzey, A. G. McCormick, and L. Mahadevan. How the cucumber tendril coils and overwinds. *Science*, 337(6098):1087–1091, 2012.

[41] W. Gerstle, N. Sau, and S. Silling. Peridynamic modeling of concrete structures. *Nucl. Eng. Des.*, 237(12):1250 – 1258, 2007.

[42] C. J. Gilbert, R. O. Ritchie, and W. L. Johnson. Fracture toughness and fatigue-crack propagation in a Zr–Ti–Ni–Cu–Be bulk metallic glass. *Appl. Phys. Lett.*, 71(4):476–478, 1997.

[43] A. M. Gillinov, A. W. Lee, J. M. Redmond, K. J. Zehr, L. Jackson, E. A. Davis, R. H. Hruban, G. M. Williams, and D. E. Cameron. Absorbable suture improves growth of venous anastomoses. *Journal of vascular surgery*, 16(5):769–773, 1992.

[44] L. Giomi, Ž. Kos, M. Ravnik, and A. Sengupta. Cross-talk between topological defects in different fields revealed by nematic microfluidics. *Proc. Natl. Acad. Sci. U.S.A*, 114(29):E5771–E5777, 2017.

[45] J. R. Gladden, N. Z. Handzy, A. Belmonte, and E. Villermaux. Dynamic buckling and fragmentation in brittle rods. *Phys. Rev. Lett.*, 94:035503, 2005.

[46] J. R. Goldman and L. H. Kauffman. Rational tangles. *Adv. Appl. Math.*, 18(3):300–332, 1997.

[47] R. E. Goldstein, H. K. Moffatt, and A. I. Pesci. Topological constraints and their breakdown in dynamical evolution. *Nonlinearity*, 25(10):R85, 2012.

[48] O. Gonzalez and J. H. Maddocks. Global curvature, thickness, and the ideal shapes of knots. *Proc. Natl. Acad. Sci. U.S.A*, 96(9):4769–4773, 1999.

[49] A. Goriely. Twisted elastic rings and the rediscoveries of Michell's instability. *J. Elast.*, 84(3):281–299, 2006.

[50] A. Goriely. Twisted elastic rings and the rediscoveries of michell's instability. *J. Elast*, 84(3):281–299, 2006.

[51] V. L. Gott, D. E. Alejo, and D. E. Cameron. Mechanical heart valves: 50 years of evolution. *The Annals of thoracic surgery*, 76(6):S2230–S2239, 2003.

[52] D. Goundaroulis, N. Gügümcü, S. Lambropoulou, J. Dorier, A. Stasiak, and L. Kauffman. Topological models for open-knotted protein chains using the concepts of knotoids and bonded knotoids. *Polymers*, 9(9):444, 2017.

[53] D. E. Grady. Length scales and size distributions in dynamic fragmentation. *Int. J. Fract.*, 163(1):85–99, 2010.

[54] K. F. Graff. *Wave motion in elastic solids*. Courier Corporation, 2012.

[55] P. Grandgeorge, C. Baek, H. Singh, P. Johanns, T. G. Sano, A. Flynn, J. H. Maddocks, and P. M. Reis. Mechanics of two filaments in tight orthogonal contact. *Proc. Natl. Acad. Sci. U.S.A.*, 118(15), 2021.

[56] A. Y. Grosberg. A few notes about polymer knots. *Polym. Sci. Ser. A*, 51(1):70–79, 2009.

[57] J. J. Hage. Heraklas on knots: sixteen surgical nooses and knots from the first century ad. *World journal of surgery*, 32(4):648–655, 2008.

[58] R. H. Heisser, V. P. Patil, N. Stoop, E. Villermaux, and J. Dunkel. Controlling fracture cascades through twisting and quenching. *Proc. Natl. Acad. Sci. U.S.A.*, 115(35):8665–8670, 2018.

[59] H. J. Herrmann, A. Hansen, and S. Roux. Fracture of disordered, elastic lattices in two dimensions. *Phys. Rev. B*, 39:637–648, 1989.

[60] M. Hetényi. *Beams on Elastic Foundation: Theory with Applications in the Fields of Civil and Mechanical Engineering*. University of Michigan Press, Ann Arbor, 1946.

[61] D. L. Hu, B. Chan, and J. W. M. Bush. The hydrodynamics of water strider locomotion. *Nature*, 424(6949):663–666, 2003.

[62] H. Jan, M. Nobbenhuis, and T. Ind. Comparison of knot tying in robotic, laparoscopic, and open surgery: robotic knots as tight as, but more secure than, open knots. *Journal of Gynecologic Surgery*, 29(6):287–291, 2013.

[63] M. Jawed, P. Dieleman, B. Audoly, and P. M. Reis. Untangling the mechanics and topology in the frictional response of long overhand elastic knots. *Phys. Rev. Lett.*, 115(11):118302, 2015.

[64] M. K. Jawed, A. Novelia, and O. M. O'Reilly. *A primer on the kinematics of discrete elastic rods*. Springer, 2018.

[65] S. R. Jernigan, G. Chanoit, A. Veeramani, S. B. Owen, M. Hilliard, D. Cormier, B. Laffitte, and G. Buckner. A laparoscopic knot-tying device for minimally invasive cardiac surgery. *European journal of cardio-thoracic surgery*, 37(3):626–630, 2010.

[66] P. Johanns, P. Grandgeorge, C. Baek, T. G. Sano, J. H. Maddocks, and P. M. Reis. The shapes of physical trefoil knots. *Extreme Mech. Lett.*, 43:101172, 2021.

[67] R. D. Kamien. Local writhing dynamics. *Eur. Phys. J. B*, 1(1):1–4, 1998.

[68] V. Kantsler and R. E. Goldstein. Fluctuations, dynamics, and the stretch-coil transition of single actin filaments in extensional flows. *Phys. Rev. Lett.*, 108:038103, 2012.

[69] V. Katritch, J. Bednar, D. Michoud, R. G. Scharein, J. Dubochet, and A. Stasiak. Geometry and physics of knots. *Nature*, 384(6605):142–145, 1996.

[70] L. H. Kauffman. An invariant of regular isotopy. *Trans. Am. Math. Soc.*, 318(2):417–471, 1990.

[71] L. H. Kauffman. *Knots and physics*, volume 1. World scientific, 2001.

[72] H. Kedia, I. Bialynicki-Birula, D. Peralta-Salas, and W. T. Irvine. Tying knots in light fields. *Phys. Rev. Lett.*, 111(15):150404, 2013.

[73] Y. Kim, H. Yuk, R. Zhao, S. A. Chester, and X. Zhao. Printing ferromagnetic domains for untethered fast-transforming soft materials. *Nature*, 558(7709):274–279, 2018.

[74] G. Kirchhoff. Ueber das gleichgewicht und die bewegung eines unendlich dünnen elastischen stabes. *J. Reine Angew. Math.*, 1859(56):285–313, 1859.

[75] G. Kirchhoff. *Vorlesungen über mathematische Physik, Mechanik (Vorl. 28)*, volume 1. Teubner, 1876.

[76] D. Kleckner and W. T. Irvine. Creation and dynamics of knotted vortices. *Nat. Phys.*, 9(4):253–258, 2013.

[77] D. Kleckner, L. H. Kauffman, and W. T. Irvine. How superfluid vortex knots untie. *Nat. Phys.*, 12(7):650, 2016.

[78] A. R. Klotz, B. W. Soh, and P. S. Doyle. Motion of knots in dna stretched by elongational fields. *Phys. Rev. Lett.*, 120(18):188003, 2018.

[79] M. Kolle, A. Lethbridge, M. Kreysing, J. J. Baumberg, J. Aizenberg, and P. Vukusic. Bio-inspired band-gap tunable elastic optical multilayer fibers. *Adv. Mater.*, 25(15):2239–2245, 2013.

[80] A. Kudrolli and J. Chopin. Tension-dependent transverse buckles and wrinkles in twisted elastic sheets. *Proc. Royal Soc. A*, 474(2214):20180062, 2018.

[81] B. Kuehlmann, C. A. Bonham, I. Zucal, L. Prantl, and G. C. Gurtner. Mechanotransduction in wound healing and fibrosis. *Journal of clinical medicine*, 9(5):1423, 2020.

[82] S. Kuei, A. M. Słowicka, M. L. Ekiel-Jeżewska, E. Wajnryb, and H. A. Stone. Dynamics and topology of a flexible chain: knots in steady shear flow. *New J. Phys.*, 17(5):053009, 2015.

[83] A. Leber, A. G. Page, D. Yan, Y. Qu, S. Shadman, P. Reis, and F. Sorin. Compressible and electrically conducting fibers for large-area sensing of pressures. *Advanced Functional Materials*, 30(1):1904274, 2020.

[84] A. E. H. Love. *A treatise on the mathematical theory of elasticity*. Cambridge University Press, 2013.

[85] R. C. Lua and A. Y. Grosberg. Statistics of knots, geometry of conformations, and evolution of proteins. *PLoS Comput. Biol.*, 2(5):e45, 2006.

[86] D. Mackenzie. The history of sutures. *Medical history*, 17(2):158–168, 1973.

[87] J. H. Maddocks and J. B. Keller. Ropes in equilibrium. *SIAM J. Appl. Math.*, 47(6):1185–1200, 1987.

[88] D. Marenduzzo, E. Orlandini, A. Stasiak, L. Tubiana, C. Micheletti, et al. Dna–dna interactions in bacteriophage capsids are responsible for the observed dna knotting. *Proc. Natl. Acad. Sci. U.S.A*, 106(52):22269–22274, 2009.

[89] S. G. Markande and E. A. Matsumoto. Knotty knits are tangles on tori. *arXiv preprint arXiv:2002.01497*, 2020.

[90] E. A. Matsumoto, H. Liang, and L. Mahadevan. Topology, geometry, and mechanics of z-plasty. *Physical review letters*, 120(6):068101, 2018.

[91] R. Matthews, A. Louis, and J. Yeomans. Complex dynamics of knotted filaments in shear flow. *EPL*, 92(3):34003, 2010.

[92] A. G. McCormick. *Discrete differential geometry and physics of elastic curves*. PhD thesis, Harvard University, Cambridge, MA, 2013.

[93] L. G. Miller. The earliest (?) description of a string figure. *American Anthropologist*, 47(3):461–462, 1945.

[94] N. P. Mitchell, V. Koning, V. Vitelli, and W. T. M. Irvine. Fracture in sheets draped on curved surfaces. *Nat. Mater.*, 16(1):89–93, 2017.

[95] H. K. Moffatt. The degree of knottedness of tangled vortex lines. *J. Fluid Mech*, 35(1):117–129, 1969.

[96] H. K. Moffatt. The energy spectrum of knots and links. *Nature*, 347(6291):367–369, 1990.

[97] H. K. Moffatt and R. L. Ricca. Helicity and the călugăreanu invariant. In *Knots And Applications*, pages 251–269. World Scientific, 1995.

[98] V. V. Mokashi, D. Qian, and Y. Liu. A study on the tensile response and fracture in carbon nanotube-based composites using molecular mechanics. *Compos. Sci. Technol.*, 67(3):530–540, 2007.

[99] N. Mott. Fragmentation of shell cases. *Proc. Royal Soc. A*, 189(1018):300–308, 1947.

[100] D. Moulton, T. Lessinnes, and A. Goriely. Morphoelastic rods. part i: A single growing elastic rod. *J. Mech. Phys. Solids*, 61(2):398–427, 2013.

[101] S. Najibi, R. Banglmeier, J. Matta, and M. Tannast. Material properties of common suture materials in orthopaedic surgery. *The Iowa orthopaedic journal*, 30:84, 2010.

[102] K. C. Neuman and A. Nagy. Single-molecule force spectroscopy: optical tweezers, magnetic tweezers and atomic force microscopy. *Nat. Methods*, 5(6):491–505, 2008.

[103] W. M. Nottage and R. K. Lieurance. Arthroscopic knot tying techniques. *Arthroscopy*, 15(5):515–521, 1999.

[104] D. J. Odde, L. Ma, A. H. Briggs, A. DeMarco, and M. W. Kirschner. Microtubule bending and breaking in living fibroblast cells. *J. Cell Sci.*, 112(19):3283–3288, 1999.

[105] C. S. Ong, X. Zhou, C. Y. Huang, T. Fukunishi, H. Zhang, and N. Hibino. Tissue engineered vascular grafts: current state of the field. *Expert review of medical devices*, 14(5):383–392, 2017.

[106] E. Panagiotou. The linking number in systems with periodic boundary conditions. *J. Comput. Phys.*, 300:533–573, 2015.

[107] A. Panaitescu, G. M. Grason, and A. Kudrolli. Persistence of perfect packing in twisted bundles of elastic filaments. *Phys. Rev. Lett.*, 120(24):248002, 2018.

[108] V. P. Patil. vppatil28/knot_simulation: Knot simulation code, Nov. 2019.

[109] V. P. Patil, Ž. Kos, M. Ravnik, and J. Dunkel. Discharging dynamics of topological batteries. *Phys. Rev. Research*, 2(4):043196, 2020.

[110] V. P. Patil, J. D. Sandt, M. Kolle, and J. Dunkel. Topological mechanics of knots and tangles. *Science*, 367(6473):71–75, 2020.

[111] J. Paulose, B. G.-g. Chen, and V. Vitelli. Topological modes bound to dislocations in mechanical metamaterials. *Nat. Phys.*, 11(2):153, 2015.

[112] R. H. J. Peerlings, R. de Borst, W. A. M. Brekelmans, and M. G. D. Geers. Gradient-enhanced damage modelling of concrete fracture. *Mech. Cohes.-Frict. Mat.*, 3(4):323–342, 1998.

[113] H. Peterlik, P. Roschger, K. Klaushofer, and P. Fratzl. From brittle to ductile fracture of bone. *Nat. Mater.*, 5(1):52–55, 2006.

[114] A. J. Pons and A. Karma. Helical crack-front instability in mixed-mode fracture. *Nature*, 464(7285):85, 2010.

[115] V. N. Prakash, M. S. Bull, and M. Prakash. Motility-induced fracture reveals a ductile-to-brittle crossover in a simple animal's epithelia. *Nat. Phys.*, pages 1–8, 2021.

[116] A. Rafiq, R. Hummel, V. Lavrentyev, W. Derry, D. Williams, and R. C. Merrell. Microgravity effects on fine motor skills: tying surgical knots during parabolic flight. *Aviation, space, and environmental medicine*, 77(8):852–856, 2006.

[117] E. J. Rawdon, K. C. Millett, and A. Stasiak. Subknots in ideal knots, random knots, and knotted proteins. *Sci. Rep*, 5:8928, 2015.

[118] J. Ren, P. Hänggi, B. Li, et al. Berry-phase-induced heat pumping and its impact on the fluctuation theorem. *Phys. Rev. Lett*, 104(17):170601, 2010.

[119] R. L. Ricca and F. Maggioni. Groundstate energy spectra of knots and links: magnetic versus bending energy. In *New Directions in Geometric and Applied Knot Theory*, pages 276–288. Sciendo, 2017.

[120] D. Z. Rocklin, S. Zhou, K. Sun, and X. Mao. Transformable topological mechanical metamaterials. *Nat. Commun.*, 8:14201, 2017.

[121] J. Rosen. In praise of the humble knot. New York Times, September 2014. [Online; posted 17-September-2014].

[122] T. Sanchez, D. T. N. Chen, S. J. DeCamp, M. Heymann, and Z. Dogic. Spontaneous motion in hierarchically assembled active matter. *Nature*, 491(7424):431–434, 2012.

[123] J. D. Sandt, M. Moudio, J. K. Clark, J. Hardin, C. Argenti, M. Carty, J. A. Lewis, and M. Kolle. Stretchable optomechanical fiber sensors for pressure determination in compressive medical textiles. *Adv. Healthc. Mater.*, 7(15):1800293, 2018.

[124] M. W. Scheeler, W. M. van Rees, H. Kedia, D. Kleckner, and W. T. Irvine. Complete measurement of helicity and its dynamics in vortex tubes. *Science*, 357(6350):487–491, 2017.

[125] A. Sengupta, C. Bahr, and S. Herminghaus. Topological microfluidics for flexible micro-cargo concepts. *Soft Matter*, 9:7251–7260, 2013.

[126] B. Senyuk, Q. Liu, S. He, R. D. Kamien, R. B. Kusner, T. C. Lubensky, and I. I. Smalyukh. Topological colloids. *Nature*, 493(7431):200, 2013.

[127] H. Shi, D. A. Quint, G. M. Grason, A. Gopinathan, and K. C. Huang. Chiral twisting in a bacterial cytoskeletal polymer affects filament size and orientation. *Nat. Commun.*, 11(1):1–12, 2020.

[128] A. Stasiak, V. Katritch, J. Bednar, D. Michoud, and J. Dubochet. Electrophoretic mobility of dna knots. *Nature*, 384(6605):122–122, 1996.

[129] R. Stolz, M. Yoshida, R. Brasher, M. Flanner, K. Ishihara, D. J. Sherratt, K. Shimokawa, and M. Vazquez. Pathways of dna unlinking: A story of stepwise simplification. *Sci. Rep.*, 7(1):12420, 2017.

[130] K. Sun, A. Souslov, X. Mao, and T. Lubensky. Surface phonons, elastic response, and conformal invariance in twisted kagome lattices. *Proc. Natl. Acad. Sci. U.S.A*, 109(31):12369–12374, 2012.

[131] C. Sykes. *No Ordinary Genius*. W. W. Norton and Company Ltd., New York, 1996.

[132] M. D. Tang-Schomer, A. R. Patel, P. W. Baas, and D. H. Smith. Mechanical breaking of microtubules in axons during dynamic stretch injury underlies delayed elasticity, microtubule disassembly, and axon degeneration. *FASEB J.*, 24(5):1401–1410, 2010.

[133] J. B. Taylor. Relaxation of toroidal plasma and generation of reverse magnetic fields. *Phys. Rev. Lett.*, 33(19):1139, 1974.

[134] W. Thomson. II. On vortex atoms. *Philos. Mag.*, 34(227):15–24, 1867.

[135] U. Tkalec, M. Ravnik, S. Čopar, S. Žumer, and I. Muševič. Reconfigurable knots and links in chiral nematic colloids. *Science*, 333(6038):62–65, 2011.

[136] J. B. Trimbos. Security of various knots commonly used in surgical practice. *Obstet. Gynecol.*, 64(2):274–280, 1984.

[137] D. L. Turcotte. Fractals and fragmentation. *J. Geophys. Res. Solid Earth*, 91(B2):1921–1926, 1986.

[138] J. C. Turner and P. van de Griend, editors. *History and Science of Knots*, volume 11 of *K & E series on knots and everything.* World Scientific, Singapore, 1996.

[139] E. Villermaux. Fragmentation. *Annu. Rev. Fluid Mech.*, 39(1):419–446, 2007.

[140] E. Villermaux. Self-activated fragmentation. *Int. J. Fract.*, 206(2):171–193, 2017.

[141] P. Virnau, L. A. Mirny, and M. Kardar. Intricate knots in proteins: Function and evolution. *PLOS Comput. Biol.*, 2(9):e122, 2006.

[142] E. Virot, A. Ponomarenko, É. Dehandschoewercker, D. Quéré, and C. Clanet. Critical wind speed at which trees break. *Phys. Rev. E*, 93(2):023001, 2016.

[143] P. B. Warren, R. C. Ball, and R. E. Goldstein. Why clothes don't fall apart: Tension transmission in staple yarns. *Phys. Rev. Lett.*, 120:158001, 2018.

[144] F. Wittel, F. Kun, H. J. Herrmann, and B. H. Kröplin. Fragmentation of shells. *Phys. Rev. Lett.*, 93:035504, 2004.

[145] M.-F. Yu, O. Lourie, M. J. Dyer, K. Moloni, T. F. Kelly, and R. S. Ruoff. Strength and breaking mechanism of multiwalled carbon nanotubes under tensile load. *Science*, 287(5453):637–640, 2000.

[146] H. Zhang and K. Ravi-Chandar. On the dynamics of necking and fragmentation–I. Real-time and post-mortem observations in Al 6061-O. *Int. J. Fract.*, 142(3-4):183–217, 2006.